This is to certify that the
dissertation entitled

HIGH ORDER FINITE ELEMENT METHODS TO COMPUTE
TAYLOR TRANSFER MAPS

presented by

SHASHIKANT MANIKONDA

has been accepted towards fulfillment
of the requirements for the

___Ph.D.___ degree in ___Physics and Astronomy___

_____
Major Professor's Signature

_____8/24/06_____
Date

MSU is an Affirmative Action/Equal Opportunity Institution

PLACE IN RETURN BOX to remove this checkout from your record.
TO AVOID FINES return on or before date due.
MAY BE RECALLED with earlier due date if requested.

DATE DUE	DATE DUE	DATE DUE

HIGH ORDER FINITE ELEMENT METHODS TO COMPUTE TAYLOR TRANSFER MAPS

By

Shashikant Manikonda

A DISSERTATION

Submitted to
Michigan State University
in partial fulfillment of the requirements
for the degree of

DOCTOR OF PHILOSOPHY

Department of Physics and Astronomy

2006

ABSTRACT

HIGH ORDER FINITE ELEMENT METHODS TO COMPUTE TAYLOR TRANSFER MAPS

By

Shashikant Manikonda

In beam physics, map methods are important techniques for the design and analysis of lattice structures. The computation of the transfer map for an electric or magnetic element requires the multipole decomposition of the field in the region where the beam passes. In the first part of this dissertation we present new techniques to extract the multipole decomposition of the electric or magnetic field from the measured field data or from the knowledge of the current distribution.

The new high precision technique developed to obtain the multipole decomposition of the field from the measured field data solves the Laplace equation using the Helmholtz vector decomposition theorem and differential algebraic methods. This technique requires the field to be specified on a closed surface enclosing the volume of interest. The method outperforms the conventional finite difference and finite element methods in both the execution speed and the precision achieved. We extend this technique to obtain a verified solution to the Laplace equation by using the Taylor model methods. We also parallelize this technique and implement it on a high performance cluster.

We then present a new high precision technique to find the magnetic field of an arbitrary current distribution. The technique uses the Biot-Savart law and differential algebra methods to compute the magnetic field. Using this technique we develop new computational tools to design accelerator magnets.

Both these techniques can also be combined to solve the Poisson equation when the source distribution is specified inside a volume and the field is specified on the surface enclosing the volume. Besides providing a natural multipole decomposition of the field both these tools have the unique advantage of always producing purely Maxwellian fields.

We demonstrate the utility of these techniques in solving practical problems by applying them to real life applications. We present the design and analysis of a novel combined function multipole magnet with an elliptic cross section that can simplify the correction of aberrations in the large acceptance fragment separators for radioactive ion accelerators. We then apply the Laplace field solver to the measured magnetic field data of the dipole magnet of the MAGNEX spectrometer and extract the multipole decomposition of the magnetic field. Finally, we present the linear and high order ion optic simulations for the proposed design of the superconducting fragment separator (Super-FRS) and also apply the field solver technique to extract the transfer map for the magnetic field data obtained through the TOSCA simulation for the Super-FRS quadrupole magnet.

TABLE OF CONTENTS

LIST OF TABLES

LIST OF FIGURES

CHAPTER 1

Introduction

The advent of computers has provided new means to solve the problems in physics. Traditionally, the choice of the technique to numerically solve a PDE is driven by the factors faster execution and the minimal use of the computational resources. Both these factors are purely practical limitations due to the limited time and resources. In the traditional numerical techniques the requirement of fast execution and minimal use of resources can only be achieved at the cost of limiting the precision of the numerical result. However, for many problems in physics that investigate phenomena and processes at high energy (TeV) or in relatively small (nano/femto) length and time scales, highly accurate results are an absolute necessity which the traditional numerical methods can not provide. For instance, the Large hadron collider (LHC) accelerator being built at CERN is designed for an energy of 14 TeV at the interaction point and luminosity of $10^{35} cm^{-2} \sec^{-1}$ [5], and this requires magnets to be designed with a magnetic field precision of $\frac{\triangle B}{B} \sim 10^{-4}$ [37]. The modeling and study of such instruments require high precision numerical tools. This leads to an additional constraint for modern numerical techniques of obtaining very high precision results. The traditional numerical techniques can not achieve all of the three conditions at the same time, and hence fail to solve many modern problems. This leads us to

investigate new numerical techniques that are not only fast and make efficient use of the computational resources, but also give high precision results.

One of the limitations with the conventional techniques comes from the fact that the mathematical functions cannot be directly used on a computer. The treatment of a function is done based on the treatment of numbers, and as a result, virtually all the classical numerical algorithms are based on the mere evaluation of functions at specific points. One way to overcome this difficulty is through the use of the local Taylor expansion of a function about a point. We are then able to extract more information about the function than just the value at a specific point. Once again due to the limitation of the computational resources it is necessary to truncate the Taylor expansion.

Algebraic operations like $+, -, \cdot$ and composition can be defined on truncated Taylor expansions, leading to an algebra called the truncated power series algebra (TPSA) [7]. The power of TPSA can be further enhanced by the introduction of derivations ∂ and their inverses, corresponding to the differentiation and integration on the space of functions. The resulting structure is called a Differential Algebra (DA) [67, 47]. The Differential Algebra provides a framework to develop techniques and algorithms to use a truncated Taylor expansion of a function on a computer. The numerical techniques based on DA have the unique advantage of getting high accuracy at a very small cost of the execution time and the computational resources compared to the traditional techniques.

In beam physics, the DA techniques were first introduced by M. Berz 1989 [12, 10, 9, 11] to compute the high-order Taylor expansions of the transfer maps. The beam physics codes based on the DA techniques have become indispensable tools to the design and analysis of accelerator lattices. In recent years the DA techniques have been applied to solve DAEs, ODEs and PDEs [50, 42, 43, 28].

CHAPTER 2

Background information

In this chapter we present the background behind the work presented in this dissertation. We start by defining a vector field in the 3-dimensional Euclidean space $\mathbb{E}^3$ and discussing the relevant properties. We then discuss the Laplace equation and the Poisson equation and present some of their properties. We also present a brief survey of the analytic and numerical techniques to solve the Laplace and the Poisson equations. We then discuss the background of the numerical techniques that we utilize in this dissertation, namely the Differential Algebra (DA) and the Taylor Model (TM).

2.1 Vector field and the Helmholtz theorem

Let V be a bounded region in the 3-dimensional (3D) Euclidean space $\mathbb{E}^3$. A vector field on the $\mathbb{E}^3$ is a function $\vec{B}$ that assigns to each point (x, y, z) in V a three-dimensional vector $\vec{B}(x, y, z)$. A vector field that has zero curl everywhere is called an *irrotational field*. Such a field can be expressed as a gradient of a scalar field. This scalar field is called a scalar potential. A vector field that has zero divergence everywhere is called a *solenoidal field*. Such a field can be expressed as a curl of a vector field. This vector field is called a vector potential.

2.1.1 The Helmholtz theorem for Euclidean three-space

The Helmholtz theorem [40, 59, 44, 62, 61] expresses any general vector field as a sum of an irrotational field and a solenoidal field over all of a Euclidean three-space.

Theorem 1 (The Helmholtz theorem for Euclidean three-space) *A general continuous three-vector field defined everywhere in a Euclidean three-space, that along with its first derivatives vanishes sufficiently rapidly at infinity, may be uniquely represented as a sum of an irrotational part and a solenoidal part.*

The theorem imply that any vector field $\vec{B}(\vec{r})$ can be written as

$$\vec{B} = -\nabla\phi_n + \nabla \times \vec{A}_t, \tag{2.1.1}$$

where $\vec{A}_t$ is a vector potential and ϕ_n is a scalar potential. A simple proof of this statement follows directly from a well-know vector identity for an arbitrary vector field,

$$-\nabla^2\vec{V} = \vec{\nabla} \times \left(\nabla \times \vec{V}\right) - \nabla\left(\nabla \cdot \vec{V}\right)$$

Now by choosing $\vec{B} = -\nabla^2\vec{V}$, $\phi_n = \nabla \cdot \vec{V}$ and $\vec{A}_t = \nabla \times \vec{V}$, we get the equation (2.1.1). However, this assumes that there is always a solution to the vector Poisson equation, $\vec{B} = -\nabla^2\vec{V}$. We now propose the following

Proposition 2 *For any vector field $\vec{B}(\vec{r})$ that vanishes fast for large r, and satisfies a Hölder condition, a vector potential $\vec{V}$ given by*

$$\vec{V}(\vec{r}) = -\int_{\mathbb{E}^3} \frac{\vec{B}\left(\vec{r}'\right)}{4\pi\left|\vec{r} - \vec{r}'\right|} d\Omega', \tag{2.1.2}$$

is the solution to a vector Poisson equation

$$\vec{B}(\vec{r}) = -\nabla^2\vec{V}(\vec{r}). \tag{2.1.3}$$

4

We now prove the proposition above. We first note that the volume integral in the equation (2.1.2) exists only if the vector field $\vec{B}(\vec{r})$ vanishes fast for large r. Such a vector field has a compact support in $\mathbb{E}^3$, as a result the integral over all of Euclidean three-space in the equation (2.1.2) can expressed as an integral on finite volume

$$\vec{V}(\vec{r}) = -\int_V \frac{\vec{B}(\vec{r}')}{4\pi \left|\vec{r} - \vec{r}'\right|} d\Omega',\qquad(2.1.4)$$

where volume V is in $\mathbb{E}^3$. We now take the Laplacian of $\vec{V}$ in equation (2.1.4) to get

$$\nabla^2 \vec{V}(\vec{r}) = -\nabla^2 \left[\int_V \frac{\vec{B}(\vec{r}')}{4\pi \left|\vec{r} - \vec{r}'\right|} d\Omega'\right],\qquad(2.1.5)$$

$$= -\int_V \frac{\vec{B}(\vec{r}')}{4\pi} \nabla^2 \left(\frac{1}{\left|\vec{r} - \vec{r}'\right|}\right) d\Omega'.$$

Since the Laplacian is with respect to the unprimed coordinates, r, the integral and the vector $\vec{B}$ can be brought out of the Laplacian. The final step is proving the relation

$$-\int_V \frac{\vec{B}(\vec{r}')}{4\pi} \nabla^2 \left(\frac{1}{\left|\vec{r} - \vec{r}'\right|}\right) d\Omega' = \vec{B}(\vec{r}).\qquad(2.1.6)$$

Once we prove the equation above, we can use the above equation and the equation (2.1.5) to complete the proof that the vector potential $V(\vec{r})$ given by equation (2.1.1) is the solution to the vector Poisson equation (2.1.3). To prove the equation (2.1.6) we need all the three components of the vector field B_i ($i = 1, 2, \text{or } 3$) to satisfy a Hölder condition.

Definition 3 *[61] Let $r_0 = \left|\vec{r}_2 - \vec{r}_1\right|$ be the distance between two points $\vec{r}_1$ and $\vec{r}_2$. If three positive constants a, n, c exist such that*

$$\left|B_i(\vec{r}_2) - B_i(\vec{r}_1)\right| < a r_0^n,$$

for all points $\vec{r}_1$ and $\vec{r}_2$ for which $r_0 < c$, the quantity B_i is said to satisfy a Hölder condition.

5

The B_i is also said to be Hölder continuous. We are now ready to prove the relation expressed in equation (2.1.6).

Proof. We note that

$$\nabla^2 \left(\frac{1}{\left| \vec{r} - \vec{r}' \right|} \right) = 0 \; \forall \; \vec{r} \neq \vec{r}',$$

thus the volume integral in equation (2.1.6) is zero except for the contribution from the singular point $\vec{r} = \vec{r}'$. As $\vec{r}'$ approaches $\vec{r}$, the distance $\left| \vec{r} - \vec{r}' \right|$ tends towards zero. We surround this singular point by a small sphere of radius ϵ, with surface S_ϵ and volume V_ϵ. Since $\vec{B} \left(\vec{r}' \right)$ satisfies a Hölder condition, we can choose ϵ so small that for all values of $\vec{r}'$ inside the sphere, $\vec{B}$ is essentially equal to its value $\vec{B} \left(\vec{r}' \right)$ at the singular point. Then the integral in the equation (2.1.6) becomes

$$\int_V \frac{\vec{B} \left(\vec{r}' \right)}{4\pi} \nabla^2 \left(\frac{1}{\left| \vec{r} - \vec{r}' \right|} \right) d\Omega' = \frac{\vec{B} \left(\vec{r} \right)}{4\pi} \int_{V_\epsilon} \nabla^2 \left(\frac{1}{\left| \vec{r} - \vec{r}' \right|} \right) d\Omega'. \tag{2.1.7}$$

Using the relations,

$$\nabla \left(\frac{1}{\left| \vec{r} - \vec{r}' \right|} \right) = -\nabla' \left(\frac{1}{\left| \vec{r} - \vec{r}' \right|} \right),$$

$$\nabla^2 \left(\frac{1}{\left| \vec{r} - \vec{r}' \right|} \right) = \nabla'^2 \left(\frac{1}{\left| \vec{r} - \vec{r}' \right|} \right),$$

and the divergence theorem on the volume integral we obtain

$$\frac{\vec{B} \left(\vec{r} \right)}{4\pi} \int_{V_\epsilon} \nabla^2 \left(\frac{1}{\left| \vec{r} - \vec{r}' \right|} \right) d\Omega' = \frac{\vec{B} \left(\vec{r} \right)}{4\pi} \oint_{S_\epsilon} \hat{n} \left(\vec{r}' \right) \cdot \nabla' \left(\frac{1}{\left| \vec{r} - \vec{r}' \right|} \right) dS', \tag{2.1.8}$$

where $\hat{n} \left(\vec{r}' \right)$ is the unit vector normal to the surface S_ϵ at $\vec{r}'$. We note that

$$dS' = \left| \vec{r} - \vec{r}' \right|^2 d\omega,$$

$$\nabla' \left(\frac{1}{\left| \vec{r} - \vec{r}' \right|} \right) = \frac{-\hat{n} \left(\vec{r}' \right)}{\left| \vec{r} - \vec{r}' \right|^2},$$

6

substituting this in the equation (2.1.8), we prove the relation expressed in the equation (2.1.6)

$$\int_V \frac{\vec{B}\left(\vec{r}'\right)}{4\pi} \nabla^2 \left(\frac{1}{\left|\vec{r}-\vec{r}'\right|}\right) d\Omega' \;=\; \frac{\vec{B}\left(\vec{r}\right)}{4\pi} \oint_{S_\epsilon} \hat{n}\left(\vec{r}'\right) \cdot \frac{-\hat{n}\left(\vec{r}'\right)}{\left|\vec{r}-\vec{r}'\right|^2} \left|\vec{r}-\vec{r}'\right|^2 d\omega$$

$$= \frac{-\vec{B}\left(\vec{r}\right)}{4\pi} \oint_{S_\epsilon} d\omega = -\vec{B}\left(\vec{r}\right).$$

∎

We see that the vector field $\vec{B}\left(\vec{r}'\right)$ must satisfy a Hölder condition the equation (2.1.7) to be valid. This requirement is stronger than continuity but less stringent than differentiability. All infinitely often differentiable functions in C^∞ satisfy this condition.

2.1.2   The Helmholtz theorem for a finite volume

For a bounded region the statement can be modified as follows

Theorem 4 (The Helmholtz theorem for a finite volume) *A general continuous three-vector field that is defined everywhere in a finite volume V of a Euclidean three-space and whose tangential and normal components on the bounding closed surface S are given may be uniquely represented as a sum of an irrotational part and a solenoidal part.*

Once again, the theorem implies that any vector field $\vec{B}\left(\vec{x}\right)$ can be written as

$$\vec{B} = -\nabla \phi_n + \nabla \times \vec{A}_t.$$

We now proceed to prove theorem 4, and obtain the explicit expressions for the vector potential $\vec{A}_t$ and the scalar potential ϕ_n in terms of the essential characteristics of the vector field, namely, divergence, curl, discontinuities, and boundary values. We adapt

the derivation from [62]. By using the equation (2.1.6) a vector function $\vec{B}(x, y, z)$ can be represented as

$$\vec{B}(\vec{r}) = -\int_V \frac{\vec{B}(\vec{r}')}{4\pi} \nabla^2 \left(\frac{1}{|r - r'|} \right) dV',$$

$$= -\nabla^2 \int_V \frac{\vec{B}(\vec{r}')}{4\pi |r - r'|} dV'. \tag{2.1.9}$$

Using the vector identity

$$\nabla \times \left(\nabla \times \vec{B} \right) = \nabla \left(\nabla \cdot \vec{B} \right) - \nabla^2 \vec{B},$$

we rewrite equation (2.1.9) as

$$\vec{B}(\vec{r}) = \nabla \times \left(\underbrace{\nabla \times \int_V \frac{\vec{B}(\vec{r}')}{4\pi |r - r'|} dV'}_{\vec{A}^t} \right) - \nabla \left(\underbrace{\nabla \cdot \int_V \frac{\vec{B}(\vec{r}')}{4\pi |r - r'|} dV'}_{\phi} \right). \tag{2.1.10}$$

We first consider the divergence term ϕ,

$$\phi = \int_V \frac{\vec{B}(\vec{r}')}{4\pi} \cdot \nabla \left(\frac{1}{|r - r'|} \right) dV'. \tag{2.1.11}$$

We note that

$$\vec{B}(\vec{r}') \cdot \nabla \left(\frac{1}{|r - r'|} \right) = -\vec{B}(\vec{r}') \cdot \nabla' \left(\frac{1}{|r - r'|} \right),$$

$$= \frac{\nabla' \cdot \vec{B}(\vec{r}')}{|r - r'|} - \nabla' \cdot \frac{\vec{B}(\vec{r}')}{|r - r'|},$$

substituting this in the equation (2.1.11) and using the divergence theorem for the second part of the volume integral,

$$\phi = \int_V \frac{\nabla' \cdot \vec{B}(\vec{r}')}{4\pi |r - r'|} dV' - \int_V \nabla' \cdot \frac{\vec{B}(\vec{r}')}{4\pi |r - r'|} dV',$$

$$= \int_V \frac{\nabla' \cdot \vec{B}(\vec{r}')}{4\pi |r - r'|} dV' - \oint_S \frac{\hat{n} \cdot \vec{B}(\vec{r}')}{4\pi |r - r'|} dS',$$

gives the desired form of the scalar potential ϕ. The curl term $\vec{A}_t$ in the equation (2.1.10) can be written as

$$
\begin{aligned}
\vec{A}_t &= \nabla \times \int_V \frac{\vec{B}\left(\vec{r'}\right)}{4\pi \left|r - r'\right|} dV', \\
&= -\frac{1}{4\pi} \int_V \vec{B}\left(\vec{r'}\right) \times \nabla \left(\frac{1}{\left|r - r'\right|}\right) dV', \\
&= \frac{1}{4\pi} \int_V \vec{B}\left(\vec{r'}\right) \times \nabla' \left(\frac{1}{\left|r - r'\right|}\right) dV'.
\end{aligned} \tag{2.1.12}
$$

We note that

$$
\nabla' \times \frac{\vec{B}\left(\vec{r'}\right)}{\left|r - r'\right|} = \frac{\nabla' \times \vec{B}\left(\vec{r'}\right)}{\left|r - r'\right|} - \vec{B}\left(\vec{r'}\right) \times \nabla' \left(\frac{1}{\left|r - r'\right|}\right),
$$

using this in equation (2.1.12) we get

$$
\vec{A}_t = \int_V \frac{\nabla' \times \vec{B}\left(\vec{r'}\right)}{4\pi \left|r - r'\right|} dV' - \frac{1}{4\pi} \int_V \nabla' \times \frac{\vec{B}\left(\vec{r'}\right)}{\left|r - r'\right|} dV'.
$$

For the second integral on the right hand side of the above equation we now show the following

$$
\frac{1}{4\pi} \int_V \nabla' \times \frac{\vec{B}\left(\vec{r'}\right)}{\left|r - r'\right|} dV' = -\frac{1}{4\pi} \oint_S \frac{\vec{n} \times \vec{B}\left(\vec{r'}\right)}{\left|r - r'\right|} dS'. \tag{2.1.13}
$$

To prove this result we consider a constant vector $\vec{C}$ and apply the divergence theorem to the quantity $\vec{C} \cdot \nabla' \times \left(\vec{B}\left(\vec{r'}\right) / \left|r - r'\right|\right)$,

$$
\begin{aligned}
\int_V \vec{C} \cdot \nabla' \times \frac{\vec{B}\left(\vec{r'}\right)}{\left|r - r'\right|} dV' &= -\int_V \nabla' \cdot \mathbf{C} \times \frac{\vec{B}\left(\vec{r'}\right)}{\left|r - r'\right|} dV', \\
&= -\oint_S \vec{C} \times \frac{\vec{B}\left(\vec{r'}\right)}{\left|r - r'\right|} \cdot \vec{n} dS', \\
&= -\vec{C} \cdot \oint_S \frac{\vec{n} \times \vec{B}\left(\vec{r'}\right)}{\left|r - r'\right|} dS',
\end{aligned}
$$

since the constant vector $\vec{C}$ is arbitrary we prove the relation (2.1.13). Using this relation leads to the desired form of the vector potential $\vec{A}_t$,

$$\vec{A}_t = \int_V \frac{\nabla' \times \vec{B}\left(\vec{r'}\right)}{4\pi \left|r - r'\right|} dV' + \oint_S \frac{\vec{n} \times \vec{B}\left(\vec{r'}\right)}{4\pi \left|r - r'\right|} dS'.$$

Hence, the Helmholtz identity for any vector field $\vec{B}\left(\vec{r}\right)$ in a finite volume is

$$\vec{B}\left(\vec{r}\right) = -\nabla \left[\int_V \frac{\nabla' \cdot \vec{B}\left(\vec{r'}\right)}{4\pi \left|r - r'\right|} dV' - \oint_S \frac{\vec{n} \cdot \vec{B}\left(\vec{r'}\right)}{4\pi \left|r - r'\right|} dS' \right]$$
$$+ \nabla \times \left[\int_V \frac{\nabla' \times \vec{B}\left(\vec{r'}\right)}{4\pi \left|r - r'\right|} dV' + \oint_S \frac{\vec{n} \times \vec{B}\left(\vec{r'}\right)}{4\pi \left|r - r'\right|} dS' \right].$$

2.1.3 The Helmholtz theorem for time dependent vector fields

Recent works [30, 82, 81] have extended the Helmholtz theorem to time dependent vector fields. We present a summary of some of those recent works here.

It is possible to obtain the Helmholtz theorem and an explicit form of the scalar and vector time dependent potentials by replacing the three dimensional analysis on the Euclidian three space in the sections 2.1.1 and 2.1.2 with a four-vector equivalent on the Euclidian four space $\mathbb{E}^4$, or the Minkowski four-space $\mathbb{R}^{3+1}$ [81, 80]. However, the approach we describe below is more suitable for our purposes, as it allows us to not only obtain the Helmholtz theorem for the time dependent vector field but also to obtain Maxwell's equation starting from the Helmholtz theorem and the continuity equation.

Let $f\left(\vec{r}, t\right)$ be a time dependent scalar function and let $g\left(\vec{r}, t\right)$ be a time dependent scalar function defined by

$$g\left(\vec{r}, t\right) = \int \frac{f\left(\vec{r'}, t - \left|\vec{r} - \vec{r'}\right|/c\right)}{4\pi \left|\vec{r} - \vec{r'}\right|} dV', \tag{2.1.14}$$

where c is a constant. We introduce the notation, $\vec{R} = \vec{r} - \vec{r}'$, $R = |\vec{R}|$, $\psi(R) = 1/(4\pi R)$, and $\tau = t - R/c$. Using this notation, the equation (2.1.14) can be written as

$$g(\vec{r},t) = \int f\left(\vec{r}',\tau\right)\psi(R)\,dV'. \tag{2.1.15}$$

The gradient of g and its divergence, i.e., the Laplacian of g can be given as

$$\nabla g(\vec{r},t) = \int (\psi \nabla f + f \nabla \psi)\,dV',$$

$$\nabla^2 g(\vec{r},t) = \int \left(\psi \nabla^2 f + 2\nabla f \cdot \nabla \psi + f \nabla^2 \psi\right)\,dV'$$

The gradient of the scalar function f and ψ are given by

$$\nabla f = -\frac{1}{c}\frac{\partial f}{\partial \tau}\hat{e}_R, \tag{2.1.16}$$

$$\nabla \psi = -\frac{1}{R}\psi\hat{e}_R,$$

and taking the divergence of ∇f, we obtain

$$\nabla^2 f = \frac{1}{c^2}\frac{\partial^2 f}{\partial^2 \tau} - \frac{2}{cR}\frac{\partial f}{\partial \tau}. \tag{2.1.17}$$

Using the equations (2.1.16) and (2.1.17), the Laplacian of g can be given as

$$\nabla^2 g(\vec{r},t) = \int \frac{1}{c^2}\frac{\partial^2 f\left(\vec{r}',\tau\right)}{\partial \tau^2}\psi(R)\,dV' + \int f\left(\vec{r}',\tau\right)\nabla^2\psi dV'. \tag{2.1.18}$$

We apply the equation (2.2.4) derived in the section 2.1.2 to the three dimensional vector field with one of its components being $f(\vec{r},\tau)$ and other two being zero to obtain

$$\int f\left(\vec{r}',\tau\right)\nabla^2\psi dV' = -f(\vec{r},t). \tag{2.1.19}$$

Now, by changing the differentiation with respect to τ in the first term on the right hand side of the equation (2.1.18) to differentiation with respect to t, and bringing the differentiation with respect to t outside the integral, and using equations (2.1.19) and (2.1.15) we obtain

$$\nabla^2 g(\vec{r},t) = \frac{1}{c^2}\frac{\partial^2 g(\vec{r},t)}{\partial t^2} - f(\vec{r},t).$$

11

We can now rewrite the equation above as

$$\left(\nabla^2 - \frac{1}{c^2}\frac{\partial^2}{\partial t^2}\right) g\left(\vec{r}, t\right) = -f\left(\vec{r}, t\right). \tag{2.1.20}$$

We now consider a time dependent vector function $\vec{F}\left(\vec{r}, t\right)$ and define a vector potential $\vec{A}\left(\vec{r}, t\right)$ by

$$\vec{A}\left(\vec{r}, t\right) = \int \vec{F}\left(\vec{r}', \tau\right) \psi\left(R\right) dV', \tag{2.1.21}$$

and using the equation (2.1.20) component-wise for the vector $\vec{A}$, we get

$$\left(\nabla^2 - \frac{1}{c^2}\frac{\partial^2}{\partial t^2}\right) \vec{A}\left(\vec{r}, t\right) = -\vec{F}\left(\vec{r}, t\right). \tag{2.1.22}$$

We now define a scalar potential ϕ associated with $\vec{F}\left(\vec{r}, t\right)$ such that it is a solution to

$$\frac{1}{c^2}\frac{\partial \phi\left(\vec{r}, t\right)}{\partial t} = -\nabla \cdot \vec{A}\left(\vec{r}, t\right). \tag{2.1.23}$$

The equation above is the well-known Lorenz gauge condition. We now use the standard vector identity for the double curl of a vector field on the vector $\vec{A}$ and use the equations (2.1.23) and (2.1.22) to get

$$
\begin{aligned}
\nabla \times \left(\nabla \times \vec{A}\left(\vec{r}, t\right)\right) &= \nabla\left(\nabla \cdot \vec{A}\left(\vec{r}, t\right)\right) - \nabla^2 \vec{A}\left(\vec{r}, t\right) \\
&= \nabla\left(-\frac{1}{c^2}\frac{\partial \phi\left(\vec{r}, t\right)}{\partial t}\right) - \left(\frac{1}{c^2}\frac{\partial^2 \vec{A}\left(\vec{r}, t\right)}{\partial t^2} - \vec{F}\left(\vec{r}, t\right)\right) \\
&= -\frac{1}{c^2}\frac{\partial}{\partial t}\left(\nabla \phi\left(\vec{r}, t\right) + \frac{\partial \vec{A}\left(\vec{r}, t\right)}{\partial t}\right) + \vec{F}\left(\vec{r}, t\right).
\end{aligned}
$$

Rearranging the equation above we arrive at the *Helmholtz theorem for time dependent vector fields,*

$$\vec{F} = \frac{1}{c^2}\frac{\partial}{\partial t}\left(\nabla \phi + \frac{\partial \vec{A}}{\partial t}\right) + \nabla \times \left(\nabla \times \vec{A}\right).$$

Now we derive additional relations which would facilitate the derivation of Maxwell's equations from the Helmholtz theorem in the section 2.1.4. Starting from

12

the equation (2.1.21), we evaluate the divergence of $\vec{A}$ to obtain

$$
\begin{aligned}
\nabla \cdot \vec{A}\left(\vec{r}, t\right) &= \int \nabla \cdot \left[\psi\left(R\right) \vec{F}\left(\vec{r}', \tau\right)\right] dV' \\
&= \int \left[-\nabla'\psi \cdot \vec{F} + \psi\nabla \cdot \vec{F}\right] dV' \\
&= \int \left[-\nabla' \cdot \left(\psi\vec{F}\right) + \psi\nabla' \cdot \vec{F} + \psi\nabla \cdot \vec{F}\right] dV' \\
&= \underbrace{\int -\nabla' \cdot \left(\psi\vec{F}\right) dV'}_{I} + \int \left[\nabla' \cdot \vec{F} + \nabla \cdot \vec{F}\right] \psi dV'.
\end{aligned}
$$

Using the divergence theorem, we can write the integral I as

$$
I = \int -\nabla' \cdot \left(\psi\vec{F}\right) dV' = -\oint \psi\vec{F} \cdot d\vec{S}'.
$$

Assuming that the vector function $\vec{F}$ vanishes sufficiently fast as $r \to \infty$, we see that the integral I vanishes. Thus, we have

$$
\nabla \cdot \vec{A}\left(\vec{r}, t\right) = \int \left[\nabla' \cdot \vec{F}\left(\vec{r}', \tau\right) + \nabla \cdot \vec{F}\left(\vec{r}', \tau\right)\right] \psi dV'.
$$

We rewrite $\nabla' \cdot \vec{F}$ and $\nabla \cdot \vec{F}$ as

$$
\begin{aligned}
\nabla' \cdot \vec{F}\left(\vec{r}', \tau\right) &= \sum_{i=1}^{3} \left[\frac{\partial \vec{F}_i\left(\vec{r}', \tau\right)}{\partial x_i'} + \frac{\partial \vec{F}_i\left(\vec{r}', \tau\right)}{\partial \tau} \frac{\partial \tau}{\partial x_i'}\right], \\
\nabla \cdot \vec{F}\left(\vec{r}', \tau\right) &= \sum_{i=1}^{3} \left[\frac{\partial \vec{F}_i\left(\vec{r}', \tau\right)}{\partial \tau} \frac{\partial \tau}{\partial x_i}\right].
\end{aligned}
$$

We note that $\left(\partial\tau/\partial x_i'\right) = -\left(\partial\tau/\partial x_i\right)$. Using this, we can conclude that

$$
\begin{aligned}
\nabla \cdot \vec{A}\left(\vec{r}, t\right) &= \int \left[\sum_{i=1}^{3} \frac{\partial \vec{F}_i\left(\vec{r}', \tau\right)}{\partial x_i'}\right] \psi dV' \\
&= \int \left[\nabla'_\tau \cdot \vec{F}\right] \psi dV', \tag{2.1.24}
\end{aligned}
$$

where the notation ∇'_τ is the gradient operator with respect to x_i' with τ kept constant, for $i = 1, 2, 3$. The scalar potential in the Lorenz gauge equation (2.1.23) can be

13

expressed in terms on another scalar function $\rho_a(r,t)$ as

$$\phi(\vec{r},t) = \int \rho_a\left(\vec{r}',\tau\right)\psi(R)\,dV',\qquad(2.1.25)$$

and also from the equation (2.1.20), the scalar potential $\phi(\vec{r},t)$ also satisfies

$$\left(\nabla^2 - \frac{1}{c^2}\frac{\partial^2}{\partial t^2}\right)\phi(\vec{r},t) = -\rho_a(\vec{r},t).\qquad(2.1.26)$$

Using the equations (2.1.24) and (2.1.23) and assuming that the time derivative can be exchanged with the spatial integral, we get

$$\frac{\partial\rho_a(\vec{r},t)}{\partial t} = -c^2\nabla\cdot\vec{F}(\vec{r},t).\qquad(2.1.27)$$

2.1.4 Maxwell's equations from the Helmholtz theorem

We will now obtain Maxwell's equations using the Helmholtz theorem for time dependent vector fields and the continuity equation

$$\nabla\cdot\vec{J}(\vec{r},t) + \frac{\partial\rho(\vec{r},t)}{\partial t} = 0,\qquad(2.1.28)$$

where $\vec{J}(\vec{r},t)$ is the current density vector and $\rho(\vec{r},t)$ is the charge density at point $\vec{r}$ and at time t.

We start from the Helmholtz theorem for time dependent potentials

$$\vec{F} = \frac{1}{c^2}\frac{\partial}{\partial t}\left(\nabla\phi + \frac{\partial\vec{A}}{\partial t}\right) + \nabla\times\left(\nabla\times\vec{A}\right).\qquad(2.1.29)$$

We choose $\vec{F}(\vec{r},t)$ to be $\mu_0\vec{J}(\vec{r},t)$, where μ_0 is permeability of the free space. Using the equation (2.1.21), we see that the vector potential $\vec{A}$ can be written as

$$\vec{A} = \int \frac{\mu_0\vec{J}\left(\vec{r}',\tau\right)}{4\pi R}\,dV',$$

and using the equation (2.1.27), we get

$$\begin{aligned}\frac{\partial\rho_a(\vec{r},t)}{\partial t} &= -c^2\nabla\cdot\mu_0\vec{J}(\vec{r},t)\\ &= -\mu_0 c^2\nabla\cdot\vec{J}(\vec{r},t) = \mu_0 c^2\frac{\partial\rho(\vec{r},t)}{\partial t}.\end{aligned}\qquad(2.1.30)$$

14

In the equation (2.1.30) we use the continuity equation (2.1.28). We now attribute a meaning to the constant c as the speed of light, and $c = 1/\sqrt{\mu_0 \epsilon_0}$, and ϵ_0 is the permittivity of free space. We thus get

$$\rho_a\left(\vec{r}, t\right) = \frac{\rho\left(\vec{r}, t\right)}{\epsilon_0}. \tag{2.1.31}$$

Using the equation (2.1.25), we define ϕ, the electric scalar potential, as

$$\phi\left(\vec{r}, t\right) = \int \frac{\rho\left(\vec{r}', \tau\right)}{4\pi\epsilon_0 R} dV'.$$

Additionally, we now define two new quantities. The electric field intensity $\vec{E}\left(\vec{r}, t\right)$ is defined as

$$\vec{E}\left(\vec{r}, t\right) = -\left(\nabla\phi\left(\vec{r}, t\right) + \frac{\partial \vec{A}\left(\vec{r}, t\right)}{\partial t}\right), \tag{2.1.32}$$

and the magnetic induction $\vec{B}\left(\vec{r}, t\right)$ is defined by

$$\vec{B}\left(\vec{r}, t\right) = \nabla \times \vec{A}\left(\vec{r}, t\right).$$

From the definition of $\vec{B}\left(\vec{r}, t\right)$ it follows that the divergence of $\vec{B}\left(\vec{r}, t\right)$ vanishes, that is,

$$\nabla \cdot \vec{B}\left(\vec{r}, t\right) = 0. \tag{2.1.33}$$

Now the equation (2.1.29) becomes the Ampere-Maxwell equation

$$\nabla \times \vec{B}\left(\vec{r}, t\right) = \mu_0 \vec{J}\left(\vec{r}, t\right) + \frac{1}{c^2}\frac{\partial \vec{E}\left(\vec{r}, t\right)}{\partial t}. \tag{2.1.34}$$

Taking the curl of both sides of the equation (2.1.32) and using the definition of $\vec{B}\left(\vec{r}, t\right)$, we get

$$\nabla \times \vec{E}\left(\vec{r}, t\right) = -\frac{\partial \vec{B}\left(\vec{r}, t\right)}{\partial t} \tag{2.1.35}$$

Taking the divergence of both side of the equation (2.1.32) and using the equations

(2.1.23), (2.1.26) and (2.1.31), we get

$$
\begin{aligned}
\nabla \cdot \vec{E}\left(\vec{r}, t\right) &= -\nabla^2 \phi\left(\vec{r}, t\right) - \frac{\partial}{\partial t}\left[\nabla \cdot \vec{A}\left(\vec{r}, t\right)\right] \\
&= -\nabla^2 \phi\left(\vec{r}, t\right) - \frac{\partial}{\partial t}\left[-\frac{1}{c^2}\frac{\partial \phi\left(\vec{r}, t\right)}{\partial t}\right] \\
&= -\left(\nabla^2 - \frac{1}{c^2}\frac{\partial^2}{\partial t^2}\right)\phi\left(\vec{r}, t\right) = \frac{\rho\left(\vec{r}, t\right)}{\epsilon_0}.
\end{aligned}
\tag{2.1.36}
$$

We have derived Maxwell's equations (2.1.36), (2.1.35), (2.1.33), and (2.1.34) starting from the Helmholtz theorem (2.1.29) and the continuity equation (2.1.30).

2.2   Laplace's and Poisson's equations

A vector field that is both solenoidal and irrotational and is continuously differentiable is called a Laplacian vector field. Since this field is irrotational, there is a potential ϕ such that

$$
\vec{B} = -\nabla\phi,
$$

and since the field is solenoidal and continuously differentiable, this potential satisfies **Laplace's equation**,

$$
\nabla^2 \phi = \frac{\partial^2 \phi}{\partial x^2} + \frac{\partial^2 \phi}{\partial y^2} + \frac{\partial^2 \phi}{\partial z^2} = 0,
\tag{2.2.1}
$$

the corresponding inhomogenous equation is called **Poisson's equation**,

$$
-\nabla^2 \phi = f.
\tag{2.2.2}
$$

Laplace's and Poisson's equations describe a wide variety of physical processes, e.g. the gravitational potential, the electrostatic potential, the magnetostatic potential, chemical concentrations, steady-state heat conduction, steady-state diffusion of a solute, steady-state irrotational flow of the incompressible fluids, and the probabilistic investigation of Brownian motion. In a typical interpretation, ϕ denotes the density of some quantity in equilibrium, as in the case of an electric potential. Laplace's equation is equivalent to the requirement that there be no maximum or minimum of

ϕ inside the volume V and the value of ϕ at a point be equal to the average of the values of ϕ at the neighboring points.

A C^2 function that satisfies Laplace's equation is called a *harmonic function*. In this section we discuss properties of harmonic functions which are relevant to the work that we present. All theorems presented are valid over $\mathbb{R}^n$, but since the problems that we address are all in two or three dimensions we restrict our attention to the special case $n = 2$ or $n = 3$. We also discuss the established techniques to solve Laplace's and Poisson's equations. The material presented here is adapted from [36].

2.2.1 Fundamental solution and Green's functions

In the section 2.1.1 we proved that for any vector field $\vec{B}(\vec{r})$ the vector potential $\vec{V}(\vec{r})$ given by

$$\vec{V}(\vec{r}) = - \int_{\mathbb{E}3} \frac{\vec{B}\left(\vec{r}'\right)}{4\pi \left|\vec{r} - \vec{r}'\right|} d\Omega',\qquad (2.2.3)$$

is a solution to the vector Poisson equation $\vec{B} = -\nabla^2 \vec{V}$. In the equation above, irrespective of what the vector field $\vec{B}(\vec{r})$ is, the kernel of the volume integral, $1/\left(4\pi \left|\vec{r} - \vec{r}'\right|\right)$, will always remain the same. This observation leads us to define the fundamental solution Φ of the Laplace equation as

$$\Phi(\vec{r}) = 1/\left(4\pi \left|\vec{r}\right|\right).$$

We can also arrive at a fundamental solution by finding an explicit solution to the Laplace equation with certain symmetry properties [36]. For a two dimensional case it can be easily shown that a fundamental solution is given by $\Phi(\vec{r}) = -\left(\log \left|\vec{r}\right|\right)/(2\pi)$. The fundamental solution Φ has a property that it is invariant under rotation and it is singular at origin. Using the notation for the fundamental solution the equation (2.2.3) can be written as a convolution integral

$$\vec{V}(\vec{r}) = - \int_{\mathbb{E}3} \Phi\left(\vec{r} - \vec{r}'\right) \vec{B}\left(\vec{r}'\right) d\Omega'.$$

17

We see that the recognizing the fundamental solution of the Laplace equation allows us to construct the solution to the more complicated Poisson equation using a convolution integral.

The Green's function is a fundamental solutions that also satisfy boundary conditions or initial conditions. To discuss Green's function it will be useful to first present Green's formula.

Theorem 1 (Green's Formulas) *Let $\phi, \psi \in C^2$ on a closed domain $U \subset \mathbb{E}^3$. Then*

1. $\int_U \nabla^2 \phi \, dV = \int_{\partial U} \frac{\partial \phi}{\partial \nu} dS$

2. $\int_U \nabla \phi \cdot \nabla \psi \, dV = -\int_{\partial U} \phi \nabla^2 \psi \, dV + \int_{\partial U} \phi \frac{\partial \psi}{\partial \nu} dS$

3. $\int_U \left[\phi \nabla^2 \psi - \psi \nabla^2 \phi \right] dV = \int_{\partial U} \left[\phi \frac{\partial \psi}{\partial \nu} - \psi \frac{\partial \phi}{\partial \nu} \right] dS$

All three Green's formulas above can be easily proved using the divergence theorem [36]. Greens's formulas along with the definition of Green's function can be used to prove the uniqueness of the solution for certain boundary value problems. We now formally define Green's function.

Definition 2 (Green's function) *Green's function for the region U is of the form*

$$G\left(\vec{r}, \vec{r}'\right) = \Phi\left(\vec{r} - \vec{r}'\right) - \Psi\left(\vec{r}, \vec{r}'\right), \qquad (2.2.4)$$

where $\Phi\left(\vec{r} - \vec{r}'\right)$ is a fundamental solution and Ψ is a harmonic function.

The boundary conditions will depend on the problem. For the special case of the Dirichlet and the Neumann boundary condition, it can be shown using the definition of Green's function and Green's formulas that the unique solution can be found for the Poisson problem $-\nabla^2 \phi = \rho$ in U. The solution to this problem can be expressed as

$$\phi\left(\vec{r}\right) = \int_U \rho\left(\vec{r}'\right) G\left(\vec{r}, \vec{r}'\right) dV + \int_{\partial U} \left[G\left(\vec{r}, \vec{r}'\right) \frac{\partial \phi\left(\vec{r}'\right)}{\partial \nu'} - \phi\left(\vec{r}'\right) \frac{\partial G\left(\vec{r}, \vec{r}'\right)}{\partial \nu'} \right] dS'$$

For the Dirichlet boundary conditions where the potential ϕ is specified on the boundary ∂U, Green's function can be chosen to be

$$G\left(\vec{r}, \vec{r}'\right) = 0 \text{ on the boundary } \partial U,$$

and for the Neumann boundary conditions where the normal component of the gradient of the potential ϕ is specified on the boundary ∂U, Green's function can be chosen to be

$$\frac{\partial G\left(\vec{r}, \vec{r}'\right)}{\partial \nu'} = 0 \text{ on the boundary } \partial U.$$

Green's function is uniquely determined by the equation (2.2.4) and the boundary conditions. Green's function is symmetric with respect to $\vec{r}$ and $\vec{r}'$, $G\left(\vec{r}, \vec{r}'\right) = G\left(\vec{r}', \vec{r}\right)$. Except for few simple geometries, like the half-plane and the sphere, it is usually very hard to find Green's functions. For many problems Green's function may not exist or may not be uniquely determined.

2.2.2   Mean-value formulas

Consider an open set $U \subset \mathbb{E}^3$ and suppose ϕ is a harmonic function within U. Let $S\left(\vec{r}_0, R\right)$ denote a ball at $\vec{r}_0$ with radius R in U. The mean-value formulas declare that $\phi\left(\vec{r}_0\right)$ equals both the average of ϕ over the ball $\partial S\left(\vec{r}_0, R\right)$ and the average of ϕ over the entire ball $S\left(\vec{r}_0, R\right)$.

Theorem 3 (*Mean-value formulas for 3D Laplace's equation*). *If $\phi \in C^2\left(U\right)$ is harmonic, then*

$$\phi\left(\vec{r}_0\right) = \frac{1}{4\pi R^2} \oint_{\partial S(\vec{r}_0, R)} \phi \, ds = \frac{3}{4\pi R^3} \int_{S(\vec{r}_0, R)} \phi \, d\Omega \qquad (2.2.5)$$

for each sphere of radius R with center at point $\vec{r}_0$, $S\left(\vec{r}_0, R\right) \subset U$.

The converse of this theorem is also true. One of the consequences of the mean value theorem is that the maximum or a minimum of a Harmonic function can occur

only on the boundary. If the function has a maximum or minimum inside U then the function is just a constant. This result provides another way to establish uniqueness of solutions in certain boundary value problems for Poisson's equation.

Regularity

The regularity theorem says that if $\phi \in C^2$ is harmonic, then necessarily $\phi \in C^\infty$. Thus harmonic functions are automatically infinitely often differentiable. Even though the Laplace equations itself has only second order partial derivatives it has the interesting feature that the all partial derivatives of the solution ϕ exist.

Analyticity

An analytic function ϕ is an infinitely differentiable function such that the Taylor series around any point x_0

$$T(x) = \sum_{n=0}^{\infty} \frac{\phi^n(x_0)}{n!}(x - x_0)^n,$$

is convergent for x close enough to x_0, and its value equals $\phi(x)$. The analyticity theorem states

Theorem 4 (Analyticity) *Assume ϕ is harmonic in U. Then ϕ is analytic in U.*

This property allows us to express a harmonic function ϕ as a Taylor series.

The last important property is the **Harnack's inequality**, which assert that the values of a non-negative harmonic function within V are all comparable. The value of a harmonic function ϕ cannot be very small or very large at any point of V unless ϕ is very small or very large everywhere in V.

2.2.3 An analytical solution of the 2D Laplace equation

Let $z = x+iy$, $dz = dx+idy$ and $d\bar{z} = dx-idy$. Then, $(\partial/\partial\bar{z}) = \frac{1}{2}((\partial/\partial x) + i(\partial/\partial y))$ and $(\partial/\partial z) = \frac{1}{2}((\partial/\partial x) - i(\partial/\partial y))$. The Laplacian operator in 2D can be given as

$\Delta = 4 \left(\partial / \partial \bar{z} \right) \left(\partial / \partial z \right)$. For any C^1 complex function f on a complex domain Ω with boundary $\partial \Omega$, the *Cauchy-Pompeiu integral representation* can be written as

$$f(z_0) = \frac{1}{2\pi i} \int_{\partial \Omega} \frac{f(z)}{z - z_0} dz - \frac{1}{\pi} \int \int_{\Omega} \frac{(\partial f / \partial \bar{z})}{z - z_0} dx dy. \qquad (2.2.6)$$

If the function f is analytic then it satisfies the Cauchy-Riemann equation $(\partial f / \partial \bar{z}) = 0$, and the equation (2.2.6) reduces to the standard Cauchy's formula

$$f(z_0) = \frac{1}{2\pi i} \int_{\partial \Omega} \frac{f(z)}{z - z_0} dz.$$

Cauchy's formula tells us that the value f at any point z_0 in Ω is completely determined by the value of f on the boundary $\partial \Omega$. This can also be used to develop a numerical scheme to solve the 2D Laplace equation.

2.2.4 Analytical and numerical solutions of the 3D Laplace equation

A solution of Laplace's equation is uniquely determined if the value of the function is specified everywhere on the boundary (Dirichlet boundary conditions) or the normal derivative of the function is specified everywhere on the boundary (Neumann boundary conditions) or a linear combination of the solution and its normal derivative is specified on the boundary (Robin boundary conditions). For many problems neither of the three boundary conditions above is suitable. We may then use the natural boundary conditions. Natural boundary conditions usually set the solution to a distinct value at infinity (asymptotic boundary conditions). The kind of boundary condition can vary from point to point on the boundary, but at any given point only one boundary condition can be specified. When the region on which the PDE problem is posed is unbounded, one or more of the above boundary conditions is usually replaced by a growth condition that limits the behavior of the solution at infinity.

Coordinate System	Solution Functions
Cartesian	Exponential, Circular and Hyperbolic functions
Circular cylindrical	Bessel, Exponential and Circular functions
Conical	Ellipsoidal harmonics and Power
Ellipsoidal	Ellipsoidal harmonic
Elliptic cylindrical	Mathieu and Circular function
Oblate spheroidal	Legendre polynomial and Circular function
Parabolic	Bessel and Circular function
Parabolic cylindrical	Bessel, Circular and Parabolic cylinder functions,
Paraboloidal	Circular function
Prolate spheroidal	Legendre polynomial and Circular function
Spherical	Legendre polynomial, Power and Circular functions

Table 2.2.1. Analytic solution functions for different coordinate systems where the method of seperation of variables can be applied.

The method of separation of variables

The method of separation of variables is a suitable technique for determining solutions to linear PDEs, usually with constant coefficients, when the domain is bounded in at least one of the independent variables. It turns out that in the three-dimensional Laplace's equation, there are some coordinate systems in which the solution takes on the form $R\left(\xi_1, \xi_2, \xi_3\right) \cdot X_1\left(\xi_1\right) \cdot X_2\left(\xi_2\right) \cdot X_3\left(\xi_3\right)$, where the additional factor R is independent of the separation constants. Laplace's equation can be solved by separation of variables in 11 coordinate systems [76, 59]. The form these solutions take is summarized in Table 2.2.1. In addition to these 11 coordinate systems, separation can be achieved in two additional coordinate systems by introducing a multiplicative factor.

In addition to the method of separation of variables, the finite Fourier transform and the power series method can be used to find an analytic solution to the Laplace and the Poisson boundary value problems.

Numerical methods

For all the electromagnetic problems that cannot be solved analytically, numerical methods are the only way to proceed. Most of the industrial packages are based on

one of the three classes of numerical techniques [6]:

The **finite difference method (FDM)** discretizes the differential operator at each point of a rectangular grid covering the entire region of interest. The differential operator is approximated by an algebraic expression (difference formula) with reference to the adjacent nodes. This leads to a large system of linear equations and the solution requires inversion of large and sparse matrices. The FDM usually utilizes uniformly spaced grids. The results usually are less accurate than other methods.

The **finite element method (FEM)** is based on division of the volume of space in which the Laplace or Poisson equation is satisfied into small volumes (the finite elements). Within each finite element a simple polynomial is used to approximate the solution. To obtain the polynomial a variational formulation over the volume is used. The variational quantity to be minimized is the total electrostatic or magnetostatic energy stored in a region. Element geometries and unknowns are expressed by polynomials with nodal values as coefficients. Relating these approximations to the operator equation through minimizing the energy functional yields the solution at the nodes. The FEM utilizes either uniform or nonuniform grids and it is possible to implement automatic mesh size control. Even though, this method is considered superior to FDM, but still suffers from some drawbacks. Among them are:

- The finite element techniques requires the mesh be extended to a reasonable distance with either potential or derivative boundary conditions applied to the outer surface, so that the truncation has an insignificant effect on the region of interest. This usually leads to a large number of finite elements.

- For problems where the magnetic or the electric field in the region of interest differ by a large ratio ($~10^6$) in the maximum and minimum value, the FEM elements have to start with extremely small element size and gradually adapt themselves to much larger element size. This will increase the number of unknowns substantially.

23

Most of these techniques using FDM or FEM utilize relatively low approximation order and provide solution as a data set in the region of interest. They also require a prohibitively large number of mesh points and careful meshing. Both FDM and FEM are geared to solve electric and magnetic potentials. Since in beam physics applications the knowledge of the values of electric or magnetic field is required, these values have to be extracted by numerical differentiation of the potential. But the numerical differentiation process is very sensitive to numerical, truncation and round off errors.

The **boundary element method (BEM)** or source based field models the field inside of a source free volume due to a real sources outside of it can be exactly replicated by a distribution of fictitious sources on its surface. The error due to discretization of the source falls off rapidly as the field point moves away from the source. Since the discretization is done only on the surface, the dimensionality of the problem is decreased by one. It makes the modeling of the problem easier and more user friendly. The trade off here is that the matrices generated by BEM are usually smaller and denser matrices. One technique that falls in this category is the image charge method. This requires proper choice of planes/grids to place point charges (or Gaussian distribution) and solve a large least square fit problem to find the charges. This involves a lot of guess work and computation time involved in getting the right solution. Knowing these charges, the potential and field can be directly computed everywhere in space. In problems where extreme ratios exist between smallest and largest details of the structure, BEM will be the method of choice. Finally, since the field and the potential everywhere in space are being computed from the actual charge distribution on the boundaries, it will result in extremely accurate results when this method is applied to particle ray tracing.

BEM methods are only applicable to problems for which Green's functions can be defined. This places considerable restrictions on the range and generality of problems

to which boundary elements can usefully be applied. And once again these methods usually compute the potential and not the field.

New methods that use the Helmholtz vector decomposition theorem are being used in recent years to overcome the difficulties encountered by the BEM. The techniques based on this method have the added benefits of giving the field directly and are particularly suitable for beam physics applications. The references [63, 74, 73, 72, 75] describe techniques based on this method to compute multipole decomposition of the fields. Other applications based on this method include vector tomography [60] and incompressible flows [33].

In beam physics, the detailed simulation of particle trajectories through magnets in spectrographs and other large acceptance devices requires the use of detailed field information obtained from measurements. Likewise, for high energy accelerators like the LHC, higher order description of the beam dynamic via one-turn maps is required to study the long term beam stability [69, 35]. The construction of such high order one-turn truncated Taylor maps [17] requires the precise information of the electromagnetic field in the individual electromagnetic components (quadrupoles, dipoles, sextupoles etc.) of the lattice.

It is commonly known that for a device that satisfies midplane symmetry, the entire field information can be extracted from the data in the midplane of the device [17]. However, it is well known that this method has limitations in accurately predicting nonlinear field information outside the immediate vicinity of the midplane because the extrapolation requires the computation of higher order derivatives of in-midplane data, which is difficult to do with accuracy if the data is based on measurements. Thus it is particularly useful to employ techniques that rely on field measurements outside the midplane. In particular, in modern particle spectrographs it is common to measure the fields on a fine mesh on 2 to 4 planes outside the midplane. These data have frequently been used to model the overall field as a superposition of point-charge

fields of so-called image charges [32, 18]. However, the computational effort required for this approach is large, as it requires the inversion of a matrix with a dimension equal to that of the number of image charges.

However, the out-of-plane field measurements in essence provide field data on the top and bottom surfaces of a box containing the region of interest through which the beam passes. If the planes extend outward far enough to a region where the fringe field becomes very small, or can easily be modeled, and inwards far enough that the field becomes rather homogenous, field data are known on an entire surface enclosing the region of interest. The method we present can extract the field information as a multipole expansion in the volume of interest if a discrete set of field measurements are provided on a closed surface enclosing the volume of interest.

2.3   The Differential Algebra $_nD_v$

For real analytic function f in v variables, we form a vector that contains all Taylor expansion coefficients at $\vec{x} = \vec{0}$ up to a certain order n. The vector with all the Taylor coefficients is called the DA vector. Knowing this vector for two real analytic functions f and g allows to compute the respective vector for $f + g$ and $f \cdot g$, since the derivatives of the sum and product function is uniquely defined from those of f and g. The resulting operations of addition and multiplication lead to an algebra, the so-called Truncated Power Series Algebra (TPSA) [7]. The power of TPSA can be enhanced by the introduction of the derivations ∂ and their inverses, corresponding to the differentiation and integration in the space of functions. This resulted in the recognition of the underlying differential algebraic structure and its exploitation, based on the commuting diagrams for the addition, multiplication, and differentiation

and their inverses:

$$
\begin{array}{ccccc}
f,g & \xrightarrow{\;T\;} & F,G & f,g & \xrightarrow{\;T\;} & F,G \\
{\scriptstyle +,-}\Big\downarrow & & \Big\downarrow{\scriptstyle \oplus,\ominus\,\cdot,/}\Big\downarrow & & & \Big\downarrow{\scriptstyle \odot,\oslash} \\
f\pm g & \xrightarrow[\;T\;]{} & F\overset{\oplus}{\ominus}G & f/g & \xrightarrow[\;T\;]{} & F\overset{\odot}{\oslash}G
\end{array}
\qquad (2.3.1)
$$

$$
\begin{array}{ccc}
f & \xrightarrow{\;T\;} & F \\
{\scriptstyle \partial,\partial^{-1}}\Big\downarrow & & \Big\downarrow{\scriptstyle \partial_{\bigcirc},\partial_{\bigcirc}^{-1}} \\
\partial f,\partial^{-1}f & \xrightarrow[\;T\;]{} & \partial_{\bigcirc}F,\partial_{\bigcirc}^{-1}F
\end{array}
$$

In the equation above the operation T is extraction of the Taylor coefficients of prespecified order n of the function. Thus, the operation T can be used to create a DA vector from a function. The operation T is an equivalence relation, and the application of T corresponds to the transition from the function to the equivalence class comprising all those functions with identical Taylor expansion to order n. The symbols $\oplus$, $\ominus$, $\odot$, $\oslash$, $\partial_{\bigcirc}$ and $\partial_{\bigcirc}^{-1}$ denote operations on the space of DA objects which are defined such that the commuting relation expressed in the equation (2.3.1) holds.

Using the Differential Algebra and analytic formulae to compute the n-th order derivative of an univariant fundamental function, like $\sin x, \cos x, \log x, \tan x$ etc., we can compute the derivatives up to order n of functions in v variables. The detailed description of obtaining the n-th order Taylor expansion for a multivariate function that is expressible on a computer is described in [17]. Also, composition of two multivariate functions can be defined using the DA. Many problems involving the use of DA techniques can be formulated as fixed-point problems, such as the inversion of a multivariate function. Here fixed point theorems can be applied to show that existence of the solution, and this also provides a practical means to obtain the solution [39].

As mentioned before the DA techniques have been widely applied in beam physics, asteroid problems and other problems involving the solution of ODEs or PDEs. The focus of the work we present is finding a solution to the Laplace and Poisson equation

using DA techniques. In this context it is worthwhile to look at the techniques that already use DA to solve PDEs [17].

2.3.1 Solution of PDEs using DA

The complicated PDEs for the fields and potentials stemming from the representation of Maxwell's equations in particle optical coordinates could be iteratively solved in the DA framework to any order in finitely many steps by rephrasing them in terms of a fixed-point problem [17, 54]. For example, consider the general PDE

$$a_1 \frac{\partial}{\partial x} \left(a_2 \frac{\partial \phi}{\partial x} \right) + b_1 \frac{\partial}{\partial y} \left(b_2 \frac{\partial \phi}{\partial y} \right) + c_1 \frac{\partial}{\partial z} \left(c_2 \frac{\partial \phi}{\partial z} \right) = 0,$$

where a_1, b_1, c_1, a_2, b_2, and c_2 are functions of x, y and z. The equation above can be written in fixed point form

$$\phi(x, y, z) = \phi|_{y=0} + \int_y \frac{1}{b_2} \left\{ \frac{\partial \phi}{\partial y}|_{y=0} - \int_y \left(\frac{a_1}{b_1} \frac{\partial}{\partial x} \left(a_2 \frac{\partial \phi}{\partial x} \right) + \frac{c_1}{b_1} \frac{\partial}{\partial z} \left(c_2 \frac{\partial \phi}{\partial z} \right) \right) \right\}.$$

If ϕ and $\partial \phi / \partial y$ are specified on the $y = 0$ plane then it is possible to iteratively calculate various high orders in y. Techniques based on the fixed point scheme for PDEs can be used to solve the Laplace equation when the potential ϕ and the normal derivative $\partial \phi / \partial y$ are specified e.g. on the midplane of a magnet. Also, by considering the Laplace equation in cylindrical coordinates, it is possible to devise a technique to obtain the magnetic field of a magnet with cylindrical symmetry when the field is specified on the central axis.

2.3.2 Taylor transfer maps

An ensemble of particles with similar coordinates is called a beam. Detailed understanding of the beam dynamics requires the study of the motion of the reference particle as well as the motion of the particle in the relative coordinates. The position and momenta are usually sufficient to describe the motion. The state vector is given

by

$$\vec{Z}(s) = (x, p_x, y, p_y, z, p_z),$$

where the point (x, y, z) and the momentum vector (p_x, p_y, p_z) gives the position and the momentum of a particle, and the arclength s along the reference orbit is used as the independent variable. The space spanned by the state vector is called phase space and the volume of the phase space is called emittance. At each point on the reference orbit it is possible to define an unique orthogonal coordinate system, denoted by $(\hat{e}_x, \hat{e}_y, \hat{e}_s)$, satisfying a certain set of conditions [50, 17]. In this coordinate system the motion of the particles in the beam can be described using relative coordinates, which are given by

$$\vec{Z}(s) = \begin{pmatrix} x \\ a = p_x/p_0 \\ y \\ b = p_y/p_0 \\ l = k(t - t_0) \\ \delta = (E - E_0)/E_0 \end{pmatrix}$$

where the position (x, y) describe the position of the particle in the local coordinate system, p_0 is a fixed momentum and E_0 and t_0 are the energy and the time of flight of the reference particle, a and b are the momentum slopes, E is the total energy, and k has a dimension of velocity which makes l a length like coordinate. The point $\vec{Z} = 0$ corresponds to the reference particle.

The transfer map or transfer function $\mathcal{M}$ relates initial conditions at s_0 to the conditions at s via

$$\vec{Z}(s) = \mathcal{M}(s_0, s)\left(\vec{Z}(s_0)\right).$$

Transfer maps are origin preserving, $\mathcal{M}\left(\vec{0}\right) = \vec{0}$, and the transfer maps have the property that

$$\mathcal{M}(s_1, s_2) \circ \mathcal{M}(s_0, s_1) = \mathcal{M}(s_0, s_2),$$

which says that the transfers maps of systems can be built up from the transfer maps of the pieces. For a deterministic system (a unique solution exists) the transfer map

is the flow of ODEs

$$\frac{d\vec{z}}{ds} = \vec{f}\left(\vec{z}, s\right), \tag{2.3.2}$$

in the independent variable s. For most dynamical systems, the transfer map can not be represented in a closed form. For weakly non-linear systems, like an accelerator system, the map can be expanded as a Taylor series. Usually, the Taylor expansion converges rapidly. Implementation of such a map on a computer would require the map to be truncated at a certain order. From the implementation point of view the Taylor transfer map is an array of DA vectors with each DA vector being an array storing the coefficients of the truncated Taylor series expansion of the final phase space coordinate in terms of the initial phase space coordinates. The Taylor transfer maps can be used to replace and speed up element-by-element tracking, to look at aberration content, or to monitor a design process [45]. A detailed discussion of the properties and use of the Taylor transfer maps can be found in [17].

Generating transfer maps

To generate a transfer map we have to solve the equation 2.3.2. For beam physics applications, the set of ODEs describing the equations of motion when the reference trajectory is restricted to a plane and the energy is conserved are given by

$$x' = a\left(1 + hx\right)\frac{p_0}{p_s},$$

$$y' = b\left(1 + hx\right)\frac{p_0}{p_s},$$

$$l' = \left\{\left(1 + hx\right)\frac{1 + \eta}{1 + \eta_0}\frac{p_0}{p_s} - 1\right\}\frac{k}{v_0},$$

$$a' = \left[\frac{1 + \eta}{1 + \eta_0}\frac{p_0}{p_s}\frac{E_x}{\chi_{e0}} + b\frac{B_z}{\chi_{m0}}\frac{p_0}{p_s} - \frac{B_y}{\chi_{m0}}\right] \cdot \left(1 + hx\right) + h\frac{p_0}{p_s},$$

$$b' = \left[\frac{1 + \eta}{1 + \eta_0}\frac{p_0}{p_s}\frac{E_y}{\chi_{e0}} + \frac{B_x}{\chi_{m0}} - a\frac{B_z}{\chi_{m0}}\frac{p_0}{p_s}\right] \cdot \left(1 + hx\right),$$

$$\delta' = 0, \tag{2.3.3}$$
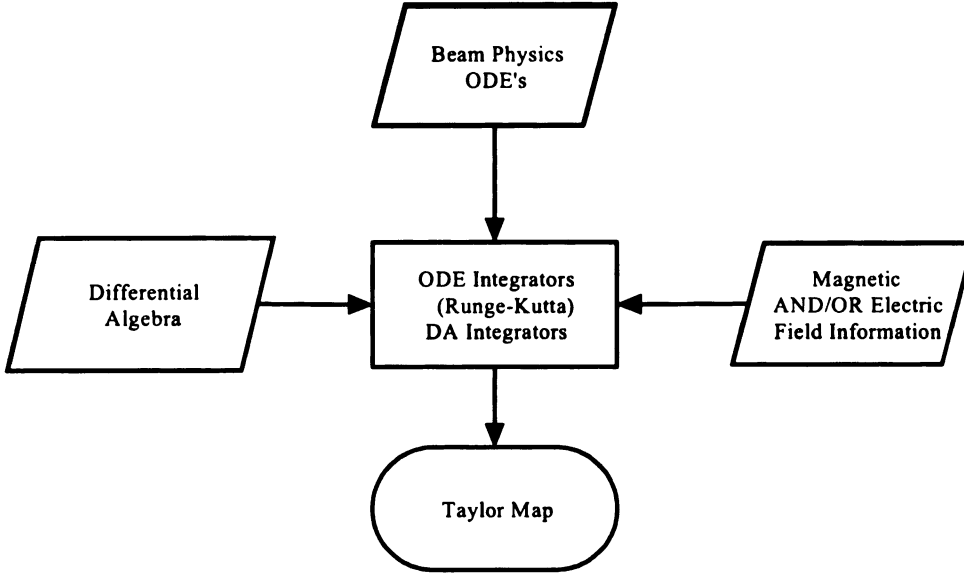
Figure 2.3.1. Flow chart for extracting the Taylor transfer maps from either the electric or the magnetic field information or both.

where h is the radius of curvature, the ratio p_0/p_s is given by

$$\frac{p_0}{p_s} = \left(\frac{\eta \, (2 + \eta)}{\eta_0 \, (2 + \eta_0)} \cdot \frac{m^2}{m_0^2} - a^2 - b^2 \right)^{-\frac{1}{2}} ,$$

the ratio η of the kinetic to rest mass energy is given by $\eta = (E - eV(x, y, s)) / (mc^2)$, the $\chi_{m0} = p_0/(ze)$ is the magnetic rigidity and $\chi_{e0} = (p_0 v_0) / (ze)$ is the electric rigidity. In the equation (2.3.3) B_x, B_y, B_z and E_x, E_y, E_z represent the x, y and z components of the magnetic field and the electric field.

Using the differential algebra and the knowledge of the magnetic and the electric field we can solve the equation (2.3.3) by using one of the ODE integration schemes. Figure 2.3.1 shows the flow chart for the extraction of transfer maps. Traditionally, it was only possible to extract the transfer maps to low orders (≤ 3), using the perturbative analytic approach. However, the introduction of differential algebra to beam physics has made it possible to extract maps to in principle arbitrary order. Further, the direct availability of the derivation ∂_i and their inverses ∂_i^{-1} allows

31

to devise efficient numerical integrators of any order. The code COSY INFINITY makes it possible to use DA integrators or a Runge-Kutta integrator of order eight with automatic step size control based on a seventh-order scheme for this purpose. The Runge-Kutta integration can be carried out not only with real numbers but also for DA vectors. At each time step the eighth order Runge-Kutta scheme requires the evaluation of the function $\vec{f}$ at thirteen points to compute the Taylor transfer map [51, 64, 48], which in turn requires the electric and magnetic field information at these thirteen points.

2.4 Taylor Models

Taylor model methods are newly developed techniques that unify many concepts of high-order computational differentiation with verification approaches covering the Taylor remainder term. These were developed as a better alternative to the conventional interval methods that have limited practical applicability. The reasons for the failure of conventional interval methods for large dimensional and domain size problems are discussed in [50, 42, 53]. The results obtained with Taylor model methods include verified optimization, verified quadrature and verified propagation of extended domains of initial conditions through ODEs, and approaches towards verified solution of DAEs and PDEs.

Definition 1 (Taylor Model) *Let $f : D \subset \mathbb{R}^v \longrightarrow \mathbb{R}$ be a function that is $(n + 1)$ times continuously partially differentiable on an open set containing the domain D. Let x_0 be a point in D and P the $n - th$ order Taylor polynomial of f around x_0. Let I be an interval such that*

$$f(x) \in P(x - x_0) + I \text{ for all } x \in D.$$

Then the pair (P, I) is called an $n - th$ order Taylor model of f around x_0 on D.

For the problems we discuss in this work the domain D is always $[-1,1]^v \subset \mathbb{R}^v$. A full theory of Taylor model arithmetic for elementary operations, intrinsic functions, initial value problems and functional inversion problems has been developed; see [50, 42, 53] and references therein. The arithmetic and the computational implementation is performed in such a way that the interval enclosure is mathematically rigorous, taking into account all round-off and threshold cut-off errors due to floating point arithmetic. Details about the verified implementation of arithmetic operation in the code COSY INFINITY can be found in [66, 53].

For the purposes of the further discussion, one particular intrinsic function, the so-called antiderivation, plays an important role. We note that a Taylor model for the integral with respect to variable i of a function f can be obtained from the Taylor model (P, I) of the function by merely integrating the part P_{n-1} of order up to order $n-1$ of the polynomial, and bounding the n-th order into the new remainder bound.

2.4.1   The Taylor Model integration scheme

We start out by defining the indefinite integration for a Taylor model in one variable and then proceed to define a special finite integral that we are going to use extensively in this work.

Definition 2 *For an n-th order Taylor model $T = (P, I)$ and $k = 1, \ldots, v$, let*

$$Q_k = \int_0^{x_k} P_{(n-1)} \left(x_1, \ldots, x_{k-1}, \xi_k, x_{k+1}, \ldots, x_v\right) d\xi_k.$$

The antiderivative ∂_k^{-1} of T is defined by

$$\partial_k^{-1}(P, I) = \left(Q_k, \left(B\left(P_{(n)} - P_{(n-1)}\right) + I\right) \cdot 2\right).$$

More details about the implementation of the anti-derivation operation can be found in [22].

Let $T^v = (P, I)$, be a $n-th$ order Taylor model in v variables. While solving PDEs we commonly encounter the finite integration

$$J^{(v-1)} = \int_{-1}^{1} T^v \left(x_1, \ldots x_{k-1}, \xi_k, x_{k+1}, \ldots, x_v \right) d\xi_k,$$

where $J^{(v-1)}$ is the resulting Taylor model of order n in $(v-1)$ variables, and $k = 1, \ldots, v$. We now describe the steps to compute the Taylor model $J^{(v-1)}$ using the antiderivative $\partial_{\xi_1}^{-1}$ operator.

1. Split the Taylor Model $T^v = (P, I)$ in to a polynomial P of order n and interval I.

2. Construct a new Taylor model $G^v = (P, I_\epsilon)$, where $I_\epsilon = [0, 0]$.

3. Apply the antiderivative operator $\partial_{\xi_1}^{-1}$ to the Taylor model G^v.

4. Evaluate the Taylor models $\partial_{\xi_1}^{-1} G^v$ (at $\xi_1 = 1$) and $\partial_{\xi_1}^{-1} G^v$ (at $\xi_1 = -1$) and subtract them to obtain a new Taylor model R^{v-1}.

5. Add the interval $2 \cdot I$ to the Taylor model R^{v-1} to give the Taylor model after integration with respect to the ξ_1 variable.

The steps 1 through 5 can be repeated for the integration in more than one variable.

2.4.2   An example of Taylor Model expansion

For a rectangular surface enclosing the volume of interest we now show the Taylor model expansion of the kernel $1/ \left(4\pi \left| \vec{r} - \vec{r}' \right| \right)$ over one surface element and one volume element. A point, $\vec{r} = (x, y, z)$, inside the volume element centered at (x_0, y_0, z_0) is described by

$$x = x_0 + 0.5 \cdot \lambda_1 \Delta x_v,$$

$$y = y_0 + 0.5 \cdot \lambda_2 \Delta y_v,$$

$$z = z_0 + 0.5 \cdot \lambda_3 \Delta z_v,$$

where Δx_v, Δy_v and Δz_v are the dimensions of the rectangular volume element and the parameters $\lambda_1, \lambda_2, \lambda_3 \in [-1, 1]$. A point, $\vec{r'} = \left(x', y', z' \right)$, on the surface element centered at (x_s, y_s, z_s) is described by

$$
\begin{aligned}
x' &= x_s + 0.5 \cdot \lambda_4 \Delta x_s, \\
y' &= y_s + 0.5 \cdot \lambda_5 \Delta y_s, \\
z' &= z_s,
\end{aligned}
$$

where Δx_s and Δy_s are the dimensions of the rectangular surface element and the parameters $\lambda_4, \lambda_5 \in [-1, 1]$. A schematic diagram of the rectangular volume element, rectangular surface element and the rectangular box enclosing the region of interest is shown in Figure 2.4.1.

For illustration we choose the volume element to be centered at $(1, 1, 1)$ and surface element at $(2, 2, 3)$ and $\Delta x_s = \Delta y_s = 1/16$ and $\Delta x_v = \Delta y_v = \Delta z_v = 1/8$. The Taylor model expansion of the kernel with respect to the parameters $\lambda_1, \lambda_2, \lambda_3, \lambda_4$ and λ_5 using Taylor model is given in tables 2.4.1 and 2.4.2. In the representation of the Taylor model expansion, the entries in the first column provide the number assigned to each of the coefficients in the Taylor model expansion to easily identify them. The entries in the second column provide the numerical value of the coefficients. The entries in the fourth through eighth provide the expansion orders with respect to the parameters $\lambda_1, \lambda_2, \lambda_3, \lambda_4$ and λ_5. The total order for each coefficient is the sum of all the orders in columns four through eight, which is given in the third column.

The Taylor Model integration of the kernel over the surface element, dS, can be expressed as

$$
\int_{dS} \frac{1}{4\pi} \frac{1}{\left| \vec{r} - \vec{r'} \right|} dy' dx' = \int_{-1}^{1} \int_{-1}^{1} \frac{1}{4\pi} \frac{1}{\left| \vec{r} - \vec{r'} \right|} d\lambda_4 d\lambda_5.
$$

Table 2.4.3 shows the Taylor model integration of the Taylor model expansion of the kernel given in tables 2.4.1 and 2.4.2.
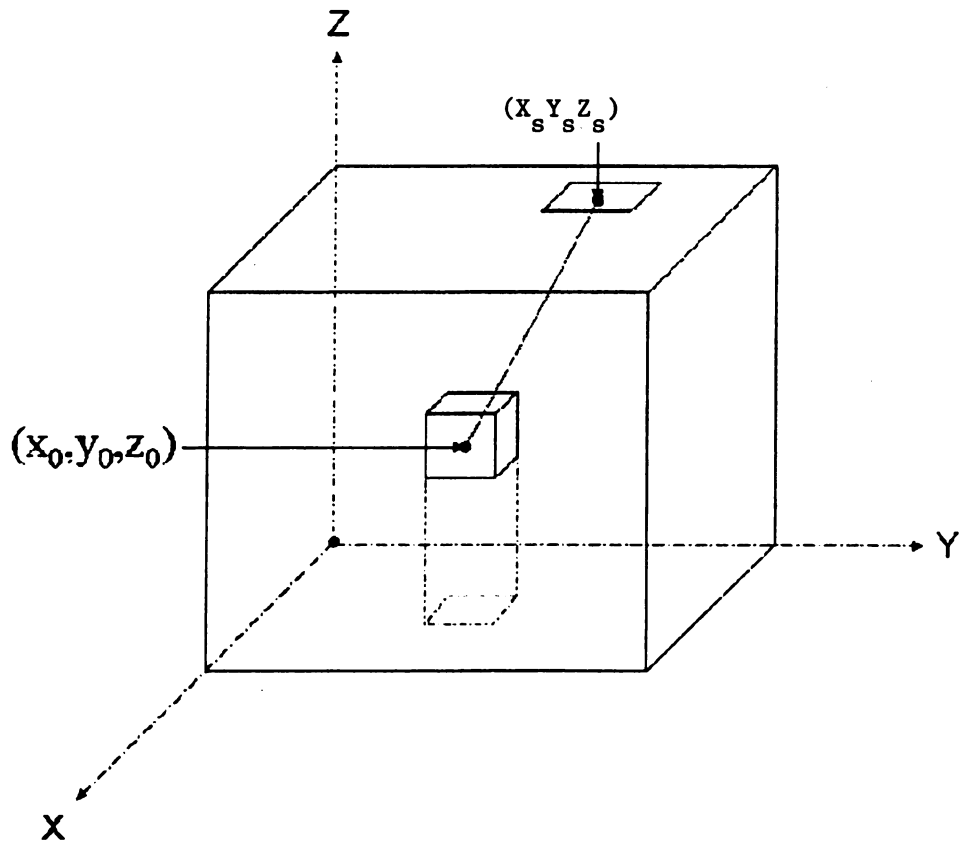
Figure 2.4.1. The figure shows a volume element centered at (x_0, y_0, z_0) element and a surface element (x_s, y_s, z_s).

```
 I   COEFFICIENT          ORDER EXPONENTS
 1   0.2012846454507073E-01  0   0 0  0 0  0
 2   0.1529273937765291E-03  1   1 0  0 0  0
 3   0.1529273937765291E-03  1   0 1  0 0  0
 4   0.2334154957641759E-03  1   0 0  1 0  0
 5   -.3823184844413227E-04  1   0 0  0 1  0
 6   -.3823184844413227E-04  1   0 0  0 0  1
 7   -.7724385987298169E-06  2   2 0  0 0  0
 8   0.3485629176768297E-05  2   1 1  0 0  0
 9   -.7724385987298169E-06  2   0 2  0 0  0
10   0.5320170848751610E-05  2   1 0  1 0  0
11   0.5320170848751610E-05  2   0 1  1 0  0
12   0.1544877197459632E-05  2   0 0  2 0  0
13   0.3862192993649084E-06  2   1 0  0 1  0
14   -.8714072941920742E-06  2   0 1  0 1  0
15   -.1330042712187903E-05  2   0 0  1 1  0
16   -.8714072941920742E-06  2   1 0  0 0  1
17   0.3862192993649084E-06  2   0 1  0 0  1
18   -.1330042712187903E-05  2   0 0  1 0  1
19   -.4827741242061355E-07  2   0 0  0 2  0
20   0.2178518235480185E-06  2   0 0  0 1  1
21   -.4827741242061355E-07  2   0 0  0 0  2
```

Table 2.4.1. The Taylor model expansion of the kernel. The coefficients up to second order are shown.

```
22   -.3526083774525404E-07    3    3 0  0 0  0
23   0.8876341263195013E-08    3    2 1  0 0  0
24   0.8876341263195013E-08    3    1 2  0 0  0
25   -.3526083774525404E-07    3    0 3  0 0  0
26   0.1354809982277133E-07    3    2 0  1 0  0
27   0.2021018196702667E-06    3    1 1  1 0  0
28   0.1354809982277133E-07    3    0 2  1 0  0
29   0.9690617197256710E-07    3    1 0  2 0  0
30   0.9690617197256710E-07    3    0 1  2 0  0
31   -.9032066548514218E-08    3    0 0  3 0  0
32   0.2644562830894053E-07    3    2 0  0 1  0
33   -.4438170631597507E-08    3    1 1  0 1  0
34   -.2219085315798754E-08    3    0 2  0 1  0
35   -.6774049911385670E-08    3    1 0  1 1  0
36   -.5052545491756669E-07    3    0 1  1 1  0
37   -.2422654299314178E-07    3    0 0  2 1  0
38   -.2219085315798754E-08    3    2 0  0 0  1
39   -.4438170631597507E-08    3    1 1  0 0  1
40   0.2644562830894053E-07    3    0 2  0 0  1
41   -.5052545491756669E-07    3    1 0  1 0  1
42   -.6774049911385670E-08    3    0 1  1 0  1
43   -.2422654299314178E-07    3    0 0  2 0  1
44   -.6611407077235133E-08    3    1 0  0 2  0
45   0.5547713289496883E-09    3    0 1  0 2  0
46   0.8467562389232092E-09    3    0 0  1 2  0
47   0.1109542657899377E-08    3    1 0  0 1  1
48   0.1109542657899377E-08    3    0 1  0 1  1
49   0.1263136372939167E-07    3    0 0  1 1  1
50   0.5547713289496883E-09    3    1 0  0 0  2
51   -.6611407077235133E-08    3    0 1  0 0  2
52   0.8467562389232092E-09    3    0 0  1 0  2
53   0.5509505897695944E-09    3    0 0  0 3  0
54   -.1386928322374221E-09    3    0 0  0 2  1
55   -.1386928322374221E-09    3    0 0  0 1  2
56   0.5509505897695944E-09    3    0 0  0 0  3
     -------------------------------------------------
VAR    REFERENCE POINT                    DOMAIN INTERVAL
  1  0.000000000000000     [-1.000000000000000    , 1.000000000000000     ]
  2  0.000000000000000     [-1.000000000000000    , 1.000000000000000     ]
  3  0.000000000000000     [-1.000000000000000    , 1.000000000000000     ]
  4  0.000000000000000     [-1.000000000000000    , 1.000000000000000     ]
  5  0.000000000000000     [-1.000000000000000    , 1.000000000000000     ]
              REMAINDER BOUND INTERVAL
  R      [-.6787457395636954E-007,0.1769369034586471E-006]
 ***********************************************************
```

Table 2.4.2. The Taylor model expansion of the kernel. The third order coefficients, the reference points and the remainder bound interval are shown.

```
I   COEFFICIENT             ORDER EXPONENTS
1   0.1965667222668859E-04    0    0 0  0 0  0
2   0.1493431579848917E-06    1    1 0  0 0  0
3   0.1493431579848917E-06    1    0 1  0 0  0
4   0.2279448200822031E-06    1    0 0  1 0  0
5  -.7543345690720868E-09     2    2 0  0 0  0
6   0.3403934742937790E-08    2    1 1  0 0  0
7  -.7543345690720868E-09     2    0 2  0 0  0
8   0.5195479344483994E-08    2    1 0  1 0  0
9   0.5195479344483994E-08    2    0 1  1 0  0
10  0.1508669138144172E-08    2    0 0  2 0  0
   ---------------------------------------------
VAR   REFERENCE POINT                    DOMAIN INTERVAL
 1   0.000000000000000    [-1.000000000000000    , 1.000000000000000    ]
 2   0.000000000000000    [-1.000000000000000    , 1.000000000000000    ]
 3   0.000000000000000    [-1.000000000000000    , 1.000000000000000    ]
 4   0.000000000000000    [-1.000000000000000    , 1.000000000000000    ]
 5   0.000000000000000    [-1.000000000000000    , 1.000000000000000    ]
            REMAINDER BOUND INTERVAL
 R     [-.1628051142682157E-008,0.2054209443924109E-008]
*********************************************************
```

Table 2.4.3. The Taylor model expansion of the kernel. The third order coefficients, the reference points and the remainder bound interval are shown.

CHAPTER 3

3D Laplace and Poisson solver using DA

In this chapter we describe a new method to solve the Poisson equation

$$\nabla^2 \phi\left(\vec{r}\right) = \rho\left(\vec{r}\right) \text{ in the bounded volume } \Omega \subset \mathbb{E}^3, \qquad (3.0.1)$$

$$\nabla \phi\left(\vec{r}\right) = \vec{g}\left(\vec{r}\right) \text{ on the surface } \partial\Omega.$$

In comparison to the Neumann problem where only the component of the gradient normal to the surface is specified, the boundary condition specified in the equation (3.0.1) requires the full gradient to be specified on the surface. However, as we will see later that the numerical scheme we develop requires all components of the gradient to be specified on the boundary. In practice this poses no problem as we often measure or have information about the complete field rather than just the normal component.

In the equation (3.0.1) the source density $\rho\left(\vec{r}\right)$ and the normal component of the gradient $\vec{g}\left(\vec{r}\right)$ are related by

$$\int_\Omega \rho\left(\vec{r}\right) d^3x = \int_{\partial\Omega} \hat{n} \cdot \vec{g}\left(\vec{r}\right) d^2x, \qquad (3.0.2)$$

where $\hat{n}$ is the unit vector perpendicular to the surface $\partial\Omega$ at $\vec{r}$. The equation (3.0.2) states that the net field across the surface of the volume Ω is equal to the total

amount of field created at the sources inside the volume Ω, and this follows directly from application of the divergence theorem to the equation (3.0.1). The potential $\phi_1(\vec{r})$ due to the source density $\rho(\vec{r})$ in vacuum is given by

$$\phi_1(\vec{r}) = \frac{1}{4\pi\epsilon_0} \int_\Omega \frac{\rho(\vec{r})}{|\vec{r}|} d^3x.$$

The potential $\phi_1(\vec{r})$ satisfies the Poisson equation

$$\nabla^2 \phi_1(\vec{r}) = \rho(\vec{r}) \text{ in the bounded volume } \Omega \subset \mathbb{E}^3. \tag{3.0.3}$$

Now, subtracting the equation (3.0.3) from (3.0.1), we get

$$\nabla^2 (\phi(\vec{r}) - \phi_1(\vec{r})) = 0 \text{ in the bounded volume } \Omega \subset \mathbb{E}^3,$$

$$\nabla(\phi(\vec{r}) - \phi_1(\vec{r})) = \vec{g}(\vec{r}) - \nabla\phi_1(\vec{r}) \text{ on the surface } \partial\Omega.$$

Let a new potential $\psi(\vec{r})$ and a vector field $\vec{f}(\vec{r})$ be defined by

$$\psi(\vec{r}) = \phi(\vec{r}) - \phi_1(\vec{r}),$$

$$\vec{f}(\vec{r}) = \vec{g}(\vec{r}) - \nabla\phi_1(\vec{r}).$$

The potential $\psi(\vec{r})$ is then the solution to the Laplace equation

$$\nabla^2 \psi(\vec{r}) = 0 \text{ in the bounded volume } \Omega \subset \mathbb{E}^3, \tag{3.0.4}$$

$$\nabla\psi(\vec{r}) = \vec{f}(\vec{r}) \text{ on the surface } \partial\Omega.$$

We have succeeded in splitting our original problem of solving the Poisson equation (3.0.1) into two independent problems, the solutions of which can then be combined to get the final solution. In the first problem we find the scalar potential $\psi(\vec{r})$ that satisfies the Laplace equation inside the volume Ω enclosed by surface $\partial\Omega$, when the gradient of the potential, $\nabla\psi(\vec{r}) = \vec{f}(\vec{r})$ is specified on the surface $\partial\Omega$. In the second problem we compute the potential $\phi_1(\vec{r})$ due to the source distribution $\rho(\vec{r})$ in vacuum. Both these elements can then be combined to get the solution to the Poisson equation.

41

In the section 3.1.1 we first discuss the benefits of using the boundary data and present the analytic closed form solution for the 2D case that can be easily found by application of Cauchy's integral formula. We then use a 2D example to highlight the advantages of the methods that use the boundary data to compute the solution. In section 3.1.3 we present the theory and the implementation of the new scheme to find the solution of the 3D Laplace equation when the gradient of the solution is specified on the surface enclosing the volume of interest . This scheme is based on the Helmholtz theorem and the tools of the code COSY INFINITY [17, 23, 24]. In the section 3.1.3 we present an application of this new scheme to a theoretical bar magnet problem. We also extend the theory to find the verified solutions of the Laplace equation 3.2. The implementation and the results of the application to the analytic bar magnet problem are discussed. The rest of this chapter describes a new DA based technique to compute the magnetic field due to an arbitrary source distribution.

3.1 The Laplace solver

The 3D Laplace equation

$$\nabla^2 \psi\left(\vec{r}\right) = 0 \text{ in the bounded volume } \Omega \subset \mathbb{E}^3 \tag{3.1.1}$$

is one of the important PDEs of physics, describing among others the phenomenology of electrostatics and magnetostatics. In many typical applications, not only the normal derivative of ψ but indeed the entire gradient $\vec{\nabla}\psi$ is known on the surface; for example, in the magnetostatic case the entire field $\vec{B} = \vec{\nabla}\psi$ is measured, and not merely the component normal to the surface under consideration. Thus the field computation problem can be viewed as solving a boundary value problem for the three dimensional $(3D)$ Laplace equation for the field, i.e. to obtain the solution of

the PDE

$$\nabla^2 \psi \left(\vec{r} \right) = 0 \text{ in the volume } \Omega \subset \mathbb{E}^3$$

where $\nabla \psi \left(\vec{r} \right) = \vec{f} \left(\vec{r} \right)$ is specified on the surface $\partial \Omega$.

As discussed in the chapter 2 the existence and uniqueness of the solution for the 3D Laplace equation case can easily be shown through the application of Green's formulae or by using mean-value formulas. But, the analytic closed form solutions for the 3D Laplace equation case can usually only be found for special problems with certain regular geometries where a separation of variables can be performed. However, in most practical 3D cases, numerical methods are the only way to proceed. Frequently the finite difference or finite element approaches are used to find the approximations of the solution on a set of points in the region of interest. But because of their relatively low approximation order, for the problem of precise solution of PDEs, the methods have very limited success because of the prohibitively large number of mesh points required. Furthermore, direct validation of such methods is often very difficult.

3.1.1 Methods using boundary data

Boundary data methods such as those utilized below are based on a description of the interior field in terms of particular surface integrals involving the surface data. These approaches have various advantages. Firstly, the solution is analytic in terms of the interior variables, even if the boundary data fail to be differentiable or are even piecewise discontinuous; all such non-smoothness is removed after the integration is executed. Hence a Taylor polynomial approximation in terms of interior variables can be performed; and we expect that a Taylor approximation of a certain order will provide an accurate approximation over suitable domains.

Secondly, since for the PDEs under consideration here the solution functions are known to assume their extrema on the boundary because of analyticity or harmonic-

43

ity, a method that uses boundary data is expected to be robust against errors in those boundary data with errors in the interior not exceeding the errors on the surface. Thirdly, if the boundary data given have statistical errors, such errors have a tendency to even average out in the integration process as long as the contributions of individual pieces of integration are of similar significance. Thus we expect the error in the computed field in the interior to be generally much smaller than the error in the boundary data. This ensures that the methods using boundary data are computationally stable .

3.1.2 The two dimensional case

As an introduction to the general approach, we begin with the discussion of the 2D case, the theory of which can be fully developed in the framework of elementary complex analysis, and which also describes the situation of static electric or magnetic fields as long as no longitudinal field dependence is present. It is based on the use of Cauchy's integral formula stating that if the function f is analytic in a region containing the closed path C, and if α is a point within C, then

$$f(\alpha) = \frac{1}{2\pi i} \oint_C \frac{f(z)}{z - \alpha} dz \qquad (3.1.2)$$

where the integral denotes the path integral over C. Cauchy's formula is an integral representation of f which permits us to compute f anywhere in the interior of C, knowing only the value of f on C. This integral representation of f is also the solution of the 2D Laplace equation for the primitive of $(\text{Re}(f), -\text{Im}(f))$ with the function f specified on the path C.

Now, suppose a random error of $\delta(z)$ is introduced in the measured data around the path C. Then by the equation (3.1.2) we can compute the error $E(a)$ introduced in the computation of $f(\alpha)$ at some point α inside C as

$$E(\alpha) = \frac{1}{2\pi i} \oint_C \frac{f(z) + \delta(z)}{z - \alpha} dz - f(\alpha) = \frac{1}{2\pi i} \oint_C \frac{\delta(z)}{z - \alpha} dz \qquad (3.1.3)$$

44

We note that while $E(\alpha)$ is given by a Cauchy integral, E need not be analytic since $\delta(z)$ need not assume the function values of an analytic function. In fact, if it would, then it already would be uniquely specified on any dense subset S of C, which removes the freedom for all values of E on points on C that are not in S.

While the error E itself may be bounded in magnitude, if the integral is approximated by one of the conventional numerical quadrature methods, the result can become singular as the point α approaches the boundary C. This case may limit the practical use of the method and needs to be studied carefully. As an example, we consider the case of quadrature based on adding the terms of a Riemann sum, i.e. the approximation

$$\frac{1}{2\pi i}\oint_C \frac{\delta(z)}{z-\alpha}dz \approx \frac{1}{2\pi i}\cdot\sum_{j=1}^{N_z}\frac{\delta\left(z_j\right)}{\left(z_j-\alpha(r)\right)}\cdot\left(z_j-z_{j-1}\right)=\tilde{E}(\alpha) \qquad (3.1.4)$$

where the N_z points z_j are spaced equidistantly around C; since C is closed, $z_0 = z_{N_z}$. By studying the approximation $\tilde{E}(a)$ as the point α approaches the boundary C, we can analyze the stability of the method with respect to the discretization of the path C.

As an example, we choose the path C as a circle of radius R enclosing the region of interest. We assume a random error of $\delta(z)\left(\pm 10^{-2}\right)$ is introduced in the measured data around C. The point α is given by $r\cdot\exp(i\cdot\phi)$ and the points z_j are given by $R\cdot\exp(i\cdot 2\pi j/N_z)$ for $j=0,\ldots,N_z$. Letting $\delta_m(z_j)$ denote the error assigned to point z_j in error set m, for each of these error sets we express the Riemann sum $\zeta_m(\alpha)$ for point α by

$$\zeta_m(\alpha)=\frac{1}{2\pi i}\cdot\sum_{j=1}^{N_z}\frac{iz_j\delta_m\left(z_j\right)}{\left(z_j-\alpha(r)\right)}\cdot\frac{2\pi}{N_z}$$

We then form the average of the magnitude of the error over N_e error sets to obtain

$$\eta(r)=\frac{1}{N_e}\sum_{m=1}^{N_e}\left|\zeta_m(\alpha)\right|.$$

45

Note that $\eta(r)$ still depends on the phase ϕ. However, in the statistical limit there is apparently invariance under rotation by $\exp\left(i \cdot 2\pi/N_z\right)$; and one quickly sees that there are two limiting cases for the choice of the phase. These are the case $\phi = 0$, where the α will eventually collide with the z_j for $j = N_z$ as $r \to R$ and thus a "worst case" divergence will appear, and the case $\phi = 2\pi/2N_z$, in which case the α will approach the mid point between z_j for $j = N_z$ and z_j for $j = 1$ as $r \to R$. Choosing sufficiently fine discretization of the path and sufficiently many error sets δ_m, the quantity $\eta(r)$ for these two cases will be a good measure for the accuracy that can be achieved with the surface integral method.

For our specific example, we choose random errors of maximum magnitude 10^{-2} at $N_z = 10,000$ points on the circle of radius $R = 2$. For each value of r, we perform the computation for a total of $N_e = 10,000$ error sets. The results of this analysis are shown as plots in Figure 3.1.1a and Figure 3.1.1b for the two cases that represent the "worst case" and the "best case" situation.

We first observe that sufficiently away from the surface, the expected smoothing effect is happening, and the errors in the function values are indeed well below the errors assumed on the surface. A rough quantitative analysis shows that this error is about two orders of magnitude below the surface data error, corresponding well with the statistically expected decrease of the error by $1/\sqrt{N_z}$. As α approaches the curve closer than 10^{-3}, in the "best case" situation, the error rises to about 10^{-2}, which is because now only nearby grid points contribute to the sum and thus the smoothing effect disappears. In the "worst case" scenario, divergence actually happens; but the average error is still at the level of the original random error of 10^{-2} for values of r that are only about 10^{-4} away from the radius 2.

So overall we see that the method performs significant smoothing, and even with the simplest discretization as a Riemann sum, good accuracy is maintained even as we approach C. We note in passing that with more sophisticated quadrature meth-
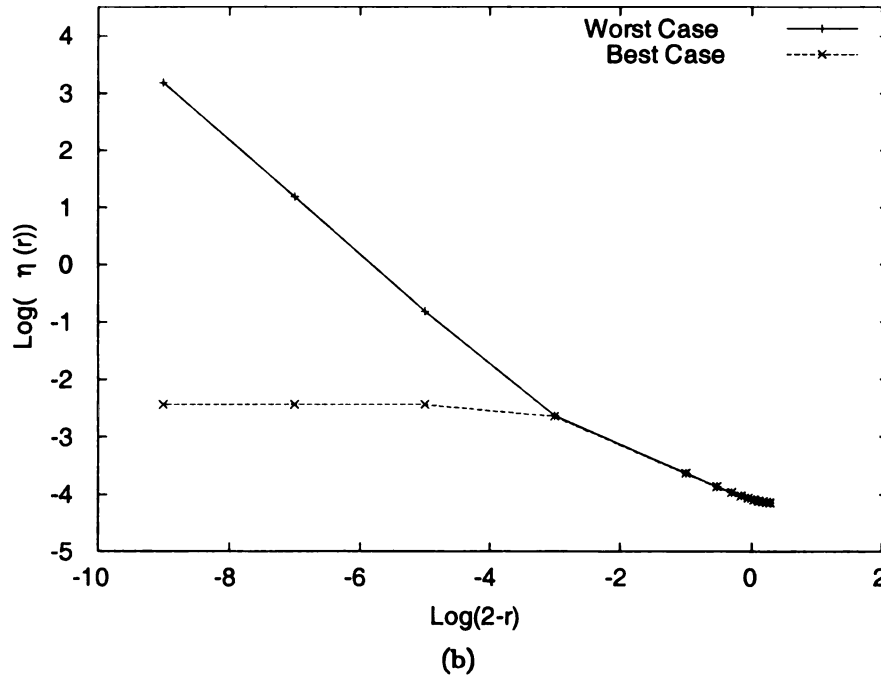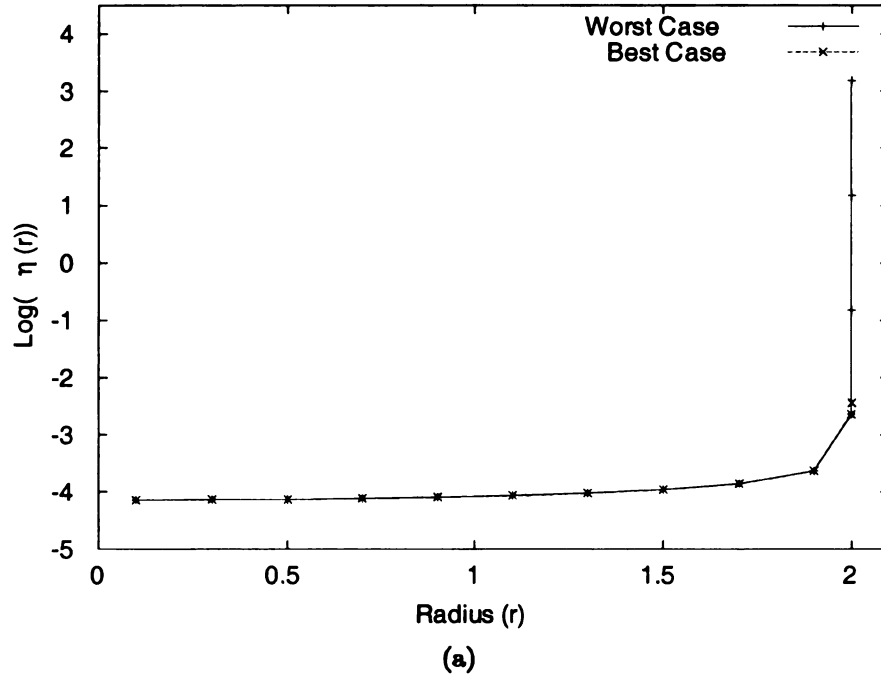
Figure 3.1.1. (a) The plot shows the dependency of $\eta(r)$ on the radius r. (b) The plot shows the dependency of $\eta(r)$ on the radius as the radius r approaches the boundary. 10,000 error sets (N_e) around the circle or radius $R = 2$ were chosen for the analysis. We show the plots for both the best and the worst case scenario.

47

ods, for example those based on Gaussian methods [17], the divergence effect can be significantly controlled.

3.1.3 The three dimensional case

The scheme we use for the 3D case is based on the Helmholtz vector decomposition theorem discussed in the sections 2.1.1 and 2.1.2. We begin by representing the solution of the PDE via the Helmholtz theorem, which states that any vector field $\overrightarrow{B}$ which vanishes at infinity can be written as the sum of two terms

$$\overrightarrow{B}(\vec{x}) = \vec{\nabla} \times \vec{A}_t(\vec{x}) + \vec{\nabla}\phi_n(\vec{x}), \text{ where} \tag{3.1.5}$$

$$\phi_n(\vec{x}) = \frac{1}{4\pi} \int_{\partial\Omega} \frac{\vec{n}(\vec{x}_s) \cdot \overrightarrow{B}(\vec{x}_s)}{|\vec{x} - \vec{x}_s|} ds - \frac{1}{4\pi} \int_{\Omega} \frac{\vec{\nabla} \cdot \overrightarrow{B}(\vec{x}_v)}{|\vec{x} - \vec{x}_v|} dV, \text{ and}$$

$$\vec{A}_t(\vec{x}) = -\frac{1}{4\pi} \int_{\partial\Omega} \frac{\vec{n}(\vec{x}_s) \times \overrightarrow{B}(\vec{x}_s)}{|\vec{x} - \vec{x}_s|} ds + \frac{1}{4\pi} \int_{\Omega} \frac{\vec{\nabla} \times \overrightarrow{B}(\vec{x}_v)}{|\vec{x} - \vec{x}_v|} dV.$$

Here $\partial\Omega$ is the surface which bounds the volume Ω. $\vec{x}_s$ denotes a point on the surface $\partial\Omega$, and $\vec{x}_v$ denotes a point within Ω. $\vec{n}$ is the unit vector perpendicular to $\partial\Omega$ that points away from Ω. $\vec{\nabla}$ denotes the gradient with respect to $\vec{x}_v$.

The first term is usually referred to as the solenoidal term, and the second term as the irrotational term. Because of the apparent similarity of these two terms to the well-known vector- and scalar potentials to $\vec{B}$, we note that in the above representation, it is in general not possible to utilize only one of them; for a given problem, in general both ϕ_n and $\vec{A}_t$ will be nonzero.

For the special case that $\vec{B} = \vec{\nabla}V$, we have $\vec{\nabla} \times \vec{B} = 0$; furthermore, if V is a solution of the Laplace equation $\vec{\nabla}^2 V = 0$, we have $\vec{\nabla} \cdot \overrightarrow{B} = 0$. Thus in this case, all the volume integral terms vanish, and $\phi_n(\vec{x})$ and $\vec{A}_t(\vec{x})$ are completely determined from the normal and the tangential components of $\vec{B}$ on the surface $\partial\Omega$ via

$$\phi_n(\vec{x}) = \frac{1}{4\pi} \int_{\partial\Omega} \frac{\vec{n}(\vec{x}_s) \cdot \overrightarrow{B}(\vec{x}_s)}{|\vec{x} - \vec{x}_s|} ds \tag{3.1.6}$$

$$\vec{A}_t(\vec{x}) = -\frac{1}{4\pi} \int_{\partial\Omega} \frac{\vec{n}(\vec{x}_s) \times \overrightarrow{B}(\vec{x}_s)}{|\vec{x} - \vec{x}_s|} ds. \tag{3.1.7}$$

For static electric or magnetic fields without sources in Ω, which are characterized by the Laplace problem that we are studying, the divergence and the curl of the field vanish and hence these fields can be decomposed into irrotational and solenoidal parts. For any point within the volume Ω, the scalar and vector potentials depend only on the field on the surface $\partial\Omega$. And due to the smoothing properties of the integral kernel, the interior fields will be analytic even if the field on the surface data fails to be differentiable.

Surface integration and finite elements via DA

Since the expressions (3.1.6) and (3.1.7) are analytic, they can be expanded at least locally. The idea is now to expand them to higher orders in BOTH the two components of the surface variables $\vec{x}_s$ and the three components of the volume variables $\vec{x}$. The polynomial dependence on the surface variables will be integrated over surface subcells, which results in a highly accurate integration formula with an error order equal to that of the expansion. The dependence on the volume variables will be retained, which leads to a high order finite element method. By using sufficiently high order, high accuracy can be achieved with a small number of surface elements, and more importantly, a small number of volume elements. We describe the details of the implementation in the following.

The volume Ω is subdivided into volume elements. Using the prescription for the surface field, the Taylor expansion of the field is computed at the center of each volume element. The final solution inside the overall volume is given as local expansions of the field in different volume elements.

To find the local expansions for each volume element, we first split the domain of integration $\partial\Omega$ into smaller elements Γ_i. From the surface field formula we extract an approximate Taylor expansion in the surface variables $\vec{x}_s$ about the center of the surface element. Then the integral kernel $1/\left|\vec{r} - \vec{r}_s\right|$ and the field $\vec{B}$ on the surface

are Taylor expanded in the surface variables $\vec{r}_s$ about the center of each surface element. We also Taylor expand the kernel in the volume variables $\vec{r}$ about the center of the volume element. The final step is to integrate and sum the resulting Taylor expansions for all surface elements. Depending on the accuracy of the computation needed we choose step sizes, order of expansion in $r\,(x, y, z)$, and order of expansion in $r_s\,(x, y, z)$.

All the mathematical operations to perform the expansion, surface integration, curl and divergence were implemented using the high-order multivariate differential algebraic tools available in the code COSY INFINITY [23, 24, 17] which automatically leads to the respective field representation to any order without any manual computations.

An analytical example: the bar magnet

As a reference problem we consider the magnetic field of an arrangement of the two rectangular iron bars with inner surfaces ($y = \pm y_0$) parallel to the midplane ($y = 0\,m$) as shown in Figure 3.1.2a. The interior of these uniformly magnetized bars, which are assumed to be infinitely extended in the $\pm y$-directions, is defined by: $x_1 \leq x \leq x_2$, $|y| \leq y_0$, and $z_1 \leq z \leq z_2$. From this bar magnet one can obtain an analytic solution for the magnetic field $\vec{B}\,(x, y, z)$ - see for example [31] - and the result is given by

$$B_y\,(x, y, z) = \frac{B_0}{4\pi} \sum_{i,j=1}^{2} (-1)^{i+j} \left[\arctan\left(\frac{X_i \cdot Z_j}{Y_+ \cdot R_{ij}^+} \right) + \arctan\left(\frac{X_i \cdot Z_j}{Y_- \cdot R_{ij}^-} \right) \right]$$

$$B_x\,(x, y, z) = \frac{B_0}{4\pi} \sum_{i,j=1}^{2} (-1)^{i+j} \left[\ln\left(\frac{Z_j + R_{ij}^-}{Z_j + R_{ij}^+} \right) \right]$$

$$B_z\,(x, y, z) = \frac{B_0}{4\pi} \sum_{i,j=1}^{2} (-1)^{i+j} \left[\ln\left(\frac{X_j + R_{ij}^-}{X_j + R_{ij}^+} \right) \right]$$

where $X_i = x - x_i$, $Y_\pm = y_0 \pm y$, $Z_i = z - z_i$, and $R_{ij}^\pm = \left(X_i^2 + Y_j^2 + Z_\pm^2 \right)^{\frac{1}{2}}$. We note that because of the symmetry of the field around the midplane, only even order

(a)   (b)
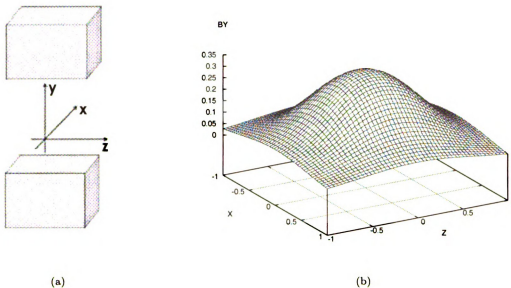
Figure 3.1.2. (a) The geometric layout of the bar magnet, consisting of two bars of magnetized material. (b) The magnetic field B_y on the center plane of the bar magnet. $B_0 = 1T$ and the interior of this magnet is defined by $-0.5 \leq x \leq 0.5$, $|y| \leq 0.5$, and $-0.5 \leq z \leq 0.5$.

terms exist in the Taylor expansion of this field about the origin. The mid plane field of such a magnet is shown in Figure 3.1.2b.

The method presented in the section 3.1.3 is valid for any volume enclosed by a smooth surface. For this example we choose three cases, (a) a volume enclosed by a cube, (b) a volume enclosed by a cylinder, and (c) a volume enclosed by a sphere. For these cases we first study the performance of the surface integration method. To this end, we consider a cube of edge length $0.8 \ m$, a cylinder of length $0.8 \ m$ and radius $0.4 \ m$, and a sphere of radius $0.4 \ m$. The center of all three geometries coincides with the center of the interior of the uniformly magnetized bars. The six surfaces of the cube are each subdivided into a 44×44 mesh. The surface of the cylinder and the sphere are also subdivided so that the number of cells are same as in the cube case. On each of the mesh cells, the contribution from the Helmholtz integral is expanded using differential algebraic tools [17], and the resulting polynomial is integrated.

Figure 3.1.3 shows the accuracy of the predicted field, compared with the exact solution, as a function of the order of expansion within the surface mesh cells. Results are shown for the points $(0,0,0)$, $(0.1,0.1,0.1)$, $(0.2,0.2,0.2)$ and $(0.3,0.3,0.3)$ for the cube case. It can be seen that at order six, an accuracy of approximately 10^{-12} is reached, which is very high compared to conventional numerical field solvers. The corresponding results for the cylinder and sphere case are shown in figures 3.1.4 and 3.1.5.
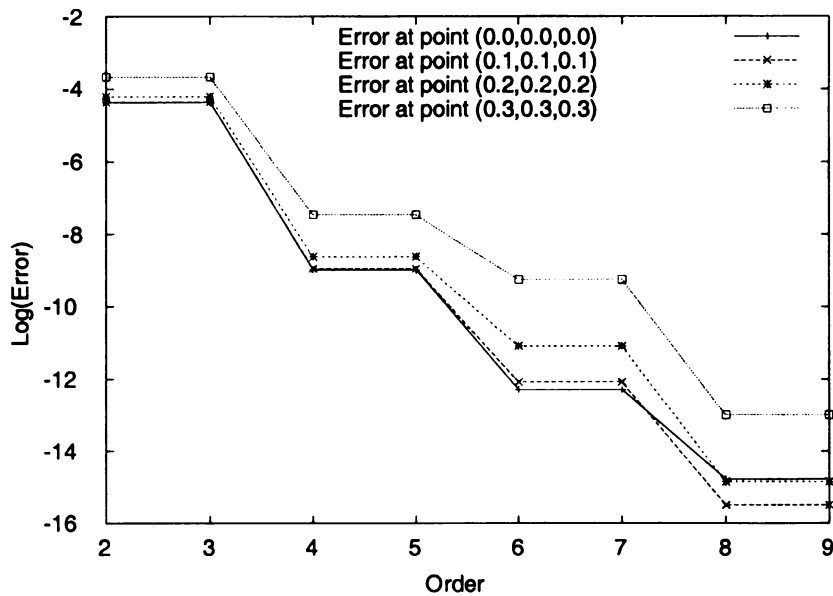
Figure 3.1.3. The error for the field calculated for the bar magnet example with rectangular grid for individual points $(0,0,0)$, $(0.1,0.1,0.1)$ and $(0.2,0.2,0.2)$ $(0.3,0.3,0.3)$.

We note that a change from an even order to the next higher order does not produce significant change in the error, which is due to the specific symmetry of the magnetic field and the resulting fact that even orders dominate in the Taylor expansion. Also, this study clearly demonstrates that the method works for all smooth surfaces. Henceforth we only present the results for the cube case.

For the next example, we split the volume inside the bar magnet into $4 \times 4 \times 4$ finite
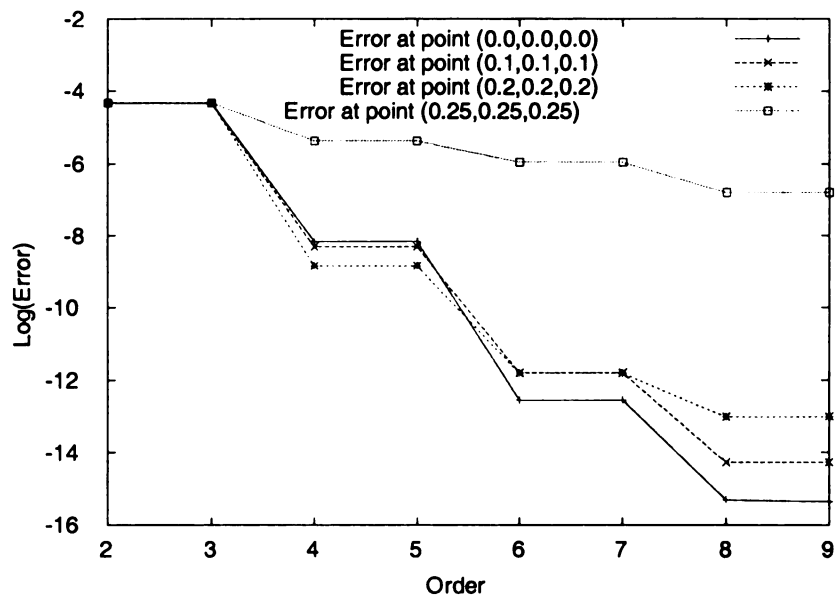
Figure 3.1.4. The error for the field calculated for the bar magnet example with cylinderical grid for individual points $(0,0,0)$, $(0.1,0.1,0.1)$ and $(0.2,0.2,0.2)$ $(0.25,0.25,0.25)$.
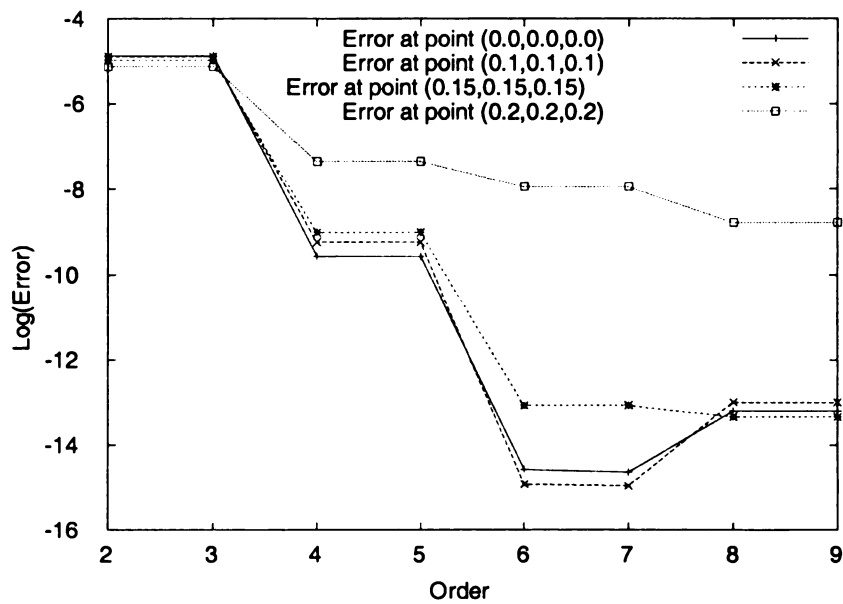
Figure 3.1.5. The error for the field calculated for the bar magnet example with speherical grid for individual points $(0,0,0)$, $(0.1,0.1,0.1)$ and $(0.15,0.15,0.15)$ $(0.2,0.2,0.2)$.
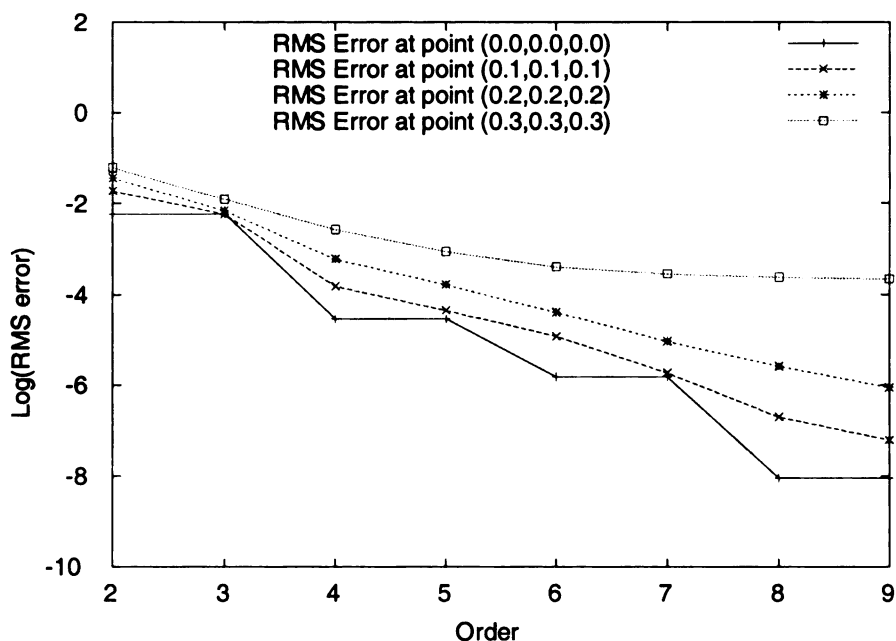
Figure 3.1.6. The average error for the field calculated for the bar magnet example for finite elements of width 0.4 around points $(0,0,0)$ and $(0.1,0.1,0.1)$.

elements of width ± 0.1 m. Within each of the elements, a Taylor expansion in the three volume variables is carried out, resulting in a polynomial representation of the field within the finite element cell. The polynomial representation is used to evaluate the field at 1000 randomly chosen points within the cell, and comparing the result with the analytical answer. Figure 3.1.6 shows the resulting RMS error for finite elements centered around $(0,0,0)$, $(0.1,0.1,0.1)$, $(0.2,0.2,0.2)$ and $(0.3,0.3,0.3)$. The plot for the finite element centered at $(0.3,0.3,0.3)$ shows the behavior of the RMS error as we approach the boundary. It can be seen that the method remains stable as we approach the boundary. For the finite elements well within the volume of interest, it can be seen that at order 7, an accuracy of approximately 10^{-6} is reached.

We see that the method of simultaneous surface and volume expansion, all of which can be carried out fully automatically using differential algebraic tools [17] implemented in the code COSY [23, 24], leads to accuracies that are significantly higher

55

than those of conventional finite element tools, even when unusually large finite elements are used.

For purposes of illustration, we now show in the table 3.1.1 the Taylor expansion of the field given by the equation (3.1.6) and calculated using the DA tools of COSY over one surface element for a particular point frozen inside the volume of interest. The center of the surface element is at $(-0.39, -0.39, 0.4)$ and the point is at $(0.1, 0.1, 0.1)$. The surface element is described by $\left(-0.39 + 0.5\lambda_x x_s, -0.39 + 0.5\lambda_y y_s, 0.4\right)$, where λ_x, λ_y represent the length and width of the surface element and $x_s, y_s \in [-1, 1]$. In

```
I   COEFFICIENT            ORDER EXPONENTS
1   0.1430015055365947E-01  0    0 0   0 0   0
2   0.6922600731781813E-03  1    0 0   0 1   0
3   -.9437452710153340E-03  1    0 0   0 0   1
4   -.1561210105220474E-04  2    0 0   0 2   0
5   -.4471499751575185E-04  2    0 0   0 1   1

                        ⋮

20  -.3232493054085583E-07  5    0 0   0 1   4
21  0.6156849473575023E-07  5    0 0   0 0   5
22  0.8960505971632865E-10  6    0 0   0 6   0
23  0.1890553337467643E-08  6    0 0   0 5   1
24  -.9792219471281489E-09  6    0 0   0 4   2

                        ⋮

41  -.2417698920592542E-10  8    0 0   0 4   4
42  0.7717865536738434E-10  8    0 0   0 3   5
43  -.2649803372019223E-11  8    0 0   0 2   6
44  -.2561415687161454E-10  8    0 0   0 1   7
45  0.8506329051477273E-10  8    0 0   0 0   8
---------------------------------------------
```

Table 3.1.1. A sample eighth order Taylor expansion in two surface variables.

the representation of the Taylor expansion in x_s and y_s in the table 3.1.1, the entries in the first column provide the number assigned to each of the coefficients in the Taylor expansion to easily identify them. The entries in the second column provide

the numerical value of the coefficients. The entries in the fourth, fifth and the sixth columns provide the expansion orders with respect to the volume variables(x, y, z). And the entries in the seventh and eighth column provide the expansion orders with respect to the surface variables (x_s, y_s). The total order for each coefficient is the sum of all the orders in columns four through eight, which is given in the third column. Since we compute the Taylor expansion about a particular point $(0.1, 0.1, 0.1)$ frozen in the volume of interest in two surface variables (x_s, y_s), we notice that the entries in column four, five, six are all zero. It can be seen that in this expansion, the contributions of higher order terms depending on the surface variables decrease rapidly, and thus the expansion shown would lead to a result of very high accuracy.

We now present the Taylor expansion of the contribution of the equation (3.1.6) for one surface element and over one volume element inside the volume of interest in the table 3.1.2. The center of the surface element is at $(-0.39, -0.39, 0.4)$ and the center of the volume element is at $(0.1, 0.1, 0.1)$. The surface element and the volume element can be fully described by $\left(-0.39 + 0.5\lambda_x x_s, -0.39 + 0.5\lambda_y y_s, 0.4\right)$ and $\left(0.1 + 0.5\rho_x x, 0.1 + 0.5\rho_y y, 0.1 + 0.5\rho_z z\right)$, respectively, where λ_x, λ_y represent the length and width of the surface element, and ρ_x, ρ_y, ρ_z represent the length, width and height of the volume element, and $x_s, y_s, x, y, z \in [-1, 1]$. In this case the coefficients of the Taylor expansion depend on both the surface (x_s, y_s) and the volume variables (x, y, z). The coefficients depending only on the surface variables and the coefficient of the zeroth order term are same as in the previous example of the expansion in just the surface variables. Once again we notice that the contributions of higher order terms decrease rapidly for higher order, showing that also the expansion in volume variables leads to a very accurate representation.

We now study the error dependency on the size(length) of the volume element, or equivalently the number of volume elements chosen for the computation. For the order of computation 3,5,7 and 9, Figure 3.1.7 and Figure 3.1.8 provide the dependence of

```
I    COEFFICIENT               ORDER  EXPONENTS
1    0.1430015055365947E-01    0      0 0   0 0   0
2    -.9590481459719686E-02    1      1 0   0 0   0
3    -.9590481459719686E-02    1      0 1   0 0   0
4    -.9768082968233012E-02    1      0 0   1 0   0
5    0.6922600731781813E-03    1      0 0   0 1   0
6    -.9437452710153340E-03    1      0 0   0 0   1

                                       ⋮

454  -.4509222359486833E-07    6      0 1   0 0   5
455  -.3067430813781439E-07    6      0 0   1 0   5
456  0.8960505971632865E-10    6      0 0   0 6   0
457  0.1890553337467643E-08    6      0 0   0 5   1
458  -.9792219471281489E-09    6      0 0   0 4   2

                                       ⋮

1283 -.2417698920592547E-10    8      0 0   0 4   4
1284 0.7717865536738462E-10    8      0 0   0 3   5
1285 -.2649803372019148E-11    8      0 0   0 2   6
1286 -.2561415687161455E-10    8      0 0   0 1   7
1287 0.8506329051477271E-10    8      0 0   0 0   8
```

Table 3.1.2. A sample eighth order Taylor expansion in two surface variable and three volume variables.

the average error on the length of the volume element and the total number of volume elements. As an example, for cell lengths of 0.1, which leads to a total number of only 550 finite elements, an accuracy of 10^{-10} can be reached with a ninth order method. Similarly, for a seventh order method with a cell length of 0.2, corresponding to 125 boxes, accuracies of about 10^{-6} can be reached. Compared to the conventional 3D Laplace solvers which typically utilize in the order of 10^6 cells to achieve accuracies in the order of 10^{-3}, these results are quite promising.
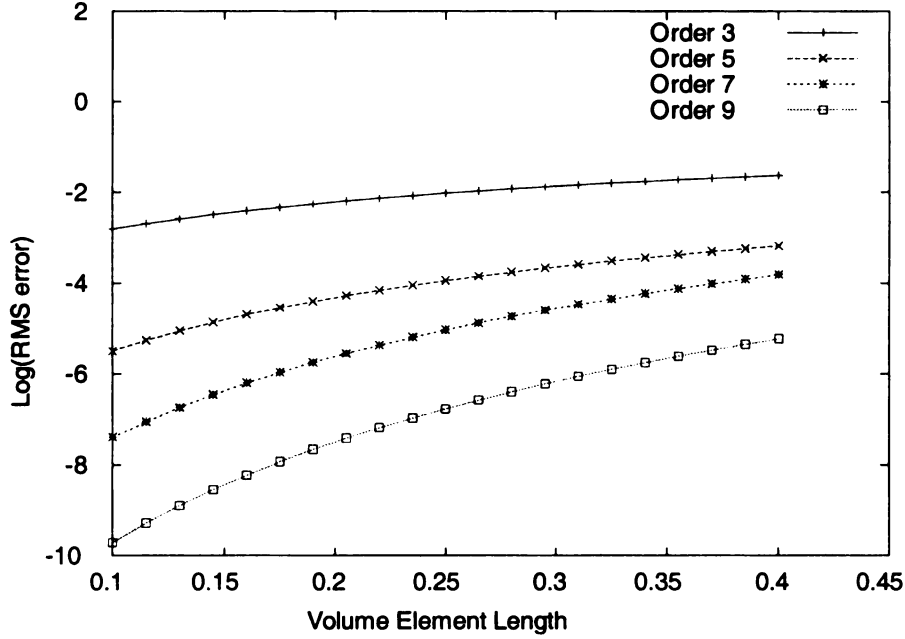
Figure 3.1.7. The plot shows the dependency of the average error on the length of the volume element.

3.2 Verified solution of the 3D Laplace equation

For various practical problems, very precise and verified solutions of this PDE are required; but with conventional finite element or finite difference codes this is difficult to achieve even without validation because of the need for an exceedingly fine mesh which leads to often prohibitive CPU time. The method presented in the section 3.1 can used to build an alternative approach based on high-order quadrature and a high-order finite element method to find a verified solution to Laplace's equation. Both of the ingredients become accessible through the use of Taylor model methods [53, 50] and the corresponding tools in the code COSY INFINITY [24, 23]. The solution in space is first represented as a Helmholtz integral over the two-dimensional surface. The latter is executed by evaluating the kernel of the integral as a Taylor model [53, 50] of both the two surface variables and the three volume variables inside

59
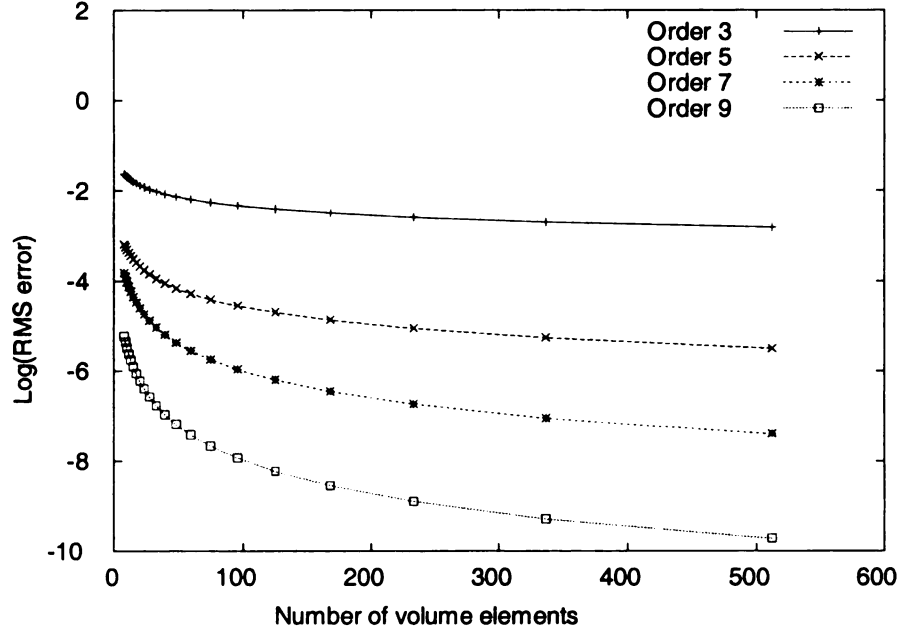
Figure 3.1.8. The plot shows the dependency of the average error on the number of volume element.

the cell of interest. Finally, the integration over the surface variables is executed as a mere polynomial integration, resulting in a local Taylor model of the solution within one cell. The final solution is provided as a set of local Taylor models, each of which represents an enclosure of a solution for a sub-box of the volume of interest. Examples of the method and the precision that can be achieved will be given.

To obtain a verified solution to Laplace's equation we start from equations 3.1.6 and 3.1.7. Using the fact that if $\vec{x} \neq \vec{x}_s$, we have $\vec{\nabla}\left(1/\left|\vec{x} - \vec{x}_s\right|\right) = -\left(\vec{x} - \vec{x}_s\right)/\left|\vec{x} - \vec{x}_s\right|^3$, and similar relationships, it is possible to explicitly obtain the gradient of the scalar potential, and with some more work the curl of the vector potential; the results have

the explicit form

$$\vec{\nabla}\phi_n\left(\vec{x}\right) = -\frac{1}{4\pi}\int_{\partial\Omega}\frac{\left(\vec{x}-\vec{x}_s\right)\left(\vec{n}\left(\vec{x}_s\right)\cdot\vec{B}\left(\vec{x}_s\right)\right)}{\left|\vec{x}-\vec{x}_s\right|^3}ds \tag{3.2.1}$$

$$\vec{\nabla}\times\vec{A}_t\left(\vec{x}\right) = \frac{1}{4\pi}\int_{\partial\Omega}\frac{\left(\vec{x}-\vec{x}_s\right)\times\left(\vec{n}\left(\vec{x}_s\right)\times\vec{B}\left(\vec{x}_s\right)\right)}{\left|\vec{x}-\vec{x}_s\right|^3}ds \tag{3.2.2}$$

From the equation (3.1.5) we know that the field inside the volume of interest is just a sum of the irrotational (equation (3.2.1)) and the solenoidal (equation (3.2.2)) part. This is then the solution for the magnetic field as surface integrals. But to numerically integrate the kernel and get the verified solution as the local Taylor model we need a specialized numerical scheme. In the next section we introduce one such scheme based on the Taylor models of the code COSY INFINITY [24, 23]. The anti-derivation operation on the Taylor models discussed in section 2.4 will be extensively used in implementation of the scheme.

Solution of the Helmholtz Problem using Taylor models

In the following, we develop a verified method based on Taylor model methods to determine sharp enclosures of the field $\vec{B}$ and the potential ψ utilizing the Helmholtz method.

Utilizing Taylor model arithmetic, the following algorithm now allows to solve the Laplace equation for the Helmholtz problem.

1. Discretize the surface $\partial\Omega$ into individual surface cells S_i with centers s_i and the volume Ω into volume cells V_j with centers v_j.

2. Pick a volume cell V_j.

3. For each surface cell S_i, evaluate the integrands in the equation (3.2.1) and (3.2.2), the so-called "kernels", in Taylor model arithmetic to obtain a Taylor model representations in BOTH the surface variables of S_i AND the volume variables of V_j, i.e. in a total of five variables.

4. Use the Taylor model anti-derivation operation twice to perform integration over the surface variables of each cell S_i.

5. Add up all results to obtain a three dimensional Taylor model enclosing the field $\vec{B}$ over the volume cell V_j.

6. If a verified enclosure of the potential ψ to $\vec{B}$ over the volume cell V_j is desired, integrate the field $\vec{B}$ over any path using the anti-derivation operation.

As a result, for each of the volume cells V_j, Taylor model enclosures for the fields $\vec{B}$ and potentials ψ are obtained. All the mathematical operations to evaluate these Taylor Models and surface integration are implemented using the Taylor Model tools available in the code COSY INFINITY [24, 23].

Apparently the computational expense scales with the product of the number of volume elements and the number of surface elements; of these, the number of volume elements is more significant because of their larger number. In practice one observes that when using high-order Taylor models, a rather small number of volume elements is required, in particular compared to the situation in conventional field solvers.

3.2.1 An analytical example: the bar magnet

Once again, we consider the bar magnet example described in the section 3.1.3. Now we compute the validate solution to Laplace's equation with the boundary conditions described in this example.

Results and analysis As a first step in the analysis of the influence of the discretization of the surface and volume on the result, we study the contributions of the surface elements towards the remainder interval part of the total integral. The volume expansion point is chosen as $\vec{r} = (.1, .1, .1)$, and the size of the volume box around it is chosen zero. Thus after the surface integration, the polynomial part of

the dependence on volume vanishes except for the constant term, and the accuracy is only limited by the width of the surface element, which after integration over the surface variables influences the width of the remainder bound. We plot the width of the remainder interval versus surface element length for the scalar potential in Figure 3.2.1. The center of the surface element is chosen as $\vec{r}_s = (.034, .011, .5)$. It is observed that for high orders, the method quickly reaches an accuracy of around 10^{-16} for about 2^5 surface subdivisions, which correspond to about $2^{10} \approx 1000$ surface element cells per surface. Under the assumption that each of these surface cells brings a similar contribution, the accuracy due to the surface discretization will be in the range of approximately $6 \cdot 1000 \cdot 10^{-16} < 10^{-12}$.
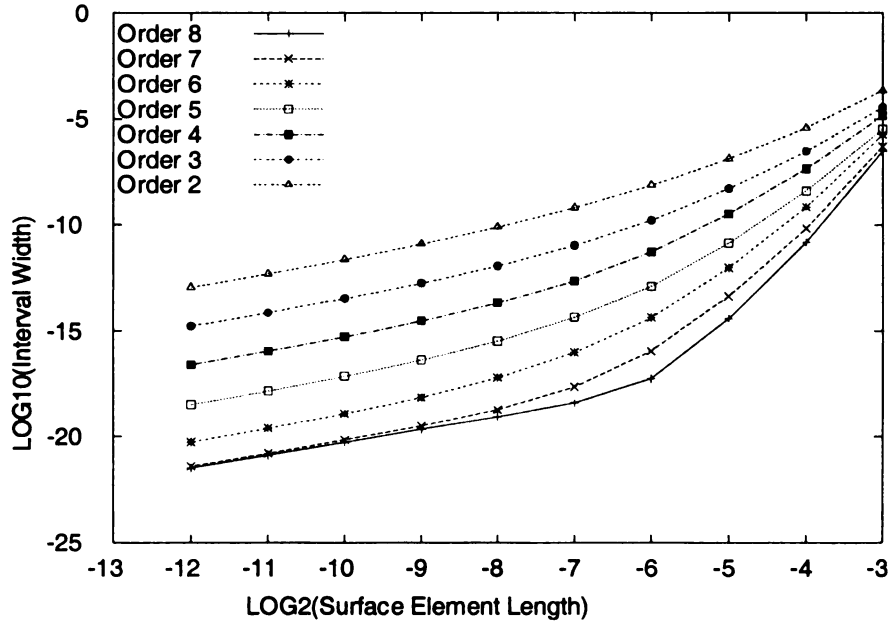
Figure 3.2.1. The remainder interval width versus the surface element length for integration over a single surface element and vanishing volume size.

We now study the dependency of the polynomial part and width of the remainder interval of the magnetic field on the volume element length. In all these plots the surface element length is kept fixed at $1/128$. Figure 3.2.2 shows the remainder

interval width for the y component of the magnetic field versus volume element lengths for different orders of computation. The other components of the magnetic field exhibit a similar behavior.
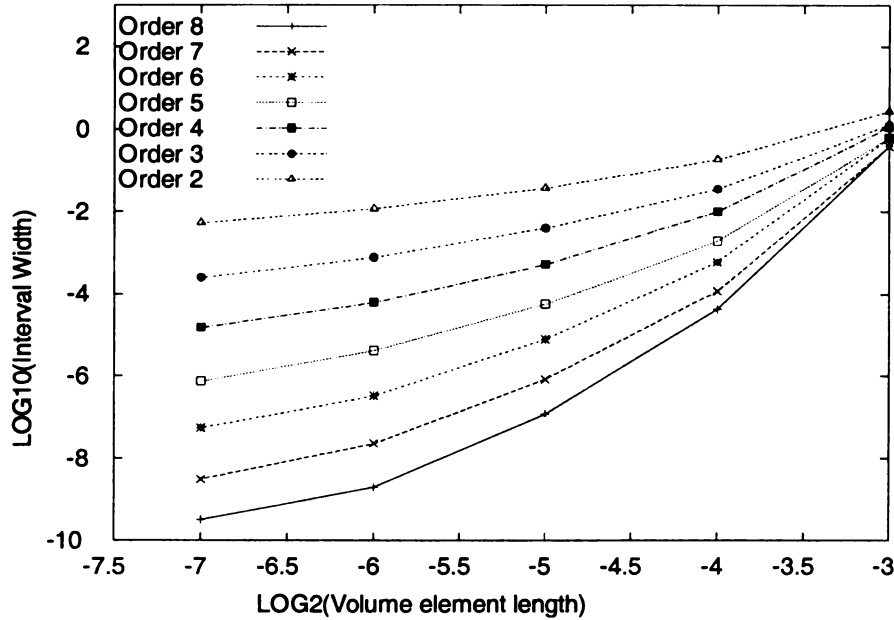
Figure 3.2.2. The remainder interval width versus the length of volume element for y component of the magnetic field.

We see that a verified accuracy in the range of 10^{-4} can be achieved for a volume element width of around 10^{-1}, corresponding to a total of around 1000 volume elements. This number compares very favorably to the above-mentioned numbers for the commercial code TOSCA [3, 4]. An accuracy in the range of 10^{-7} can be achieved for a width of around $10^{-1.4}$, corresponding to a total of around $200,000$ volume elements.

Overall, we see that the method of simultaneous surface and volume expansion of the Helmholtz integrals leads to verified tools for the solutions of PDEs which when executed in the Taylor model arithmetic can lead to very sharp enclosures. It is obvious that the method can be generalized to other surface-integral based approaches

to the solution of PDEs.

3.3   Parallel implementation of the Laplace solver

Recently the code COSY INFINITY has been ported to support large scale computations for beam dynamics simulation and design optimization, including verified global optimization. Test results with some of the COSY tools adapted to parallel execution have shown that they scale linearly to about 1000 processors [46]. Along this line of high performance computing efforts with COSY INFINITY, a parallel implementation of the Laplace solver has been practiced on the NERSC (National Energy Research Scientific Computing Center) IBM RS6000 Seaborg Cluster consisting of 6080 processors [2].

In our implementation of the Laplace solver, we first discretize the surface enclosing the volume of interest into surface elements, and then the magnetic field contribution of each surface element at a given observation point or volume is computed independently. We then sum up the magnetic field contributions of all the surface elements to obtain the magnetic field at the observation point or volume. The large summation over all the surface elements can be trivially parallelized. However, if trivially parallelized, the large summation over all the surface elements at the end may take significant time and render the algorithm inefficient. Also, to utilize the computational resources productively and minimize the cross communication between processors, which may potentially slow down the computation, we need to contrive an efficient algorithm.

An efficient parallel algorithm to some extent depends on the architecture of the cluster that we use. For example, the Seaborg cluster, on which we implement our parallel algorithm, has 380 computing nodes with each node having 16 processors. Processors on each node have a shared memory pool of 16 to 64 GBytes. The commu-

nication between the processors within a node is much faster than the communication between the processors of different nodes. Hence, care must be taken in designing an algorithm to minimize the communication between the processors of different nodes. Also, the Seaborg cluster supports several optimization modes that further improve the performance of the algorithm. The detailed discussion is beyond the scope of this work, but can be found in [2].

We now highlight some of the aspects of the parallel algorithms for the Laplace solver. Let NPR be the number of processors we choose to use on the cluster for parallel execution, and let NSP be the number of surface elements over which the magnetic field is specified. The master processor will divide the computation of NSP surface points over NPR processors. The master processor itself is a part of the NPR processors.

If the summation over all surface elements is trivially parallelized, each processor computes the partial sum of the magnetic field contributions for the assigned surface elements, and sends the result of the partial sum back to the master processor, where these partial sums are summed up to get the total magnetic field. The number of communications between processors is equal to $k \times NPR$, where k is a constant depending upon the problem.

We now describe a new efficient algorithm for parallelization of the summation over all the surface elements. The master processor will divide the computation of NSP surface points over NPR processors. The NPR processors are split into groups of $N1$ processors each, leading to $N2 = NPR/N1$ groups. The master processor assigns one of the processors in a group as the master processor for the group, and these processors are referred to as sub-masters. The master processor itself is a part of the NPR processors and also a part of the $N2$ sub-masters. The number of processors $N1$ in each group is given by

$$N1 = INT\left(2 \cdot \sqrt{NPR}\right),$$

66

where the INT function finds nearest integer smaller than are equal to $\left(2 \cdot \sqrt{NPR}\right)$. However, if NPR is not exactly divisible by $N1$, then we decrease the value of $N1$ by one, $N1 = (N1 - 1)$. We repeat the process till NPR is exactly divisible by $N1$. This ensures that both $N1$ and $N2$ are integers. Each processor computes the partial sum of the magnetic field contributions for the assigned surface elements, and sends the computed result of the partial sum back to the sub-master processor. Each sub-master processor computes the partial sum of the magnetic field contributions for each group and sends the result of the groups partial sum back to the master processor, where these group partial sums are summed up to get the final field. The number of communications between the processors is roughly equal to $k \times (N1 + N2)$. Since, $(N1 + N2) \ll N1 \times N2$, the communication time is greatly reduced as compared to the trivial parallelization case.

The above algorithm is implemented using the parallel loop block (PLOOP) available in the code COSY INFINITY. The steps are highlighted in Table 3.3.1. We use two nested parallel loop blocks, one over the $N2$ groups and the other over $N1$ processors in each group. At the end of a parallel loop a communication option can be specified to gather computed results from all the processors that have participated in the parallel loop block on to only one processor, which once again minimizes the cross communication between the processors. In the section 4.3.4 we present example of the parallel implementation to compute the magnetic field for the Super-FRS quadrupole magnets.

3.4 Magnetic field due to arbitrary current distribution

In this section we describe a method to compute the magnetic field of an arbitrary current distribution using DA techniques. The motivation to look at this problem

{Loop over N2 groups}
PLOOP JJ 1 N2;

    {Loop over N1 processors}
    PLOOP II 1 N1;

        {Evaluate the processor number PP}
        PP:=II+(JJ-1)*N1;

        [*Code to identify the surface elements JBEG through JEND*
        for which the processor PP will evaluate the partial sum]

        {Loop to compute the partial sum of the scalar and vector potential
        contributions over surface elements JBEG through JEND}
        LOOP IL JBEG JEND;
                ⋮

            [*Code to compute the scalar and the vector potential*
            contribution of a surface element IL.]
                ⋮

        ENDLOOP;

    {End the parallel loop over the group of N1 processors and
    send the results to sub-master processor using communication mode 4}
    ENDPLOOP 4 PN1_SCLPOT PN1_VECPOT;

    {Loop to evaluate group partial sum of N1 processors}
    LOOP II 1 N1;
        ⋮
        [*Summation to get group partial sum GN2_SCLPOT and GN2_VECPOT*]
        ⋮
    ENDLOOP;

{End the parallel loop over the N2 groups and send the results to master processor}
ENDPLOOP 4 GN2_SCLPOT GN2_VECPOT;

{Loop to evaluate sum over N2 groups}
LOOP JJ 1 N2;
    ⋮
    [*Summation to get sum SCLPOT and VECPOT*]
    ⋮
ENDLOOP;

[*Code to evaluate the divergence of SCLPOT and the curl of VECPOT and sum them
to get the magnetic field*]

Table 3.3.1. The code for the parallel algorithm.

comes from the need to design and optimize an accelerator magnet in a simple and in an efficient way. Once again the DA based techniques have the advantage of providing the complete multipole decomposition of the field. It is also straight-forward to verify the that the field computed in the source free region indeed has identically vanishing divergence and curl. Hence, it is guaranteed that the field computed is always Maxwellian. Previous attempts to compute the magnetic field using DA techniques are described in [34, 68].

3.4.1 Field computations using the Biot-Savart law and DA

We first describe a general frame work that uses the Biot-Savart law to compute the field due to an arbitrary current distribution. The Biot-Savart law for line, surface and volume currents is given by

$$\vec{B}\left(\vec{r}\right) \;=\; \frac{\mu_0}{4\pi} \int_l \frac{\vec{I}\left(\vec{r}\right) \times \vec{u}_{\vec{r}-\vec{r}'}}{\left(\vec{r}-\vec{r}'\right)^2} dl' , \tag{3.4.1}$$

$$\vec{B}\left(\vec{r}\right) \;=\; \frac{\mu_0}{4\pi} \int_S \frac{\vec{K}\left(\vec{r}\right) \times \vec{u}_{\vec{r}-\vec{r}'}}{\left(\vec{r}-\vec{r}'\right)^2} da' , \tag{3.4.2}$$

$$\vec{B}\left(\vec{r}\right) \;=\; \frac{\mu_0}{4\pi} \int_V \frac{\vec{J}\left(\vec{r}\right) \times \vec{u}_{\vec{r}-\vec{r}'}}{\left(\vec{r}-\vec{r}'\right)^2} d\tau' , \tag{3.4.3}$$

where $\vec{I}$ is a current vector, and the surface current density vector $\vec{K}$ is the current per unit width perpendicular to the current flow, and the volume current density vector $\vec{J}$ is the current per unit area perpendicular to the flow of the current. The vector $\vec{r}-\vec{r}'$ points from the current element at $\vec{r}'$ to the observation point $\vec{r}$ where we want to compute the magnetic field. The vector $\vec{u}_{\vec{r}-\vec{r}'}$ represents the unit vector in this direction. The magnetic constant, μ_0, is the permeability of vacuum. In SI units, the value is exactly expressed by $\mu_0 = 4\pi \times 10^{-7}\,\mathrm{N\,A^{-2}}$. In most cases numerical integration is usually required to find the total magnetic field at any point.

The general idea is to discretize the domain and express the integral over the domain as the sum of integrals over smaller intervals. Depending on the type of the problem, we express the domain in terms of one, two or three parameters and scale them such that the new domain is a box $[-1, 1]^n$, where n is number of parameters. We then Taylor expand the kernel in terms of the previously defined parameters and integrate it. We first present two analytical examples to describe the DA approach to obtain the multipole decomposition of the magnetic field for the line and surface currents. And, in the section 3.4.4 we describe the technique to find the magnetic field for the volume current distribution.

3.4.2   Line current example: circular loop

For a circular loop with its axis oriented in the $\hat{z}$ direction, the analytic formula for the magnetic field on the z-axis is given by

$$\vec{B}(0, 0, z) = \frac{\mu_0}{4\pi} \frac{2\pi R^2 I}{\left(z^2 + R^2\right)^{\frac{3}{2}}} \hat{z}.$$

We choose an example with radius $R = 0.4\ m$ and current of $I = 1\ A$. For this example, the eighth order expansion of the $\hat{z}$ component of the magnetic field at $z = 0$ is given in Table 3.4.1.

I	COEFFICIENT	ORDER	EXPONENTS		
1	0.1570796326794896E-05	0	0	0	0
2	-.1472621556370215E-04	2	0	0	2
3	0.1150485590914231E-03	4	0	0	4
4	-.8388957433749600E-03	6	0	0	6
5	0.5898485695605188E-02	8	0	0	8

Table 3.4.1. A eighth order Taylor expansion of the analytic formula for the z component of the magnetic field of a circular coil on the central axis.

In the representation of the Taylor expansion above, the entries in the first column provide the number assigned to each of the coefficients in the Taylor expansion to easily identify them. The entries in the second column provide the numerical value of the coefficients. The entries in the fourth, fifth and the sixth columns provide the expansion orders with respect to the observation point (x, y, z). The total order for each coefficient is the sum of all the orders in columns four through eight, which is given in the third column.

We now use a DA based approach to solve this problem. Let the point $\vec{r} = (x, y, z)$ be the observation point. We discretize the length of the current loop into $N = 4000$ current elements of length $(2\pi R) / N$. Let (x_n, y_n, z_n) describe a point inside the nth current element, where $n = 1, \ldots, N$. And let s be a parameter such that

$$
\begin{aligned}
x_n &= R \cdot \cos\left(\triangle_s \cdot (n - 0.5 + 0.5s)\right), && (3.4.4) \\
y_n &= R \cdot \sin\left(\triangle_s \cdot (n - 0.5 + 0.5s)\right), \\
z_n &= 0,
\end{aligned}
$$

where $\triangle_s = 2\pi/N$ and $s \in [-1, 1]$. By varying s we can now get all points inside any given current element which is centered at $\vec{r}_n^{\,\prime} = (R \cdot \cos(n \cdot \triangle_s), R \cdot \sin(n \cdot \triangle_s), 0)$. We can now compute the contribution due to the current element at $\vec{r}_n^{\,\prime}$ using the Biot-Savart law for a line current, the equation (3.4.1), by first expressing the integral in terms of the new parameter s using the equation (3.4.4), and then expanding the kernel in terms of the variables x, y, z and s. We then integrate the resulting polynomial with respect to s in the interval $[-1, 1]$. Finally, we sum up the contribution due to all the current elements to get the resulting field at (x, y, z). The Taylor expansion of the $\hat{z}$ component of the magnetic field, $\vec{B}(x, y, z)$, computed using the DA framework available in the code COSY INFINITY is given in Table 3.4.2.

Note that the expansion given in Table 3.4.2 reduces to the expansion for the

I	COEFFICIENT	ORDER	EXPONENTS
1	0.1570796326794921E-05	0	0 0 0 0
2	0.7363107781851075E-05	2	2 0 0 0
3	0.7363107781851056E-05	2	0 2 0 0
4	-.1472621556370156E-04	2	0 0 2 0
5	0.4314320965821285E-04	4	4 0 0 0
6	0.8628641931856381E-04	4	2 2 0 0
7	0.4314320965821278E-04	4	0 4 0 0
8	-.3451456772742676E-03	4	2 0 2 0
9	-.3451456772742692E-03	4	0 2 2 0
10	0.1150485590914342E-03	4	0 0 4 0
11	0.2621549198046754E-03	6	6 0 0 0
12	0.7864647594140242E-03	6	4 2 0 0
13	0.7864647594140274E-03	6	2 4 0 0
14	0.2621549198046748E-03	6	0 6 0 0
15	-.4718788556484144E-02	6	4 0 2 0
16	-.9437577112968266E-02	6	2 2 2 0
17	-.4718788556484138E-02	6	0 4 2 0
18	0.6291718075312196E-02	6	2 0 4 0
19	0.6291718075312182E-02	6	0 2 4 0
20	-.8388957433749353E-03	6	0 0 6 0

Table 3.4.2. A sixth order Taylor expansion of the z component of the magnetic field computed for the circular loop example.

analytic case, Table 3.4.1, when $x = 0, y = 0$. The result that we get is valid as long as the observation point does not lie on the current loop. This case will require special treatment. It is also easy to verify that the magnetic field computed here is divergence less and curl free.

The DA technique that we develop here can easily be generalized to compute the magnetic field due to the current on a wire of arbitrary shape and orientation in space. We only need the discretization information and the parametrization over each current element to compute the magnetic field.
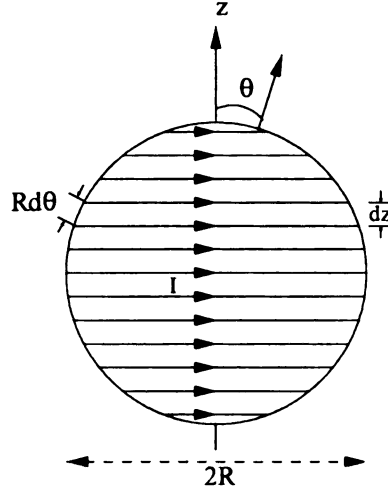
Figure 3.4.1. The cross section of a flux ball consisting of a sphere with winding on its surface.

3.4.3 Surface current example: spherical coil

For the case of a properly wound spherical coil the magnetic field inside has the property that it is uniform. The current density on the surface can be thought of as a sinusoidally distribution between the north and south poles of a sphere. Current loops of appropriately varying diameter, spaced evenly as projected onto the $\hat{z}$ axis, automatically simulate such a distribution. The coil, with a radius R and a wire carrying the current I, is shown in Figure 3.4.1.

To deduce the surface current density representing this winding, note that the density of turns on the surface is the total number, N, divided by the total length, $2R$, and so the number of turns in the incremental length dz is $(N/2R)\,dz$. Since $z = r\cos\theta$, a differential length dz corresponds to an angular increment $d\theta/dz = -R\sin\theta$. Therefore, the number of turns in the differential length $Rd\theta$ as measured along the periphery of the sphere is $(N/2R)\sin\theta$. With each turn carrying the current I, the surface current density is

$$\vec{K} = \hat{i}_\phi \frac{N}{2R} I \sin\theta$$

73
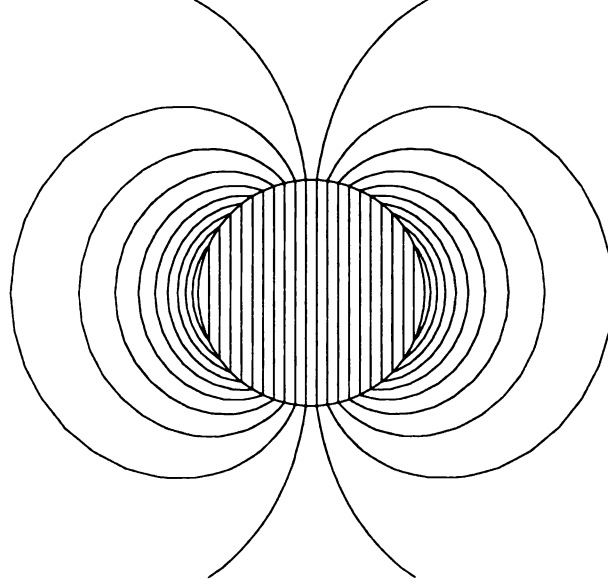
Figure 3.4.2. Magnetic field lines for the spherical coil.

The magnetic field intensity for such a surface current distribution is shown in Figure 3.4.2. The field inside the sphere is constant.

The magnetic field inside and outside the sphere is as follows.

$$\vec{B} = \mu_0 \frac{NI}{3R} \left(\cos\left(\theta\right) \hat{\imath}_r - \sin\left(\theta\right) \hat{\imath}_\theta \right) = \frac{\mu_0}{4\pi} \frac{NI}{3R} \hat{z}, \qquad r < R$$

$$\vec{B} = \mu_0 \frac{NI}{6R} \left(\frac{R}{r} \right)^3 \left(2 \cos\left(\theta\right) \hat{\imath}_r + \sin\left(\theta\right) \hat{\imath}_\theta \right), \qquad r > R$$

The exterior lines of the magnetic field intensity are those of a dipole, while the interior field is uniform. Figure 3.4.2, shows the magnetic field lines.

We consider a specific case where we choose the radius of sphere $R = 0.4\ m$ and the total current, NI, such that $\frac{NI}{2R} = 1000\ A/m$. The analytic formula then gives the $\hat{z}$ component of the field inside the sphere to be $\frac{8}{3}\pi \times 10^{-4} = 0.8377580409572781 \times 10^{-03}$ Tesla. We now use a DA based approach to solve this problem. Let the point $\vec{r} = (x, y, z)$ be the observation point. Let $N_x = N_y = 88$ be the number of subdivisions in azimuthal θ and polar ϕ angles, leading to $N_x \times N_y$ surface elements. Let $\left(X_{i,j}, Y_{i,j}, Z_{i,j} \right)$ describe a point inside the (i,j)-th surface element and $\vec{K}_{i,j}$

describe the surface current on the (i, j)-th surface element, where $i = 1, \ldots, N_x$ and $j = 1, \ldots, N_y$. The point $\left(R, \theta_i, \phi_j \right)$ in spherical coordinates is equivalent to the point $\left(X_{i,j}, Y_{i,j}, Z_{i,j} \right)$ in the Cartesian coordinates. The surface elements and the current at (i, j) can now be described in terms of two parameters, x_s and y_s, such that

$$
\begin{aligned}
\phi_i &= \triangle_x \cdot (i - 0.5 + 0.5 x_s) \\
\theta_j &= \triangle_y \cdot (j - 0.5 + 0.5 y_s) \\
X_{i,j} &= R \cdot \cos(\phi_i) \cdot \sin\left(\theta_j\right) \\
Y_{i,j} &= R \cdot \sin(\phi_i) \cdot \sin\left(\theta_j\right) \\
Z_{i,j} &= R \cdot \cos\left(\theta_j\right) \\
\vec{K}_{i,j} &= \frac{NI}{2R} \cdot \sin\left(\theta_j\right) \cdot \left(-\sin(\phi_i)\, \hat{x} + \cos(\phi_i)\, \hat{y} \right),
\end{aligned}
\tag{3.4.5}
$$

where $\triangle_x = 2\pi / N_x$, $\triangle_y = 2\pi / N_y$ and $x_s, y_s \in [-1, 1]$. By varying x_s, y_s we can now get all points inside any given surface element. We can now compute the contribution due to the surface element at $\vec{r}_n'$ using the Biot-Savart law for the surface current, the equation (3.4.1), by first expressing the integral in terms of the new parameters x_s and y_s using the equation (3.4.5), and then expanding the kernel in terms of the three volume variable x, y, z, and the two surface variables x_s and y_s. We then integrate the resulting polynomial with respect to (x_s, y_s) over the domain $[-1, 1] \times [-1, 1]$. Finally, we sum up the contribution due to all the surface elements to get the resulting field at (x, y, z). The $\hat{z}$ component of the magnetic field, $\vec{B}(x, y, z)$, computed using the DA framework available in the code COSY INFINITY is given in Table 3.4.3

Note that the zeroth order term in the Taylor expansion given in Table 3.4.3 agrees with the values computed using the analytic formula. The result that we get is valid as long as the observation point does not lie on the surface. This case will require special treatment. It is also easy to verify that the magnetic field computed here is divergence less and curl free.

```
MAGNETIC FIELD (Bx,By,BZ)
      0.000000000000      0.000000000000      0.8377580409801E-03 00000
      0.000000000000      0.000000000000     -0.7490871758478E-12 20000
      0.000000000000      0.000000000000     -0.7490871081318E-12 02000
     -0.1496412647114E-11 0.000000000000      0.000000000000      10100
      0.000000000000     -0.1496412522919E-11 0.000000000000      01100
      0.000000000000      0.000000000000      0.1496363218034E-11 00200
      0.000000000000      0.000000000000      0.1406498322650E-08 40000
      0.000000000000      0.000000000000      0.2812995931364E-08 22000
      0.000000000000      0.000000000000      0.1406498327655E-08 04000
      0.5625993567287E-08 0.000000000000      0.000000000000      30100
      0.000000000000      0.5625991024637E-08 0.000000000000      21100
      0.5625991025586E-08 0.000000000000      0.000000000000      12100
      0.000000000000      0.5625993571062E-08 0.000000000000      03100
      0.000000000000      0.000000000000     -0.1125198581064E-07 20200
      0.000000000000      0.000000000000     -0.1125198581536E-07 02200
     -0.7501323883764E-08 0.000000000000      0.000000000000      10300
      0.000000000000     -0.7501323883789E-08 0.000000000000      01300
      0.000000000000      0.000000000000      0.3750661939904E-08 00400
      0.1072194029532E-15 0.000000000000      0.000000000000      31100
----------------------------------------------------------------------
```

Table 3.4.3. A fourth order Taylor expansion of the z component of the magnetic field computed for the spherical coil example.

Once again, the DA technique that we develop here can easily be generalized to compute the magnetic field due to an arbitrary surface current distribution. We only need the discretization information and the parametrization over each surface element to compute the magnetic field.

3.4.4 Three dimensional current distribution

We discuss the three-dimensional case by using the example of the current in the straight wire with a finite cross section. This particular case is of practical importance and we will use this to develop tools to design new accelerator magnets. These tools will then be used to design a 3D model of a quadrupole magnet in the section 4.1.

Magnetic field computation for a wire with a rectangular cross section using DA

We first develop a framework to express a point inside a finite length current wire of a rectangular cross section that is oriented in an arbitrary direction in the 3D space. This would then facilitate the implementation of the Biot-Savart law and Ampere's law in the differential algebraic (DA) framework.

Let $\hat{n}_1$ and $\hat{n}_2$ be two unit vectors on a plane ($\hat{n}_1 \neq \hat{n}_2$), then any point on the plane can be given as $\lambda_1 \hat{n}_1 + \lambda_2 \hat{n}_2$, where the parameters λ_1 and λ_2 are any real numbers. The unit vector $\hat{n}_\perp = \hat{n}_1 \times \hat{n}_2$ along with two points on the plane completely defines the plane formed by the unit vectors $\hat{n}_1$ and $\hat{n}_2$. In the special case where $\hat{n}_1$ is perpendicular to $\hat{n}_2$ ($\hat{n}_1 \cdot \hat{n}_2 = 0$) and $\lambda_1, \lambda_2 \in [-1, 1]$, the vector $(\lambda_1 \hat{n}_1 + \lambda_2 \hat{n}_2)/2$ describes a point inside a unit square lying on the plane and centered at the origin. We can translate and scale this unit box to describe a rectangle lying on this plane. The vector $\vec{V}_p$ defined by

$$\vec{V}_p = \vec{V}_c + 0.5 \cdot (\lambda_1 b \cdot \hat{n}_1 + \lambda_2 w \cdot \hat{n}_2), \tag{3.4.6}$$

describes a point inside a rectangle of the length b and width w and centered at a point $\vec{V}_c$. All points inside the rectangle are completely described by the two parameters (λ_1, λ_2) and are independent of the actual dimensions of the rectangle and its orientation in the three dimensional space. In other words, we have projected the area of the rectangle oriented in an arbitrary direction in the three dimensional space on to a square described by the parameters (λ_1, λ_2).

For the case of a rectangular box of height l, let the cross section be defined by the unit vectors $\hat{n}_1$ and $\hat{n}_2$. The center point of the rectangular cross section lies on a straight line whose direction is given by the unit vector $\hat{n}_\perp$. A point on this line can be expressed by

$$\vec{V}_c = \vec{V}_{c_0} + \lambda_3 \cdot \hat{n}_\perp,$$

where the vector $\vec{V}_{c_0}$ is the center of a face on the rectangular box that is perpendicular to the unit vector $\hat{n}_\perp$, and $\lambda_3 \in [0, l]$. The parameters $(\lambda_1, \lambda_2, \lambda_3)$ then completely describe a rectangular box. Any point inside the box is given by

$$\vec{V}_p^{box} = \vec{V}_{c_0} + 0.5 \cdot (\lambda_1 b \cdot \hat{n}_1 + \lambda_2 w \cdot \hat{n}_2) + \lambda_3 \cdot \hat{n}_\perp. \qquad (3.4.7)$$

Once again, we have projected the volume of the rectangular box oriented in an arbitrary direction on to a box defined by the parameters $(\lambda_1, \lambda_2, \lambda_3)$. The equations (3.4.6) and (3.4.7) will be used in the next two sections to express the Biot-Savart law and Ampere's law in the DA framework.

Magnetic field of a wire with a rectangular cross section using the Biot-Savart law and DA

We can choose the direction of the current in the wire to coincide with the unit vector $\hat{n}_\perp$. Using the Biot-Savart law, we can write the magnetic field at an observation point $\vec{r}$ as

$$\vec{B}(\vec{r}) = \frac{\mu_0}{4\pi} \frac{I_0}{b \cdot w} \int_{-1}^{1} \int_{-1}^{1} \left[\int_0^l \frac{\left(\hat{n}_\perp \times \left(\vec{r} - \vec{V}_p^{box}\right)\right)}{\left|\vec{r} - \vec{V}_p^{box}\right|^2} \cdot d\lambda_3 \right] d\lambda_2 \cdot d\lambda_1. \qquad (3.4.8)$$

To perform integration with respect to λ_3 in the equation (3.4.8), we first split the domain of integration into smaller intervals. Let the length l be divided into N parts of the size $h = l/N$. Then the parameter λ_3 can be written as

$$\lambda_3(i) = (i + 0.5 \cdot v) \cdot h,$$

where $i = 0.5, \ldots, (N - 0.5)$, and $v \in [-1, 1]$. The position of a point inside the box in terms of the new parameters $(\lambda_1, \lambda_2, v)$ is given by

$$\vec{V}_p^{box}(i, \lambda_1, \lambda_2, v) = \vec{V}_{c_0} + ih \cdot \hat{n}_\perp + 0.5 \cdot (\lambda_1 b \cdot \hat{n}_1 + \lambda_2 w \cdot \hat{n}_2 + vh \cdot \hat{n}_\perp). \qquad (3.4.9)$$

The equation (3.4.8) can now be written as

$$\vec{B}\left(\vec{r}\right) = \frac{\mu_0}{4\pi} \frac{I_0}{b \cdot w} \sum_{i=0.5}^{i=N-0.5} \int_{-1}^{1} \int_{-1}^{1} \int_{-1}^{1} \frac{\left(\hat{n}_\perp \times \left(\vec{r} - \vec{V}_p^{box}\left(i\right)\right)\right)}{\left|\vec{r} - \vec{V}_p^{box}\left(i\right)\right|^2} \cdot \frac{l}{N} \cdot dv \cdot d\lambda_2 \cdot d\lambda_1.$$

(3.4.10)

The parameters $(\lambda_1, \lambda_2, v)$ become the DA variables with respect to which the kernel of the integral in the equation (3.4.10) is expanded to a high order. In the DA framework it is straightforward to perform the volume integral over the resulting polynomial representation.

In the DA frame work it is also straightforward to treat the wires with rectangular cross sections that have curved endings rather than the straight endings that are perpendicular to the direction of the current flow. Let the two surfaces at the start and the end of the wire carrying the current be expressed as $\lambda_3 = g\left(\lambda_1, \lambda_2\right)$ and $\lambda_3 = f\left(\lambda_1, \lambda_2\right)$. We can use the equation (3.4.10) to find the magnetic field due to this new configuration by noting

$$h\left(\lambda_1, \lambda_2\right) = \frac{f\left(\lambda_1, \lambda_2\right) - g\left(\lambda_1, \lambda_2\right)}{N},$$

where the step h is now a function of the parameters (λ_1, λ_2). The equation (3.4.9) can be modified to express a point inside the rectangular box with curved endings as

$$\begin{aligned}
\vec{V}_p^{box}\left(i, \lambda_1, \lambda_2, v\right) &= \vec{V}_{c_0} + \left(g\left(\lambda_1, \lambda_2\right) + i \cdot h\left(\lambda_1, \lambda_2\right)\right) \cdot \hat{n}_\perp \\
&\quad + 0.5 \cdot \left(\lambda_1 b \cdot \hat{n}_1 + \lambda_2 w \cdot \hat{n}_2 + v \cdot h\left(\lambda_1, \lambda_2\right) \cdot \hat{n}_\perp\right).
\end{aligned}$$

When the surfaces are just inclined planes, the functions f and g are just linear combinations of the parameters λ_1 and λ_2. This special case is useful in the implementation of the numerical tool to compute the magnetic field due to a coil carrying a current with a rectangular cross section .

Magnetic field of an infinitely long wire with a rectangular cross section using Ampere's law and DA

Once again, we can choose the direction of the current in the infinitely long wire with a rectangular cross section to coincide with the unit vector $\hat{n}_\perp$. The closest distance $r_\perp$ between the observation point $\vec{r}$ and the line passing through the point $\vec{V}_p$ and in the direction $\hat{n}_\perp$ is given by

$$r_\perp = \left| \left(\vec{r} - \vec{V}_p \right) - \left(\hat{n}_\perp \cdot \left(\vec{r} - \vec{V}_p \right) \right) \hat{n}_\perp \right|,$$

where $\vec{V}_p$ is given by the equation (3.4.6). Ampere's law can then be written as

$$\vec{B}\left(\vec{r}\right) = \int_{-1}^{1} \int_{-1}^{1} \frac{\mu_0}{2\pi} \frac{I_0}{b \cdot w} \frac{\left(\hat{n}_\perp \times \left(\left(\vec{r} - \vec{V}_p \right) / \left| \left(\vec{r} - \vec{V}_p \right) \right| \right) \right)}{r_\perp} d\lambda_1 \cdot d\lambda_2. \qquad (3.4.11)$$

The equation (3.4.11) can be used to compute the magnetic field of an infinitely long wire with a rectangular cross section . The parameters (λ_1, λ_2) become the DA variables with respect to which the kernel of the integral in the equation (3.4.11) is expanded to high order, and DA integration is performed over the resulting polynomial representation.

COSY INFINITY tools for magnetic field computations

Due to their frequent use in the magnet design, a dedicated set of tools has been written for the rectangular cross section wire and coil in the code COSY INFINITY [23, 24]. These tools use the differential algebraic framework available in COSY IN-FINITY [23, 24] to Taylor expand, integrate and evaluate the kernels appearing in the equations (3.4.11) and (3.4.10). In addition to providing highly accurate results in the form of the local Taylor expansion of the magnetic field, the DA based implementation has a unique advantage of easily obtaining the curl and divergence of the magnetic field at any given point. This offers one way to quickly verify if the magnetic field satisfies Maxwell's equations.

One of the tools computes the magnetic field of a finite wire of a rectangular cross section. A finite wire can have the current entrance and exit planes inclined to the central axis or the direction of the current flow. Also, a tool to compute the field for an infinitely long wire with a rectangular cross section has been implemented. Using orders around 10, accuracy of about 14 digits can be achieved using these tools. Another tool to compute the magnetic field of a current coil of a rectangular cross section has also been implemented. More detail about the current coil implementation will be given in the section 4.1.2.

In general, a numerical tool to compute the magnetic field for an infinitely often differentiable current distribution can also be implemented using concepts above and the DA framework available in the code COSY INFINITY [23, 24].

3.5 Extraction of transfer map from surface field data or current distribution

In the sections 3.1 and 3.4 we have successfully demonstrated that we can obtain local expansion of the magnetic field by either using the surface data or the current distribution. We now use the technique described in section 2.3.2 to demonstrate that we can successfully extract transfer map from the surface field data. The field information at 13 point of each time step in the Runge-Kutta integrator is supplied as local expansion of the magnetic field computed using the techniques we have developed.

We present the results for a test case of theoretical quadrupole magnetic field for which the analytic transfer map is know. The quadrupole field varies linearly with the distance from the magnet center, $\vec{B}\left(x, y, s\right) = (k_q y, k_q x, 0)$, where k_q is a constant and has units of T/m. The quadrupole magnet focuses the beam along one plane while defocusing the beam along the other plane. We note that the radius of curvature, $h = 0$, for the quadrupole magnet. The equation (2.3.3) can now be linearized to

obtain

$$x' = a,$$

$$y' = b,$$

$$a' = -\frac{k_q}{\chi_{m0}}x,$$

$$b' = \frac{k_q}{\chi_{m0}}y,$$

$$l' = -\frac{k}{v_0}\frac{1}{(1+\eta_0)(2+\eta_0)}\delta,$$

$$\delta' = 0.$$

Let $\omega = \sqrt{k_q/\chi_{m0}}$, and $D = -k/(v_0(1+\eta_0)(2+\eta_0))$ and L be length of the quadrupole. It is straight forward to solve the above system of ODEs to obtain the first order transfer map for the quadrupole, which is given as

$$\mathcal{M} = \begin{pmatrix} \cos(\omega L) & \sin(\omega L)/\omega & 0 & 0 & 0 & 0 \\ -\omega\sin(\omega L) & \cos(\omega L) & 0 & 0 & 0 & 0 \\ 0 & 0 & \cosh(\omega L) & \sinh(\omega L)/\omega & 0 & 0 \\ 0 & 0 & \omega\sinh(\omega L) & \cosh(\omega L) & 0 & 0 \\ 0 & 0 & 0 & 0 & 1 & D \\ 0 & 0 & 0 & 0 & 0 & 1 \end{pmatrix}.$$

It is also possible to obtain similar analytic formulae for the high order coefficients [27].

We compare the transfer map computed using the analytical formulas and the transfer map computed using Runge-Kutta integrator with the magnetic field computed using the Laplace solver we have developed. For the case a quadrupole of length 0.2 m, 0.1 m aperture and field strength at the aperture of 6.725×10^{-2} T we computed the difference between the transfer maps. The result is presented in tables 3.5.1 and 3.5.2. We can see that the agreement between the analytic and computed Taylor maps is very good, and this once again demonstrate that the magnetic field generated by the techniques we have developed are highly accurate. This examples also serves and a proof that we can extract transfer maps from the measured surface field data using

82

the techniques we have developed. In the section 4.3.4 we will present the example of the Super-FRS quadrupole magnet for which we will extract the transfer map using the magnetic field data on a closed surface.

3.6   Summary
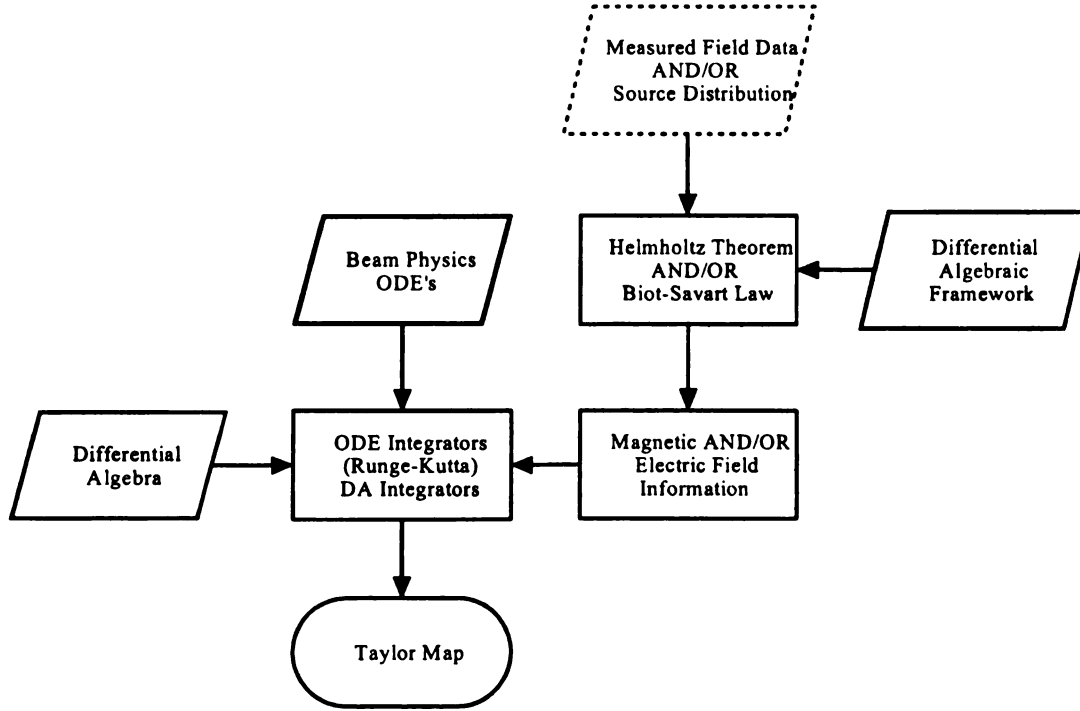
Figure 3.6.1. The flow chart for extracting transfer maps from the measured magnetic field data or the source distribution.

A new technique for finding the multipole expansion solution of the three dimensional Poisson equation using the surface data and the current distribution inside the volume enclosed by the surface has been developed. Since this new technique uses the field information on the surface enclosing the volume of interest and is implemented using the high-order multivariate differential algebraic tools, the accuracy achieved is much higher than that of conventional field solvers. If the data on the surface

```
-.7127632E-13  -.7115593E-12   .0000000E+00   .0000000E+00   .0000000E+00  100000
-.4718448E-14  -.7105427E-13   .0000000E+00   .0000000E+00   .0000000E+00  010000
 .0000000E+00   .0000000E+00   .7149836E-13   .7143869E-12   .0000000E+00  001000
 .0000000E+00   .0000000E+00   .4718448E-14   .7127632E-13   .0000000E+00  000100
 .0000000E+00   .0000000E+00   .0000000E+00   .0000000E+00  -.7057580E-15  200000
 .0000000E+00   .0000000E+00   .0000000E+00   .0000000E+00   .3560542E-13  110000
 .0000000E+00   .0000000E+00   .0000000E+00   .0000000E+00   .2366163E-14  020000
 .0000000E+00   .0000000E+00   .0000000E+00   .0000000E+00  -.7064949E-15  002000
 .0000000E+00   .0000000E+00   .0000000E+00   .0000000E+00  -.3588926E-13  001100
 .3567199E-13  -.7027697E-15   .0000000E+00   .0000000E+00   .0000000E+00  100001
 .4732326E-14   .3557007E-13   .0000000E+00   .0000000E+00   .0000000E+00  010001
 .0000000E+00   .0000000E+00  -.3581380E-13  -.7045552E-15   .0000000E+00  001001
 .0000000E+00   .0000000E+00   .0000000E+00   .0000000E+00  -.2400857E-14  000200
 .0000000E+00   .0000000E+00  -.4787837E-14  -.3571015E-13   .0000000E+00  000101
 .1250188E-12   .1237387E-11   .0000000E+00   .0000000E+00   .0000000E+00  300000
 .2769872E-13   .3679666E-12   .0000000E+00   .0000000E+00   .0000000E+00  210000
-.1039776E-12   .5195115E-13   .0000000E+00   .0000000E+00   .0000000E+00  120000
-.9048318E-14  -.3291182E-13   .0000000E+00   .0000000E+00   .0000000E+00  030000
 .0000000E+00   .0000000E+00  -.3758715E-12  -.3729083E-11   .0000000E+00  201000
 .0000000E+00   .0000000E+00  -.6323985E-13  -.7413065E-12   .0000000E+00  111000
 .0000000E+00   .0000000E+00   .3319892E-13  -.3679442E-13   .0000000E+00  021000
-.3321907E-12  -.3294149E-11   .0000000E+00   .0000000E+00   .0000000E+00  102000
-.2018379E-13  -.3273745E-12   .0000000E+00   .0000000E+00   .0000000E+00  012000
 .0000000E+00   .0000000E+00   .1109808E-12   .1101801E-11   .0000000E+00  003000
 .0000000E+00   .0000000E+00  -.2223924E-13  -.3691161E-12   .0000000E+00  200100
 .0000000E+00   .0000000E+00  -.7609278E-13  -.8903396E-13   .0000000E+00  110100
 .0000000E+00   .0000000E+00  -.1665335E-15   .3047020E-13   .0000000E+00  020100
-.3292882E-13  -.6518573E-12   .0000000E+00   .0000000E+00   .0000000E+00  101100
 .6717630E-13  -.1018835E-12   .0000000E+00   .0000000E+00   .0000000E+00  011100
 .0000000E+00   .0000000E+00   .2599943E-13   .3276678E-12   .0000000E+00  002100
 .0000000E+00   .0000000E+00   .0000000E+00   .0000000E+00   .1057490E-14  200001
 .0000000E+00   .0000000E+00   .0000000E+00   .0000000E+00  -.5331369E-13  110001
 .0000000E+00   .0000000E+00   .0000000E+00   .0000000E+00  -.4746203E-14  020001
 .0000000E+00   .0000000E+00   .0000000E+00   .0000000E+00   .1057172E-14  002001
-.3793775E-13  -.5576818E-13   .0000000E+00   .0000000E+00   .0000000E+00  100200
-.2498002E-15  -.4481073E-13   .0000000E+00   .0000000E+00   .0000000E+00  010200
 .0000000E+00   .0000000E+00   .1101168E-12   .4617591E-13   .0000000E+00  001200
 .0000000E+00   .0000000E+00   .0000000E+00   .0000000E+00   .5388008E-13  001101
-.2672016E-13   .5264869E-15   .0000000E+00   .0000000E+00   .0000000E+00  100002
-.4732326E-14  -.2664362E-13   .0000000E+00   .0000000E+00   .0000000E+00  010002
 .0000000E+00   .0000000E+00   .2686198E-13   .5285215E-15   .0000000E+00  001002
 .0000000E+00   .0000000E+00   .1000589E-13   .3795380E-13   .0000000E+00  000300
 .0000000E+00   .0000000E+00   .0000000E+00   .0000000E+00   .4787837E-14  000201
 .0000000E+00   .0000000E+00   .4815592E-14   .2678565E-13   .0000000E+00  000102
```

Table 3.5.1. The difference between the analytic and the computed Taylor maps. The difference map is shown to the third order .

```
.0000000E+00 -.5380633E-15  .0000000E+00  .0000000E+00  .1222132E-14 400000
.0000000E+00 -.2578822E-15  .0000000E+00  .0000000E+00 -.6219813E-13 310000
.0000000E+00  .0000000E+00  .0000000E+00  .0000000E+00 -.1498060E-13 220000
.0000000E+00  .0000000E+00  .0000000E+00  .0000000E+00  .5182920E-13 130000
.0000000E+00  .0000000E+00  .0000000E+00  .0000000E+00  .4468648E-14 040000
.0000000E+00  .0000000E+00  .1829428E-15  .2166037E-14  .0000000E+00 301000
.0000000E+00  .0000000E+00  .0000000E+00  .8101576E-15  .0000000E+00 211000
.2389887E-15  .3119767E-14  .0000000E+00  .0000000E+00  .3914068E-15 202000
.0000000E+00  .7771467E-15  .0000000E+00  .0000000E+00  .1665009E-12 112000
.0000000E+00  .0000000E+00  .0000000E+00  .0000000E+00  .9770657E-14 022000
.0000000E+00  .0000000E+00 -.1748517E-15 -.2071154E-14  .0000000E+00 103000
.0000000E+00  .0000000E+00  .0000000E+00 -.2469727E-15  .0000000E+00 013000
.0000000E+00 -.5266477E-15  .0000000E+00  .0000000E+00 -.1087287E-14 004000

                              ⋮

.2226095E-13 -.4383921E-15  .0000000E+00  .0000000E+00  .0000000E+00 100003
.4767020E-14  .2219503E-13  .0000000E+00  .0000000E+00  .0000000E+00 010003
.0000000E+00  .0000000E+00 -.2240254E-13 -.4406926E-15  .0000000E+00 001003
.0000000E+00  .0000000E+00  .0000000E+00  .0000000E+00 -.5058454E-14 000400
.0000000E+00  .0000000E+00 -.2059464E-13 -.5711100E-13  .0000000E+00 000301
.0000000E+00  .0000000E+00  .0000000E+00  .0000000E+00 -.7202572E-14 000202
.0000000E+00  .0000000E+00 -.4773959E-14 -.2233597E-13  .0000000E+00 000103
.5283285E-10  .5267736E-09  .0000000E+00  .0000000E+00  .0000000E+00 500000
.1758265E-10  .2631307E-09  .0000000E+00  .0000000E+00  .0000000E+00 410000
.3701574E-11  .7016947E-10  .0000000E+00  .0000000E+00  .0000000E+00 320000
.4778458E-12  .1071568E-10  .0000000E+00  .0000000E+00  .0000000E+00 230000
-.9821050E-13  .8942905E-12  .0000000E+00  .0000000E+00  .0000000E+00 140000
-.1018630E-13  .5400845E-14  .0000000E+00  .0000000E+00  .0000000E+00 050000
.0000000E+00  .0000000E+00 -.2646860E-09 -.2644290E-08  .0000000E+00 401000
.0000000E+00  .0000000E+00 -.7049192E-10 -.1056648E-08  .0000000E+00 311000
.0000000E+00  .0000000E+00 -.1076331E-10 -.2114512E-09  .0000000E+00 221000

                              ⋮

.0000000E+00  .0000000E+00  .1961116E-13  .3858557E-15  .0000000E+00 001004
.0000000E+00  .0000000E+00  .1680600E-13  .1921857E-14  .0000000E+00 000500
.0000000E+00  .0000000E+00  .0000000E+00  .0000000E+00  .1550149E-13 000401
.0000000E+00  .0000000E+00  .3178013E-13  .7154130E-13  .0000000E+00 000302
.0000000E+00  .0000000E+00  .0000000E+00  .0000000E+00  .9658940E-14 000203
.0000000E+00  .0000000E+00  .4787837E-14  .1955467E-13  .0000000E+00 000104
---------------------------------------------------------------------
```

Table 3.5.2. The difference between the analytic and the computed Taylor maps. The difference map shows some of the fourth and the fifth order terms.

enclosing the volume of interest can be given exactly, then in principle, arbitrarily high accuracy limited only by the computational resources available can be achieved by this new technique. In practical situations where the field data on the surface enclosing the volume of interest are experimentally measured, the discretization of the surface and the errors in the experimentally measured field data may limit the accuracy achieved, but because the method is naturally smoothing, the accuracy is expected to exceed that of the measurements. In addition, we have also developed framework to compute the magnetic field of an arbitrary current distribution using the Biot-Savart law. Using these techniques we can now extract the Taylor transfer maps from the measured field data or the source data. Figure 3.6.1 shows the flow-chart to extract the Taylor transfer maps from the measured magnetic fields data or the source distribution.

CHAPTER 4

Applications

In this chapter we present examples to demonstrate the utility of the new field computation techniques we have developed. We first present the design of the new quadrupole magnet with elliptic cross section and tunable high order multipoles. Next, we present the application of the Laplace solver to the realistic case of measure magnetic field data obtained for the MAGNEX spectrometer dipole magnet. Finally, we present the ion-optic simulations for the Super-FRS and present the field computations for the quadrupole magnet utilizing the high performance parallel computing environment.

4.1   The conceptual design of a quadrupole magnet

For charged particle beams that are wider in the dispersive plane than the transverse plane it is cost efficient to utilize magnets that accept beams with elliptic cross sections . We now present the conceptual design of a quadrupole magnet with an elliptic cross section and with tunable high order multipoles. The design consists of 18 superconducting racetrack coils placed on two hollow concentric rhombic prism

support structures.

The analysis of this design will use the new numerical tools that we have described in the section 3.4.4 to compute the local Taylor expansion of the magnetic field starting from the Biot-Savart law and Ampere's law. In this section we first discuss the case where the magnet is considered to be infinitely long. This leads to purely transverse magnetic fields (2D fields). In the section 4.1.1 we present results of numerical computations for this 2D case. We also discuss the feasible range of multipole field strength that can be achieved with this design. Finally, in the section 4.1.2 we present the results for a finite length magnet and discuss the fringe field effects.

A combination of superconducting racetrack coils is used to produce the desired magnetic field inside an elliptic cross section. By the proper choice of dimensions, current density, and placement of these coils, various combinations of the quadrupole field and the higher order multipole fields can be achieved. The support structure that holds these coils in place consists of two concentric hollow rhombic prisms, with the ratio of the diagonals of the rhombus equal to 2. The cross section view showing the arrangement of the current coils on the support structure is shown in Figure 4.1.1. The superconducting racetrack coils on the inner rhombic prism produce quadrupole and octupole fields. The racetrack coils on the outer rhombic prism produce hexapole and decapole fields, and also allow for a limited dipole field for correction purposes. Figure 4.1.1 shows the layout of the various coils. The signs "+" and "-" indicate the direction of the current to produce a positive multipole term.

Due to symmetry in the design about the central axis, it is sufficient to describe only one quarter of the magnet. Figure 4.1.2 shows one quarter of the cross section. The positions and the direction of the coils in this quarter are specified in Table 4.1.1. All the coils have square cross section with thickness of 0.1 m.

In Table 4.1.1 the quantities $QI1, QI2, HI1, HI2, HI3, HI3$ are the magnitude of the currents. For any given configuration of the inner current coils, the currents
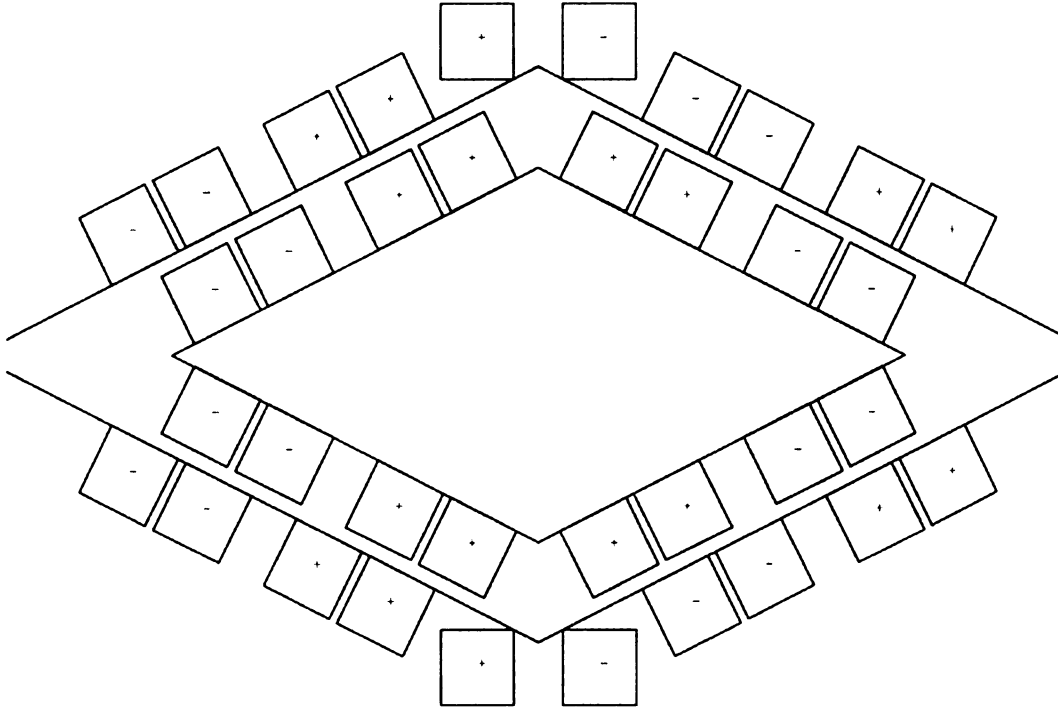
88

Figure 4.1.1. The cross section view of the quadrupole.

Coil Description	Position of Coils		Current
	x	y	
Inner Coils			
Quadrupole	0.4473	0.8222E-01	-QI1
Octupole	0.3473	0.1322	-QI2
Octupole	0.1973	0.2072	+QI2
Quadrupole	0.9736E-01	0.2572	+QI1
Outer Coils			
Hexapole	0.5591	0.1604	+HI1
Decapole	0.4591	0.2104	+HI2
Decapole	0.3091	0.2854	-HI2
Hexapole	0.2091	0.3354	-HI1
Dipole Corrector	0.8385E-01	0.4172	-HI3

Table 4.1.1. The center position of the current carrying coils in the first quadrant
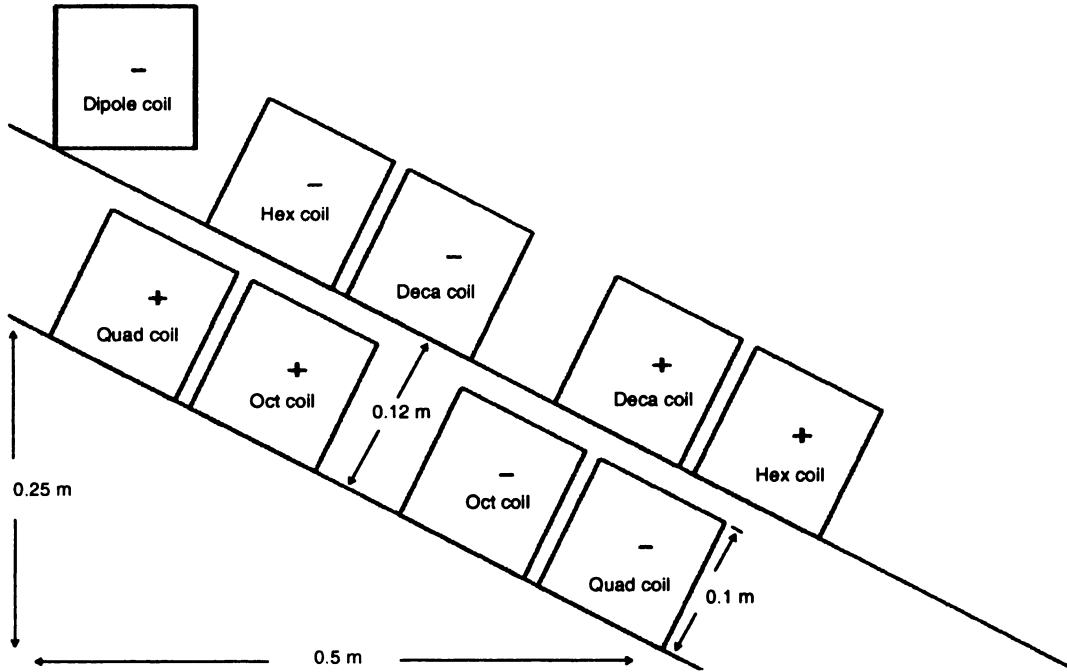
89

Figure 4.1.2. The layout of the racetrack coils in the first quadrant.

$(QI1, QI2)$ can be used as parameters to obtain different quadrupole and octupole strength. Similarly, for any given configuration of the outer coils, the currents $(HI1, HI2)$ can be used as parameters to get the desired hexapole and decapole field strength.

From the construction point of view it is cost efficient if the same type of coils can be used. We use current coils of the same shape and size to generate the quadrupole and hexapole fields. Also, we use the same type of current coils for octupole and decapole fields.

4.1.1 2D design of the quadrupole magnet

For a 2D design the current coils can be considered to be of infinite length, thus avoiding any fringe field effects. In this case a coil can be viewed as two current wires of infinite length and finite cross section which are separated by certain distance. The

currents in these wire are equal in magnitude but are opposite in direction.

The magnetic field of the magnet described in the previous section is a superposition of the fields produced by individual coils. In a 2D case the field of an individual coil is again a superposition of fields generated by two infinitely long current wires of finite cross sections . In the next section we show the results of the computation that has been performed using the infinite wire tool.

Pure quadrupole configuration

A pure quadrupole configuration can be achieved by the following setting of the currents.

```
QI1= 3965729.315790645   QI2= 80626.58244399808

HI1=  0.0000000000       HI2=  0.0000000000       HI3=  0.0000000000
```

The fifth order Taylor expansion of the magnetic field about the point $(0.0, 0.0, 0.0)$ that we obtained is shown in Table 4.1.2.

Pure hexapole configuration

A pure hexapole configuration can be achieved by the following setting of the currents.

```
QI1=  0.0000000000       QI2=  0.0000000000

HI1=  499792.9930948258 HI2=  938956.9619500297 HI3=  448723.7676402168
```

The fifth order Taylor expansion of the magnetic field about the point $(0.0, 0.0, 0.0)$ that we obtained is shown in Table 4.1.3.

```
MAGNETIC FIELD (Bx,By,BZ)
          Bx                    By                    Bz
  0.4440892098501E-15  0.000000000000     0.000000000000     000000
  0.000000000000      46.09565826333      0.000000000000     100000
 46.09565826333        0.000000000000     0.000000000000     010000
 -0.7105427357601E-14  0.000000000000     0.000000000000     200000
  0.1421085471520E-13 -0.1421085471520E-13 0.000000000000    110000
  0.000000000000       0.1136868377216E-12 0.000000000000    210000
  0.000000000000      -0.2842170943040E-13 0.000000000000    120000
  0.7815970093361E-12  0.000000000000     0.000000000000     030000
 -0.1421085471520E-13  0.000000000000     0.000000000000     400000
  0.000000000000       0.5684341886081E-13 0.000000000000    310000
 -0.2273736754432E-12 -0.1705302565824E-12 0.000000000000    130000
 -0.4263256414561E-13  0.5684341886081E-13 0.000000000000    040000
  0.000000000000      -3956.535097021     0.000000000000     500000
-19782.67548511        0.000000000000     0.000000000000     410000
  0.000000000000      39565.35097021      0.000000000000     320000
 39565.35097021        0.000000000000     0.000000000000     230000
  0.000000000000     -19782.67548511      0.000000000000     140000
 -3956.535097021       0.000000000000     0.000000000000     050000
------------------------------------------------------------------
```

Table 4.1.2. The fifth order Taylor expansion of the magnetic field about the point (0.0,0.0,0.0) for the current configuration producing a pure quadrupole field.

Operational plots

We have mentioned that the currents $(QI1, QI2, HI1, HI2)$ can be used as parameters to get the desired quadrupole and higher order multipole strength. However, there is a maximum limit on the current density that the superconducting coils can support. This puts a limit on the maximum quadrupole and other multipole field strength that can be achieved. Because of the fact that each multipole is achieved by superimposing the fields of several coils, this leads to operating diagrams showing achievable multipole settings.

To study this situation in detail, we now look at how the multipole strength depends on the currents. The matrix given in the equation (4.1.1) relates the multipole field

```
MAGNETIC FIELD (Bx,By,BZ)
```

Bx	By	Bz	
0.000000000000	-0.8604228440845E-15	0.000000000000	000000
-0.4718447854657E-15	0.000000000000	0.000000000000	100000
0.000000000000	-0.3885780586188E-15	0.000000000000	010000
0.000000000000	-18.24792017395	0.000000000000	200000
-36.49584034790	0.000000000000	0.000000000000	110000
0.000000000000	18.24792017395	0.000000000000	020000
-0.1776356839400E-14	0.000000000000	0.000000000000	210000
-0.1776356839400E-14	0.2664535259100E-14	0.000000000000	120000
0.2220446049250E-14	-0.4440892098501E-15	0.000000000000	030000
-0.1776356839400E-14	-0.3463895836830E-13	0.000000000000	400000
-0.2593480985524E-12	0.000000000000	0.000000000000	310000
0.000000000000	0.4547473508865E-12	0.000000000000	220000
0.1705302565824E-12	0.1953992523340E-13	0.000000000000	130000
0.4440892098501E-14	-0.4174438572591E-13	0.000000000000	040000
0.1776356839400E-14	0.8881784197001E-15	0.000000000000	500000
0.1421085471520E-13	0.1421085471520E-13	0.000000000000	410000
0.2842170943040E-13	0.3552713678801E-13	0.000000000000	320000
0.2131628207280E-13	0.000000000000	0.000000000000	230000
-0.5684341886081E-13	-0.7105427357601E-14	0.000000000000	140000
-0.4440892098501E-14	-0.3552713678801E-14	0.000000000000	050000

Table 4.1.3. The fifth order Taylor expansion of the magnetic field about the point (0.0,0.0,0.0) for the current configuration producing a pure hexapole field.

strength at the horizontal half aperture to the currents in the coils for the specific case of a horizontal half aperture of 0.5 m and a vertical half aperture of 0.25 m . In the notation $B^y_{(1111)}$, the superscript denotes the "y" component of the magnetic field and the subscript (1111) gives the exponent in transport notation. Thus, $B^y_{(1111)}$ is the coefficient of x^4 in the Taylor expansion of the "y" component of the magnetic field, or the decapole term in the expansion. The equations (4.1.2) provide relationships between the coefficients of other multipole terms in the Taylor expansion of the field to the principle multipole coefficients $B^y_{(11)}$, $B^y_{(111)}$ and $B^y_{(1111)}$.

$$\begin{bmatrix} B^y_0 \\ B^y_{(1)} \\ B^y_{(11)} \\ B^y_{(111)} \\ B^y_{(1111)} \end{bmatrix} = \begin{bmatrix} 0 & 0 & -0.25137 & -0.04316 & +0.37029 \\ +5.76974 & +2.40063 & 0 & 0 & 0 \\ 0 & 0 & -3.89914 & -2.08907 & -1.45431 \\ -0.40613 & +15.44685 & 0 & 0 & 0 \\ 0 & 0 & +1.66569 & -2.32478 & +2.99743 \end{bmatrix} \cdot \begin{bmatrix} QI1 \\ QI2 \\ HI1 \\ HI2 \\ HI3 \end{bmatrix}$$

$$(4.1.1)$$

$$B^y_{(22)} = -B^y_{(11)} \qquad\qquad (4.1.2)$$

$$B^y_{(122)} = -3B^y_{(111)}$$

$$-\frac{B^y_{(1122)}}{6} = B^y_{(2222)} = B^y_{(1111)}$$

$$B^x_{(2)} = B^y_{(1)}$$

$$B^x_{(12)} = 2B^y_{(11)}$$

$$\frac{B^x_{(112)}}{3} = -B^x_{(222)} = B^y_{(111)}$$

$$B^x_{(1112)} = -B^x_{(1222)} = 4B^y_{(1111)}$$

Operational plot for the quadrupole and the octupole fields

From the equation (4.1.1) it can be seen that the quadrupole field strength and the octupole field strength are coupled via the currents $(QI1, QI2)$. We vary both of these current densities in the range $\left[-10^8, 10^8\right]$ A/m^2 and plot the resulting octupole field strength and the quadrupole field strength; the results are shown in Figure 4.1.3. This plot gives the possible values of the quadrupole and octupole strength that can be achieved with the configuration of the coils described in the section 4.1.
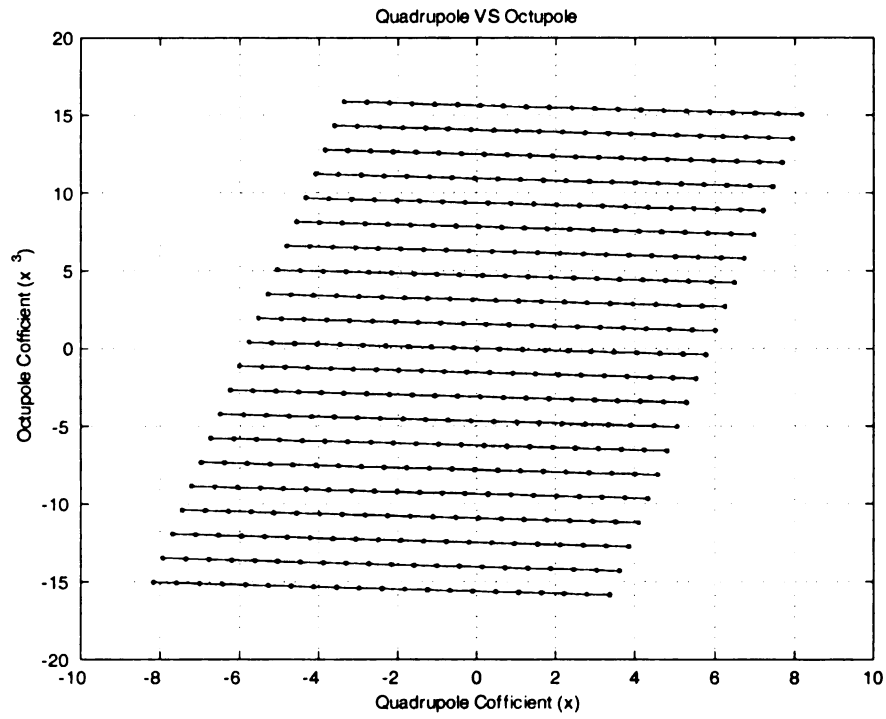
94

Figure 4.1.3. The operational plot for the quadrupole and the octupole. The coefficients are computed at the horizontal half aperture.
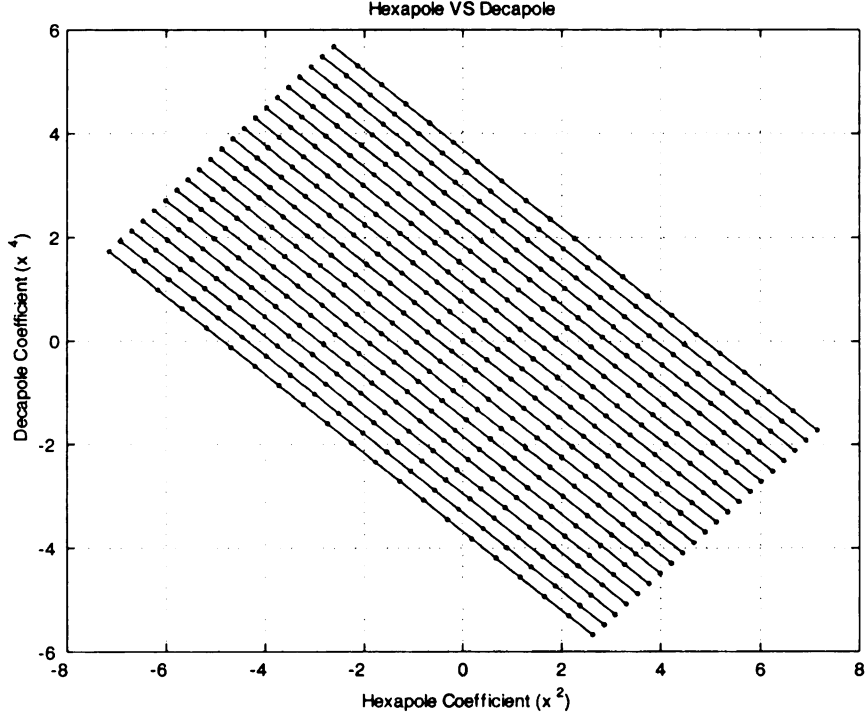
Figure 4.1.4. The operational plot for the hexapole and the decapole. The coefficients are computed at the horizontal half aperture.

Operational plot for the hexapole and decapole fields

From the equation (4.1.1) it can also be seen that the dipole, hexapole and decapole field strength are coupled via the currents $(HI1, HI2, HI3)$. However, under normal operation, we have a strict requirement of zero dipole field for this magnet. The dipole field is set zero by the proper choice of the current $HI3$. Once again we vary the current densities of all currents in the range $\left[-10^8, 10^8\right]$ A/m^2 and plot the decapole field strength versus the hexapole field strength; the results are shown in Figure 4.1.4. This plot gives the possible values of the hexapole and decapole strength that can be achieved with the configuration of the coils described in the section 4.1.
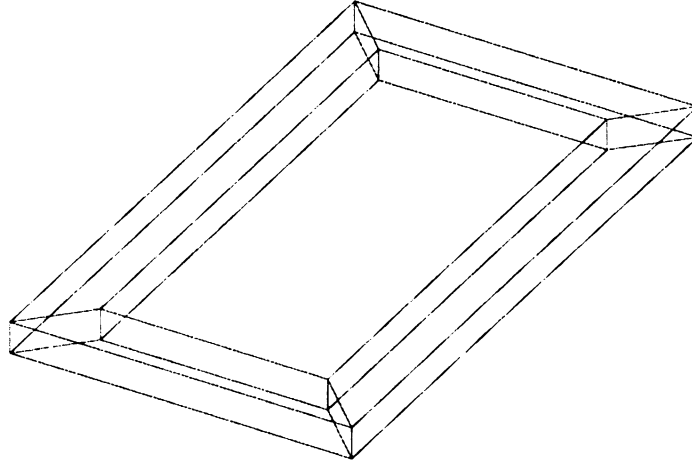
Figure 4.1.5. The schematic digram of a current coil.

Optimization of the operational region

The matrix given in the equation (4.1.1) is influenced by the geometrical design parameters of the system. In order to optimize the operational region of the currents and the fields, we need to find the optimal geometric configuration of the coils described in the section 4.1, where the optimal design is defined as the one that would decouple the influence of the octupole coil current on the quadrupole component of the field and vice versa. And, at the same time maximize the coupling strength of the current in quadrupole coils on the quadrupole component of the field, and maximize the coupling strength of the current in octupole coils on the octupole component of the field. The same type of optimization is also required for the hexapole and decapole components of the field.

4.1.2 3D design of the quadrupole and the fringe field analysis

Figure 4.1.5 shows a current coil of a rectangular cross section . This coil is made by joining four wires having rectangular cross section with the current entrance and exit

planes tilted by 45° in opposite directions. This ensures that there is a continuos flow of current through the coil. The magnetic field for each of these wires is calculated using the COSY tools described in the section 3.4.4.
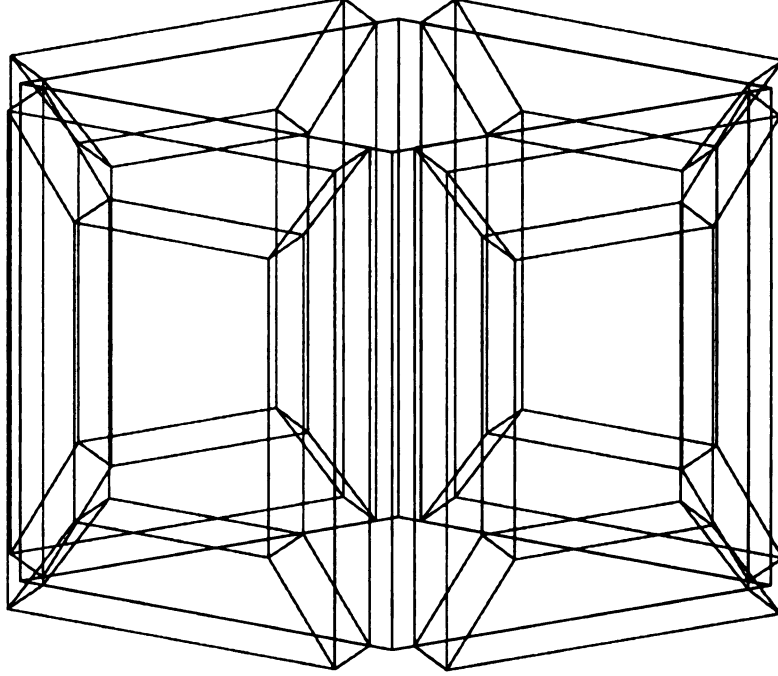

Figure 4.1.6. The three dimensional layout of quadrupole coils.

The 3D layout of the quadrupole with four current coils is shown in Figure 4.1.6. We note that when the length of the magnet is large compared to the aperture of the magnet, the magnetic field at the center of the magnet is identical to the magnetic field obtained by the 2D design in the section 4.1.1. We also verify that the curl and the divergence vanishes at all points inside the magnet.

To present the results we once again consider the design presented in the section 4.1.1, but with a modification that the length of the magnet is finite. We consider a magnet of length $1\ m$, extending from $-0.5\ m \leq z \leq 0.5\ m$. We now look at the magnetic field generated by this coil configuration at four different planes perpendicular

to the central axis, $z = 0$, $z = 0.25\ m$, $z = 0.5\ m$ and $z = 1.0\ m$.

From figures 4.1.7 and 4.1.8 we can see that at the plane $z = 0$ the magnetic field agrees with the textbook model where $B_x = Cy$, $B_y = Cx$. In the z direction the magnitude of the magnetic field is of the order $\sim 10^{-16}$, which is zero for all practical purposes.

Now, as we start going away from the center, we start seeing deviation from the ideal behavior ($z = 0$). Figures 4.1.9 and 4.1.10 show the plots for the magnetic field at the quarter length of the magnet, $z = 0.25\ m$. There is no significant deviation from ideal behavior in the x and y components of the magnetic field. In the z direction we notice that the magnetic field is nonzero. However, the magnitude is still very small compared to the components B_x and B_y.

Figures 4.1.11 and 4.1.12 show the plots for the magnetic field at the entrance and the exit of the magnet, for $z = 0.5\ m$. Now we see that the magnetic field is different compared to the field at the center of the magnet. We see that the strength of B_x and B_y falls by a factor of five. The B_z component is very strong, which is almost three times as large as B_x or B_y.

Figures 4.1.13 and 4.1.14 show the magnetic field on a plane $0.5\ m$ away from the entrance and exit of the magnet. The overall field falls off significantly and its magnitude is $\sim 10^{-1}$ *tesla*. Finally, the plot 4.1.15 shows the magnetic field on the first quadrant of the magnet on the $y = 0\ m$ plane. The region stretches from the center of the magnet to $0.5m$ (half length of the magnet) outside the magnet in both x and z directions. Here the fringe field that falls off in the region can be clearly seen.
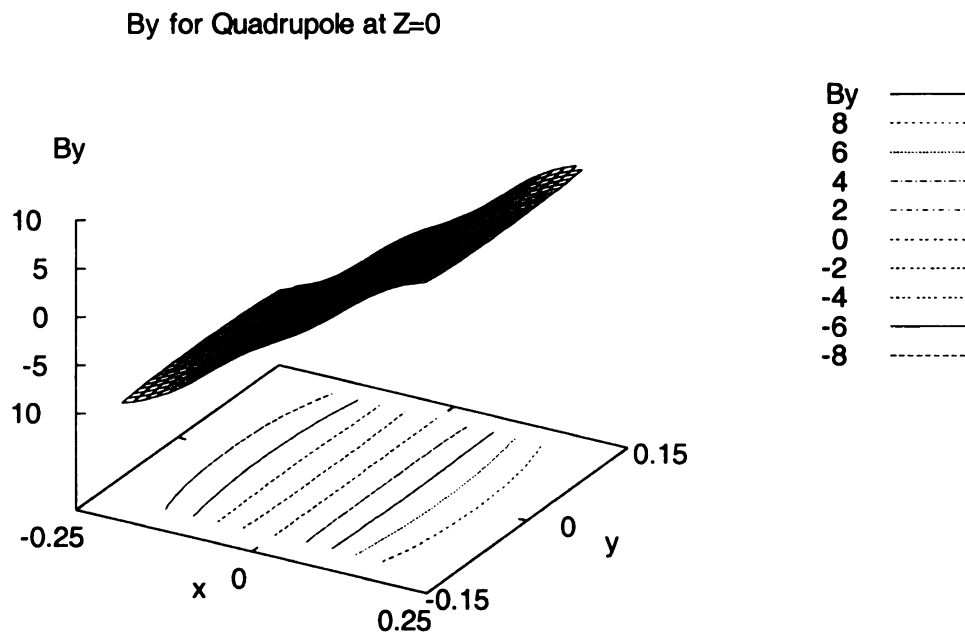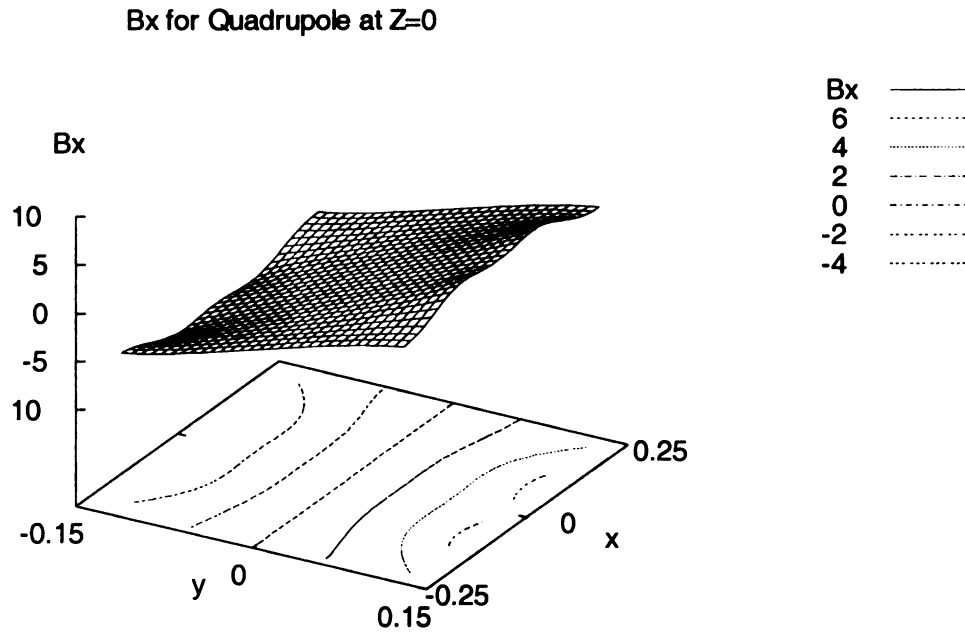
Bx for Quadrupole at Z=0

Bx

Bx
6
4
2
0
-2
-4

10
5
0
-5
10

0.25
0

x

-0.15

y   0

0.15   -0.25

(a)

By for Quadrupole at Z=0

By

By
8
6
4
2
0
-2
-4
-6
-8

10
5
0
-5
10

0.15
0

y

-0.25

x   0

0.25   -0.15

(b)

Figure 4.1.7. (a) The plot for B_x for the data on the plane $z = 0$ m. (b) The plot for B_y for the data on the plane $z = 0$ m.

100

Bz for Quadrupole at Z=0
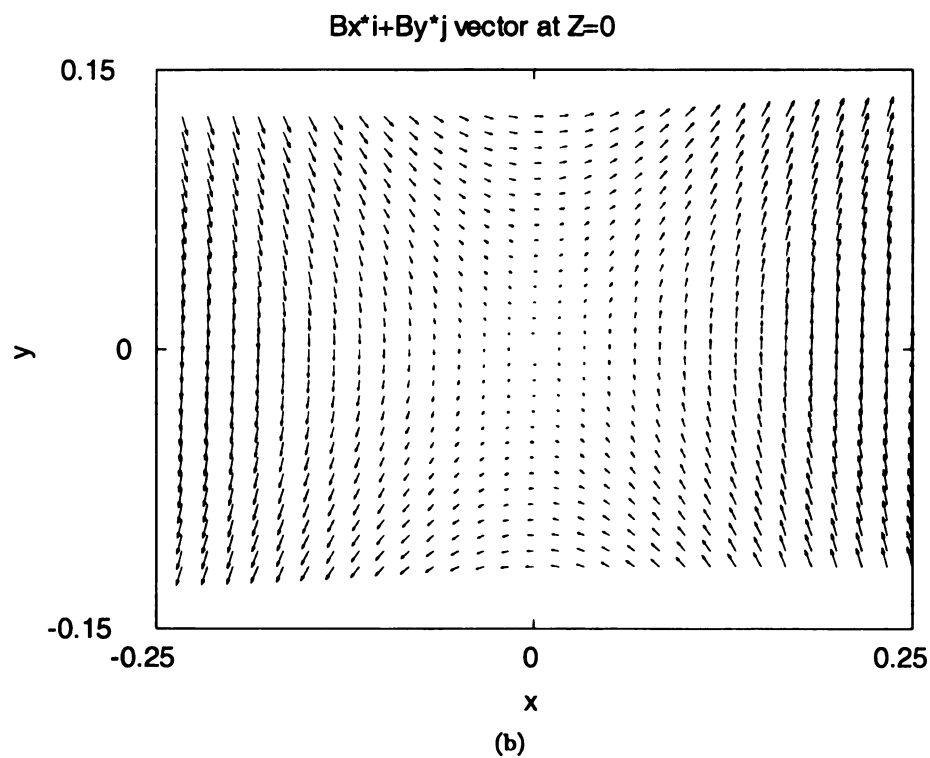
Bx*i+By*j vector at Z=0

Figure 4.1.8. (a) The plot for B_z for the data on the plane $z = 0$ m. (b) The vector plot of the two dimensional field on the plane $z = 0$ m.

Bx for Quadrupole at Z=.25

(a)

By for Quadrupole at Z=.25

(b)

Figure 4.1.9. (a) The plot for B_x for the data on the plane $z = 0.25 \ m$. (b) The plot for B_y for the data on the plane $z = 0.25 \ m$.
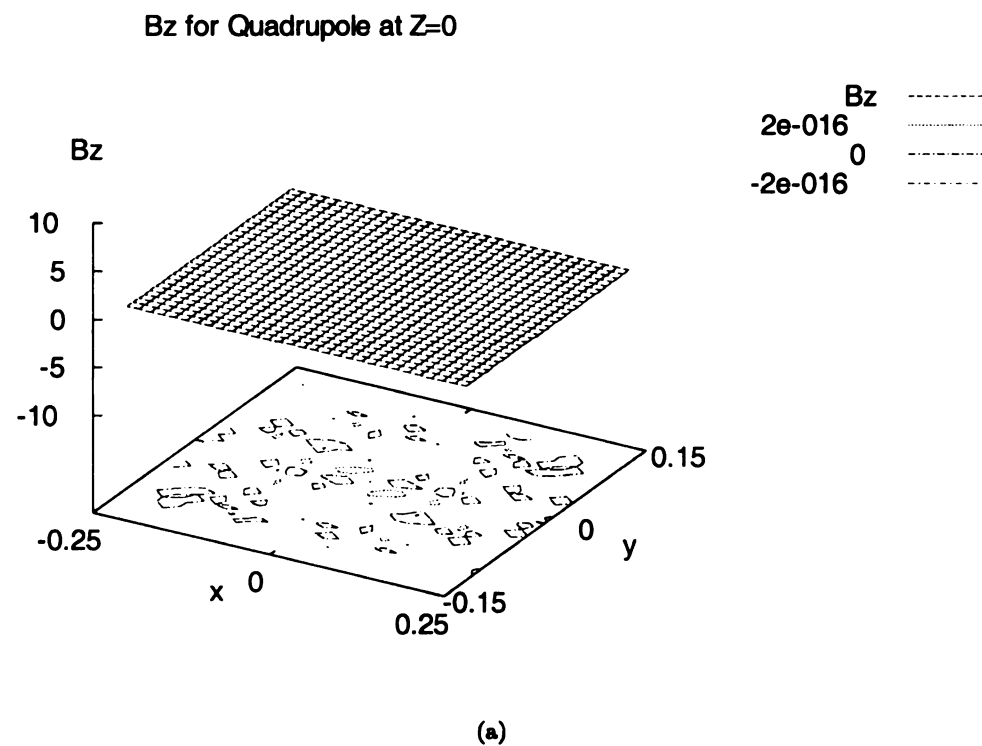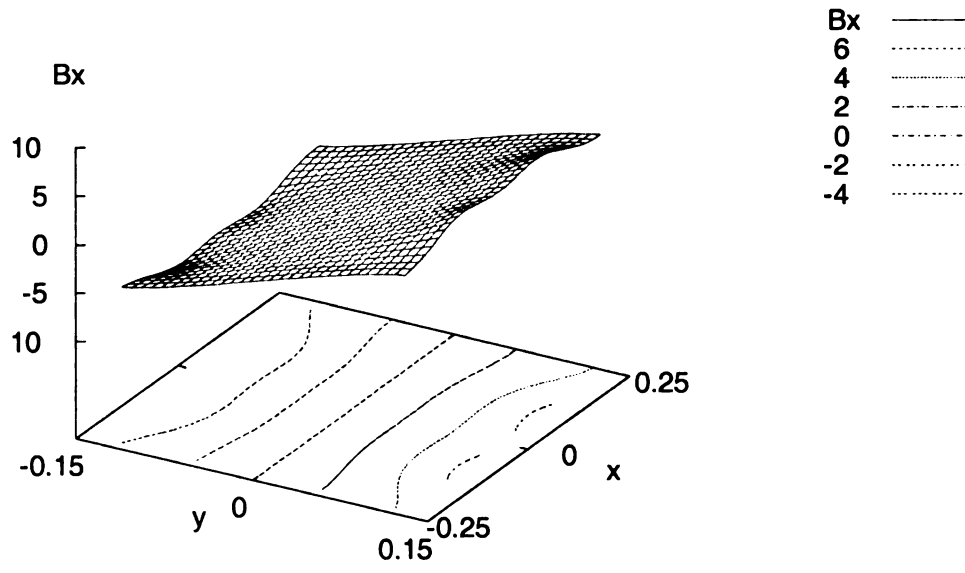
Figure 4.1.10. (a) The plot for B_z for the data on the plane $z = 0.25$ m. (b) The vector plot of the two dimensional field on the plane $z = 0.25$ m.

Bx for Quadrupole at Z=0.5

(a)

By for Quadrupole at Z=0.5

(b)
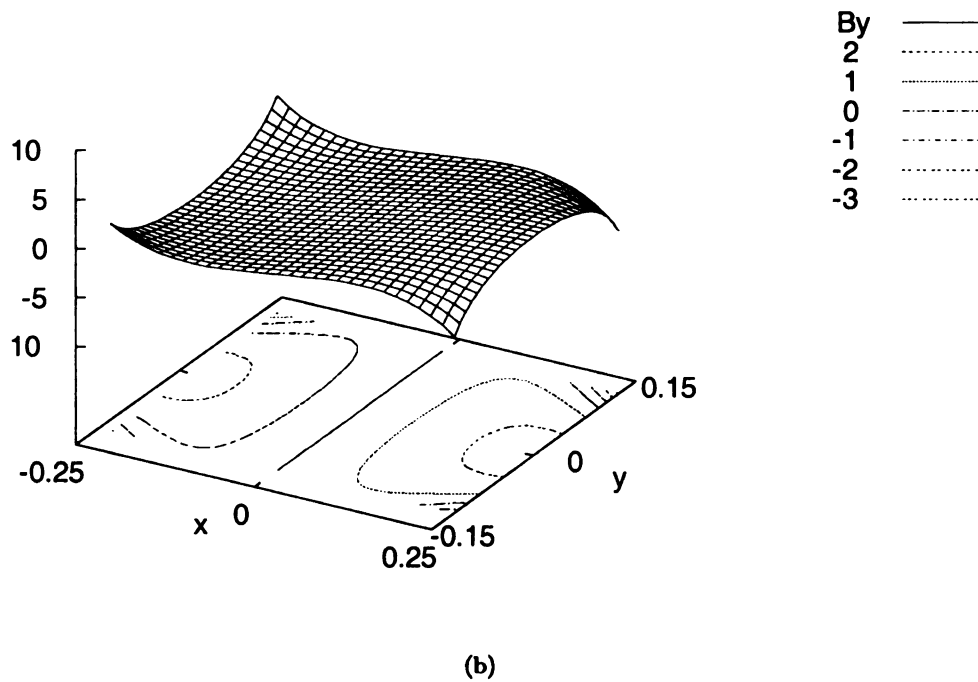
Figure 4.1.11. (a) The plot for B_x for the data on the plane $z = 0.5$ m. (b) The plot for B_y for the data on the plane $z = 0.5$ m.
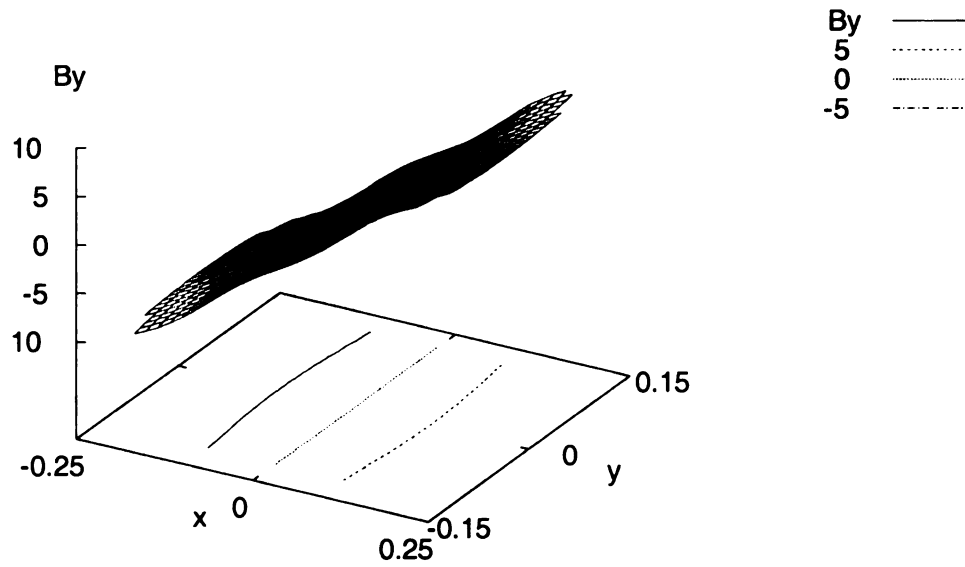
104

Bz for Quadrupole at Z=0.5

Bx*i+By*j vector at Z=0.5

Figure 4.1.12. (a) The plot for B_z for the data on the plane $z = 0.5\ m$. (b) The vector plot of the two dimensional field on the plane $z = 0.5\ m$.

105

Bx for Quadrupole at Z=1

(a)

By for Quadrupole at Z=1

(b)
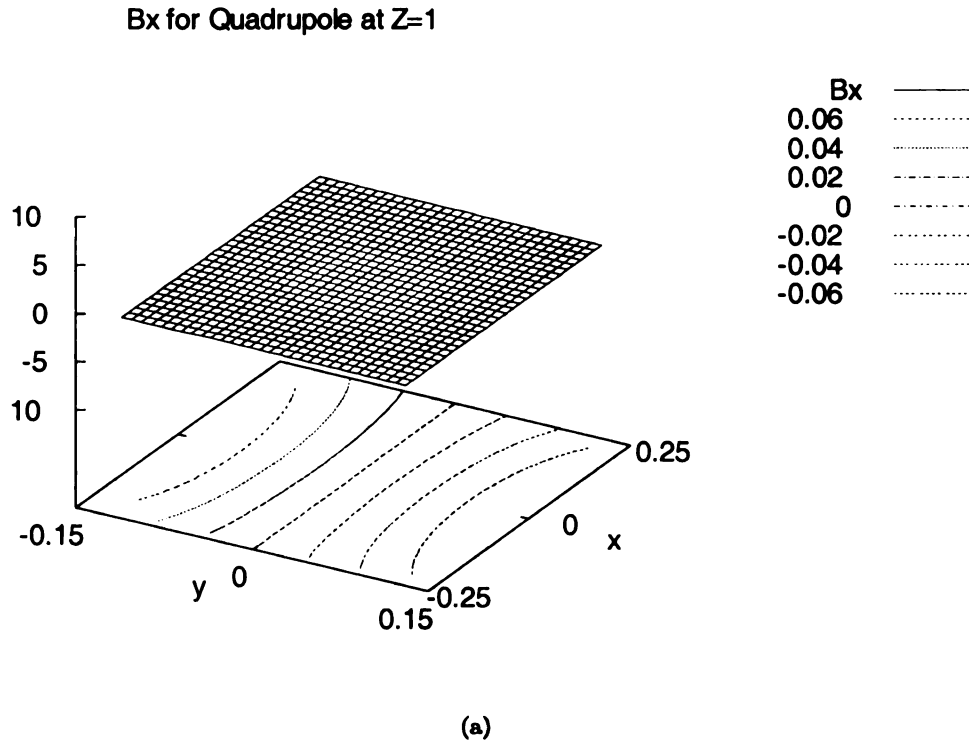
Figure 4.1.13. (a) The plot for B_x for the data on the plane $z = 1\ m$. (b) The plot for B_y for the data on the plane $z = 1\ m$.

106

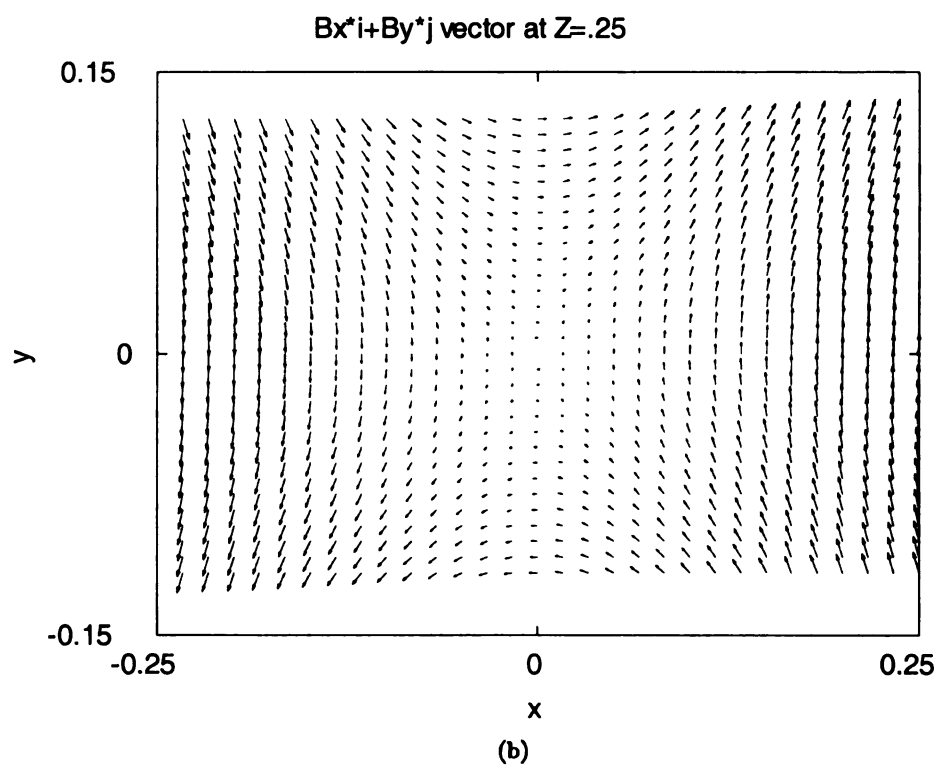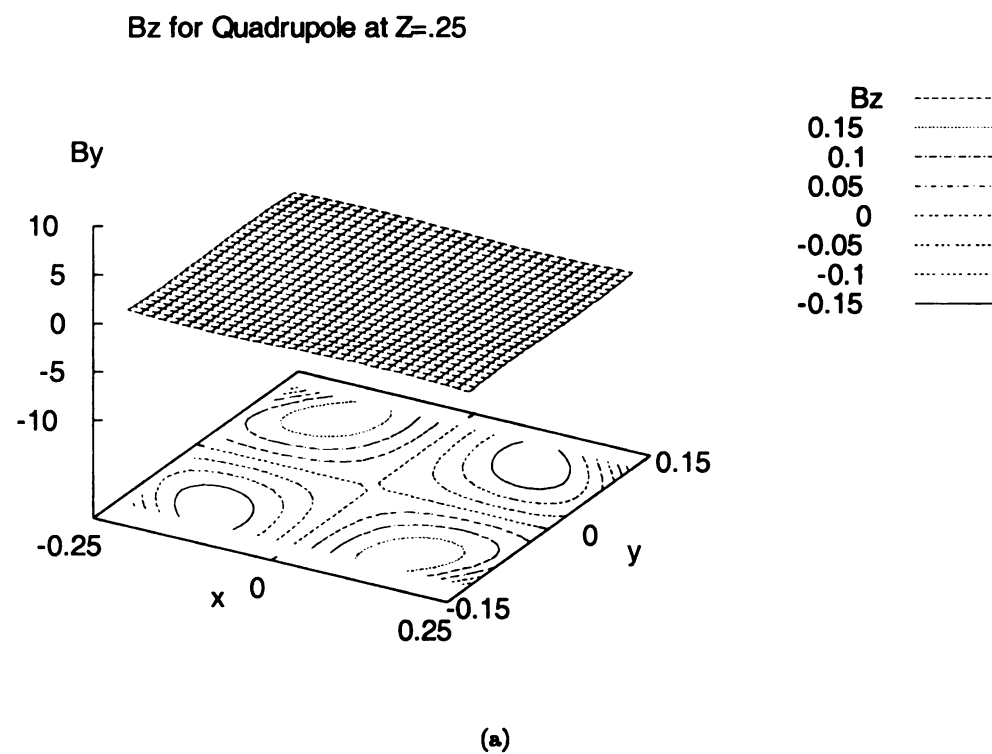## Bz for Quadrupole at Z=1

(a)

Bx*i+By*j vector at Z=1

(b)
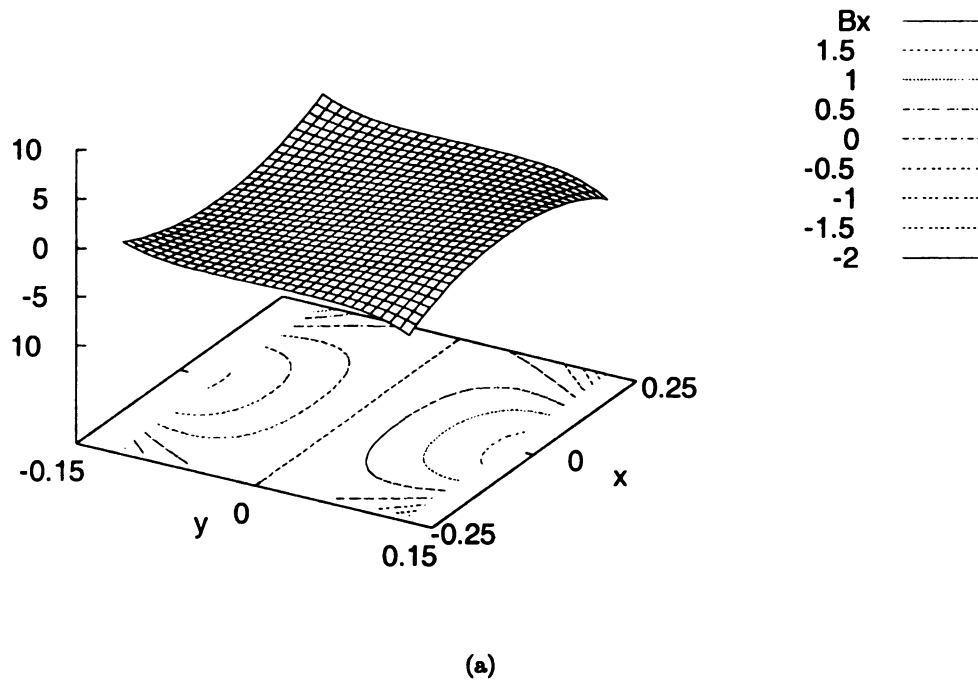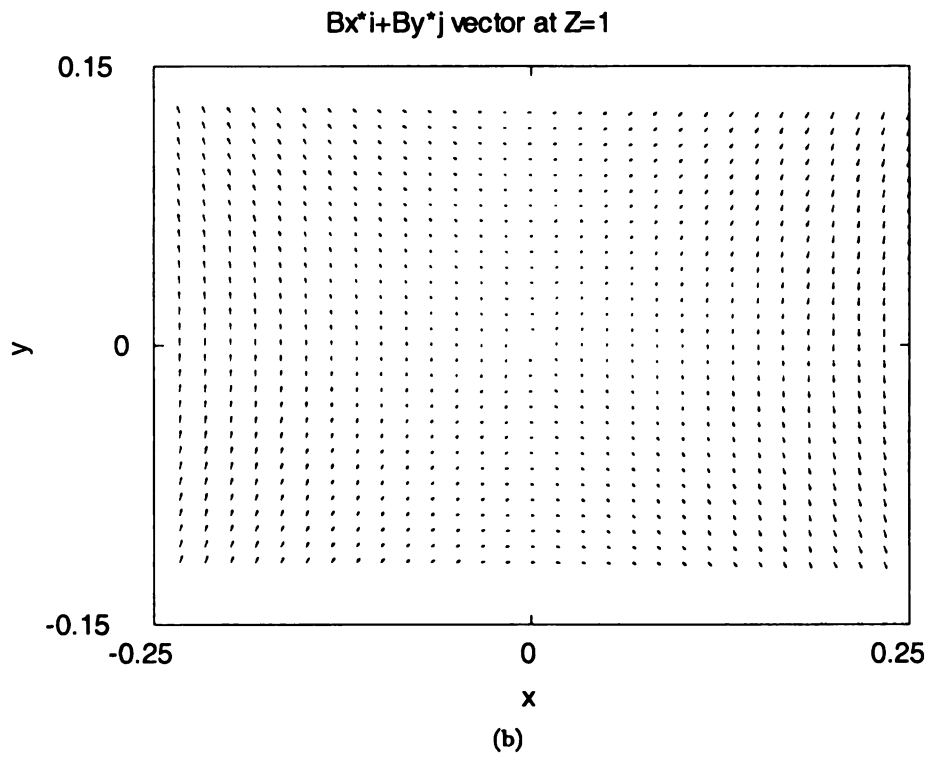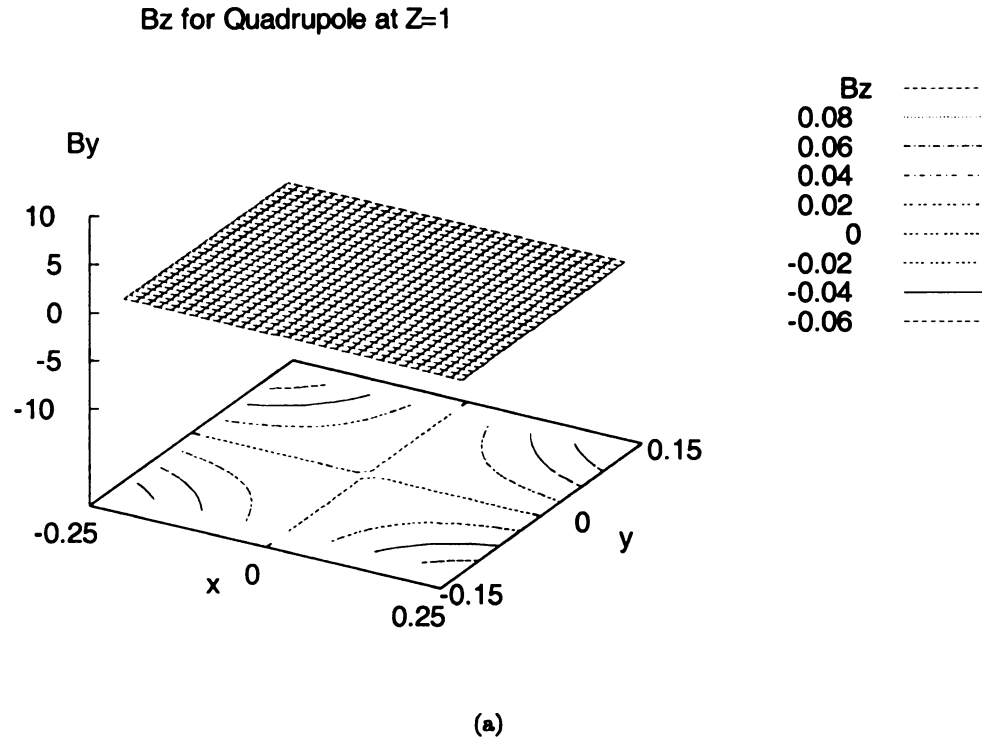
Figure 4.1.14. (a) The plot for B_z for the data on the plane $z = 1$ m. (b) The vector plot of the two dimensional field on the plane $z = 1$ m.

107

By for Quadrupole at Y=0 plane

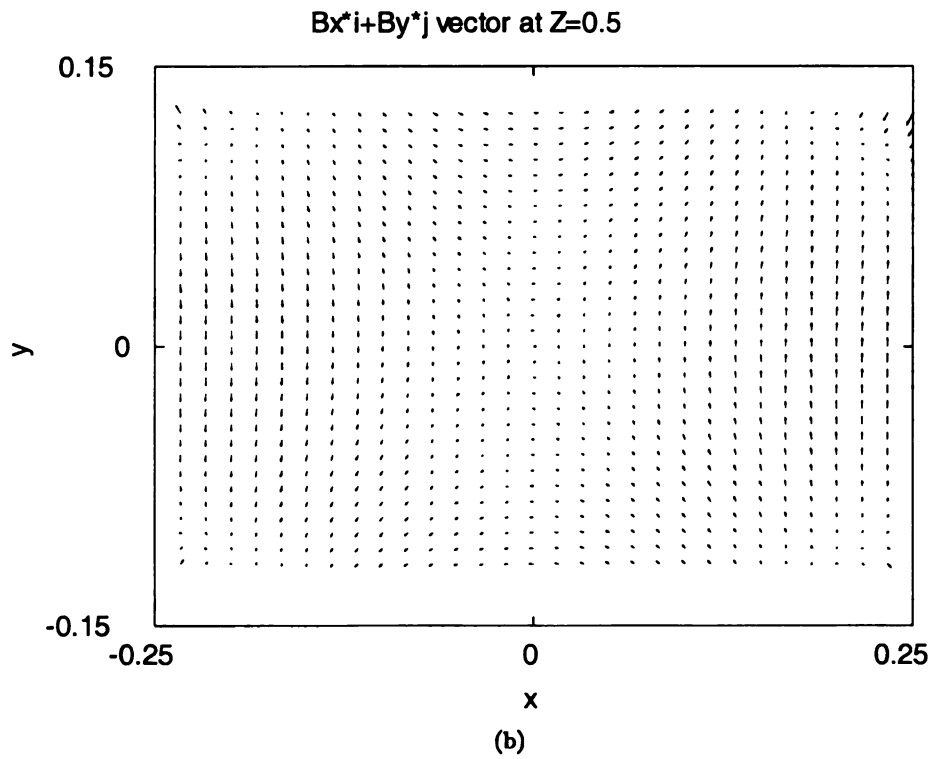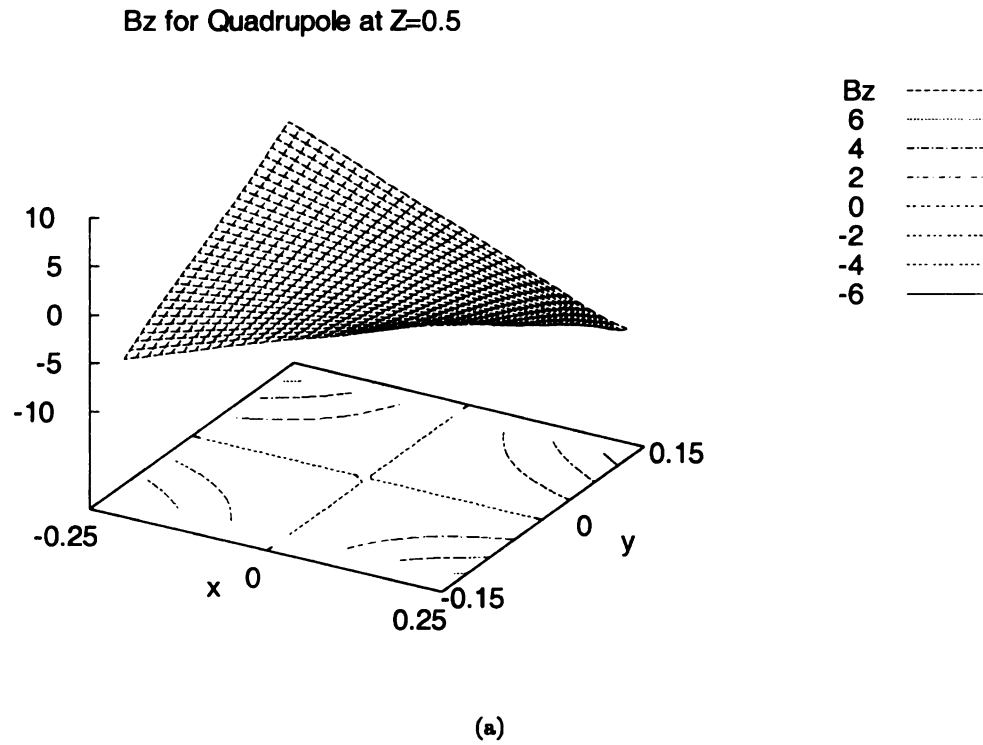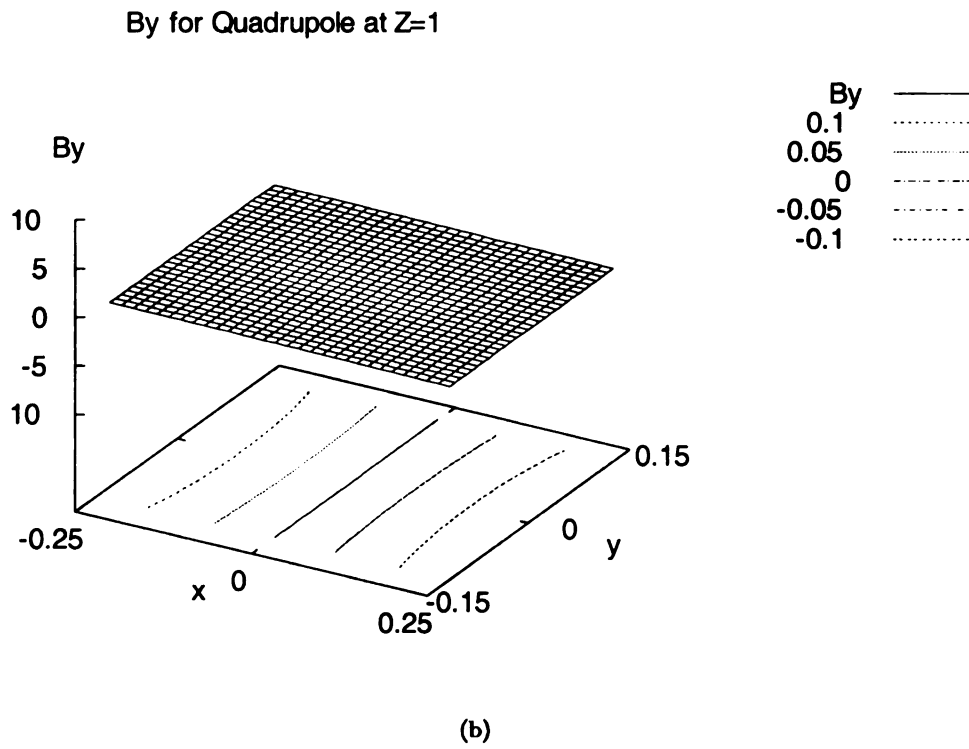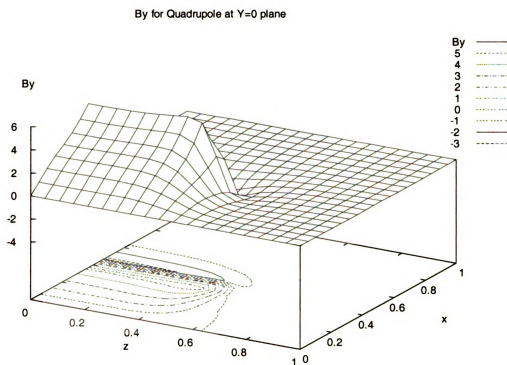Figure 4.1.15. The plot of the magnetic field on the midplane, $y = 0$ m. Only the magnetic field in the first quadrant is shown.
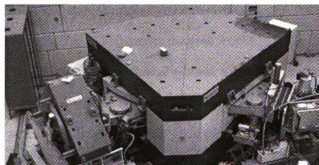
Figure 4.2.1. The dipole magnet of the MAGNEX spectrometer.
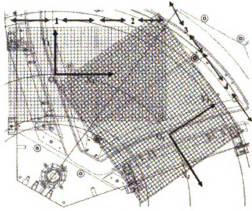
Figure 4.2.2. The layout of the measurement grids in different regions of the dipole magnet.

4.2 The dipole magnet of the Catania MAGNEX spectrometer

We now address a practical application of the Laplace solver technique to magnetic spectrometers. The trajectory reconstruction method [21] is one of the important tools to study magnetic spectrometers. Good computational modelling of the dipole magnet is very important for this tool to work, and this is particularly so for modern large-aperture devices such as MAGNEX at INFN, Catania, Italy [70, 49, 29]. Figure 4.2.1 shows the MAGNEX spectrometer configuration.

For purposes of measurement economy, magnet builders usually provide the magnetic field only on few separate horizontal planes within the dipole, while the computational treatment of the device requires the knowledge of the field in all of space. The MAGNEX dipole was divided into a number of volumes defined by areas and planes as shown in Figure 4.2.2. Four areas were mapped as indicated in Table 4.2.1; Areas 1 and 4 comprise the Effective Field Boundary regions of the magnet at the entrance and at the exit where the field undergoes a sudden variation due to the

fringe field effects, whereas region 2 and 3 represent the central region of the magnet. This subdivision is the result of the need of different grid sizes over the mapped area in order to limit the measurement time. For each of the regions the measurements were taken on seven different planes as shown in Table 4.2.1.

Area	
1	EFB area at entrance
2	Central area entrance end
3	Central area exit end
4	EFB area at exit

Planes	Z(cm)	
a	0	Midplane
b	1.6	Above midplane
c	3.2	Above midplane
d	4.8	Above midplane
e	6.4	Above midplane
f	8.0	Above midplane
g	-4.8	Below midplane

Table 4.2.1. (a)Areas mapped in the dipole (b)Planes mapped in the dipole.

The magnetic measurement were organized so that the RMS error $\langle \Delta B_i/B \rangle$ $i = x, y, z$ at any mesh point inside the working volume of the magnet was not greater than 5×10^{-4}. The field measurement error due to the error of measuring the Hall probe voltage was $\Delta B = \pm 5 \times 10^{-5}$ Gauss. The main source of the B measurement error were assumed to be the errors of positioning the Hall probe [71, 65, 41].

Utilizing that sufficiently outside the dipole the fields will vanish, it is thus possible to provide field data over the surface of a finite box enclosing the region of interest, and thus to apply the Laplace solver technique to obtain a field representation everywhere. We use this method to compute the fields in the region 1 and plane A of the dipole magnet. The contour plot of the resulting relative errors is plotted over the region 1 in Figure 4.2.3. The region where the sharp valley is observed coincides with the physical boundary of the dipole magnet.

Figure 4.2.3 we can see that the relative error is not as small as we would expect from our approach. Since the data was measured in several planes and in several overlapping regions on each plane it is very hard to extract the magnetic field data on a closed surface. To demonstrate our approach we have used only the data for the entrance of the dipole magnet (region 1) and extracted data on a surface of a

110
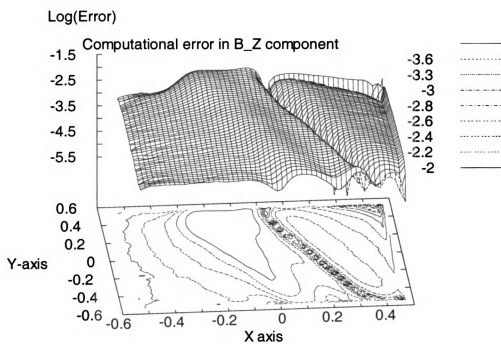
Figure 4.2.3. The contour plot of magnetic field errors for the region 1 and plane A.
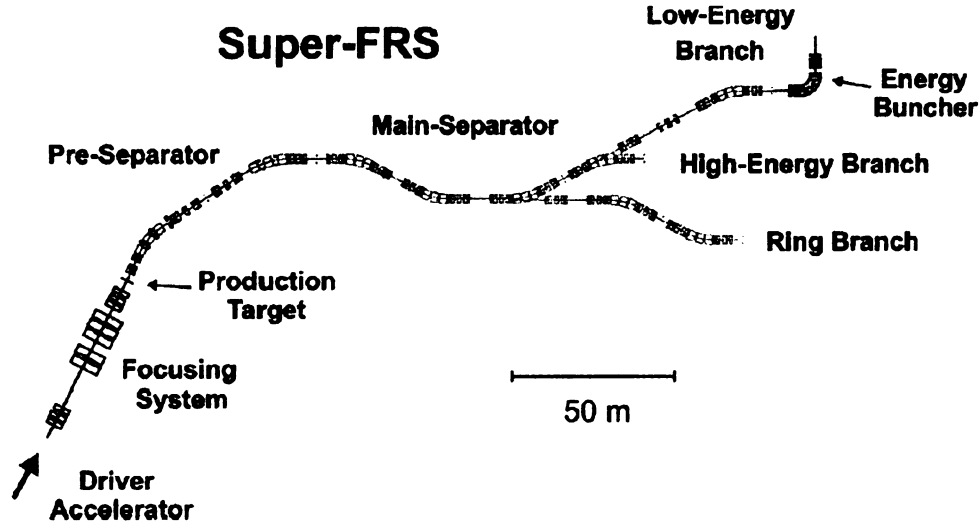
Figure 4.3.1. The layout of the Super-FRS. Spatially separated rare-isotope beams are delivered to the experimental areas via three different branches.

rectangular box enclosing the region of interest. Since the data was measured on only seven different planes the data on two surfaces, $x = \pm 0.5$ m, of the rectangular box enclosing the region of interest are discretized with very large step size. This may lead to large errors from the surface elements on these planes ($x = \pm 0.5$ m). Also, compared to the case where the whole data is enclosed by one closed surface the smoothing effect is limited for the rectangular box enclosing only the data on region 1 for seven different planes. The difference we observe may also be attributed to the errors in the experimental measurements and may need independent verification.

4.3 Ion-optic simulations for the Super-FRS

The superconducting fragment separator (Super-FRS) [38] being built at GSI, Germany will be the most powerful in-flight separator for exotic nuclei up to relativistic energies. The Super-FRS is a large-acceptance superconducting fragment separator with three branches serving different experimental areas. The Super-FRS uses the

Parameters	
Max. Magnetic Rigidity $B\rho_{max}$	$20Tm$
Momentum Acceptance $\Delta P/P$	$\pm 2.5\%$
Angular Acceptance $\phi_y\phi_x$	$\pm 40 mrad^2$
Momentum Resolution	1500

Table 4.3.1. The Super-FRS design parameters.

$B\rho - \Delta\rho - B\rho$ method, where a two-fold magnetic rigidity analysis is applied in front of and behind a specially shaped energy degrader. As a consequence the Super-FRS consists of a two-stage magnetic system, the pre-separator and the main-separator, each equipped with a degrader. Figure 4.3.1 shows the layout of the proposed Super-FRS. Table 4.3.1 summarizes the design parameters for the Super-FRS.

The ion-optic design for the Super-FRS has been primarily studied using the beam physics code GICOSY [19]. The code GICOSY computes the transfer maps to the fifth order. However, for some electric and magnetic elements the GICOSY code computes transfer maps to only the third order, and hence the maps generated are only correct to the third order. The first, second and third order design studies have been conducted using the code GICOSY. However, for high acceptance and high resolution machines like the Super-FRS, the high order transfer map computations are necessary to study the effect of the high order nonlinearities on the resolution achieved. The code COSY INFINITY [23, 24] is an arbitrary order beam physics code and hence can be utilized to perform the high order design studies of the Super-FRS.

The theory and the implementation details of the GICOSY and the COSY INFINITY codes can be found in [77, 78, 26, 79, 20, 15, 14, 16, 25, 52, 13, 7, 8, 12] and references therein. Both GICOSY and COSY INFINITY codes are written in the Fortran 77 language, and they themselves provide a programming environment to describe a particle optical system conveniently and in an intuitive manner. However, due to the differences in their approach to the description of the optics, and their implementation in the Fortran 77 language, they may provide different results for

113

some of the ion or particle optical elements. Though they may be very small, these differences may be of relevance, for example, when analyzing instruments of high precision, like fragment separators, where the higher order aberration corrections are important to get the desired resolution. A systematic study of the differences in the description of the important particle optical elements in the GICOSY and the COSY INFINITY codes has been done and the results are presented in the Appendix A. Also, to facilitate code reusability, a code converter to translate a GICOSY program into the COSY INFINITY program has been developed and is discussed in Appendix B. Using this program, all GICOSY files were converted to COSY INFINITY files to perform the high order simulations. It has been verified that with same choice of units and the scaling factor and ignoring the fringe fields, the results from the COSY INFINITY and GICOSY codes agreed to good accuracy to third order.

The code COSY INFINITY has been optimized to do single particle simulations for large multiturn accelerators like the LHC and the FNAL. There is a plethora of tools available in the code COSY INFINITY to study and present results for these multiturn accelerators. However, to present the results for an ensemble of particles for a single pass accelerator like the Super-FRS, we need to implement new output tools. New tools developed for the purpose are discussed in Appendix C.

We now present the results of the simulation for the pre-separator stage, the main-separator stage and the energy buncher using the code COSY INFINITY. We then apply the Laplace solver technique to the magnetic field data obtained from the TOSCA simulation of the Super-FRS quadrupole and extract the transfer map for this magnet.

4.3.1 The pre-separator branch

The standard ion-optical layout of the pre-separator stage is presented in Figure 4.3.2a. The most relevant first order matrix elements are given in Table 4.3.2 at four

114

Matrix Element	PF1	PF2	PF3	PF4
$(x|x)$	-3.19	1.73	-3.19	2.00
$(x|a)$	0	0	0	0
$(x|\delta)$	3.68	-2.00	3.68	0
$(a|a)$	-0.31	0.57	-0.31	0.50
$(a|\delta)$	0.44	0	-0.44	0
$(y|y)$	-4.81	-3.13	0.39	2.28
$(y|b)$	2.13	0	-1.94	0
$(b|b)$	-0.07	-0.32	-0.02	0.43

Table 4.3.2. The relevant first order matrix elements for the pre-separator stage.

focal planes PF1, PF2, PF3, and PF4. In the first focal plane a focus is realized only in the x direction, whereas in the symmetrical mid plane, the position of the first degrader system, foci are required in both the x and y coordinates. Also a parallel dispersion line is required at PF2. The system is mirror symmetric with respect to PF2, firstly to have the necessary three foci to achieve the achromatic condition at PF4, secondly to minimize the geometrical image aberrations. Figure 4.3.3 shows the envelopes and the dispersion line for the primary-beam emittances of 40π mm mrad and $\Delta p/p$ of 2.5 % . The target spot size is assumed to be ± 1 mm and ± 2 mm in the x and y directions, respectively.

The benefit of the design is that the higher order aberrations are small except for the chromatic contributions, especially $(x, a\delta)$ which is responsible for an enormous focal plane tilt. The tilt angle at PF2 would be about 7 degrees without second-order corrections by means of hexapole magnets, while the required tilt is 90 degrees. Such a tilt would make a high resolution degrader operation very difficult or even impossible. Therefore, hexapole magnets are used to correct this deficiency. However, as soon as this correction is done, induced higher order aberrations become a major challenge. Applying hexapole and octupole corrections, about 80 % of the first-order momentum resolving power at the central plane of the pre-separator was regained.

Usually, the resolution is computed using formulas which only consider the important aberration terms. However, we can also compute the true nonlinear resolution
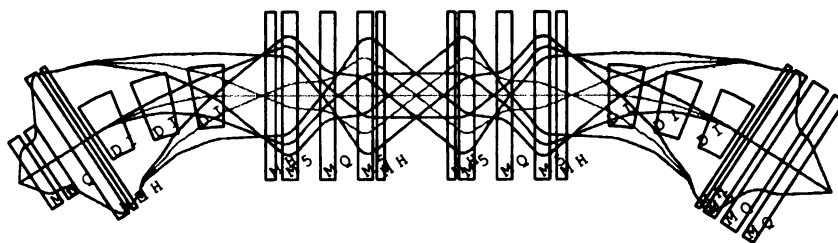
(a) Layout of the Pre-Separator

0.3 8
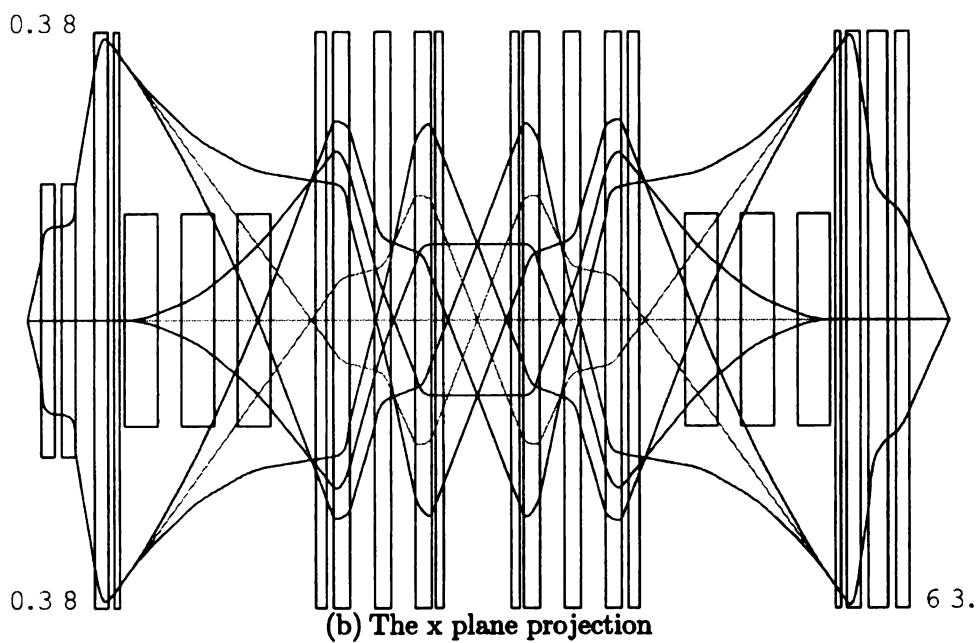
0.3 8   6 3.
(b) The x plane projection

0.3 8
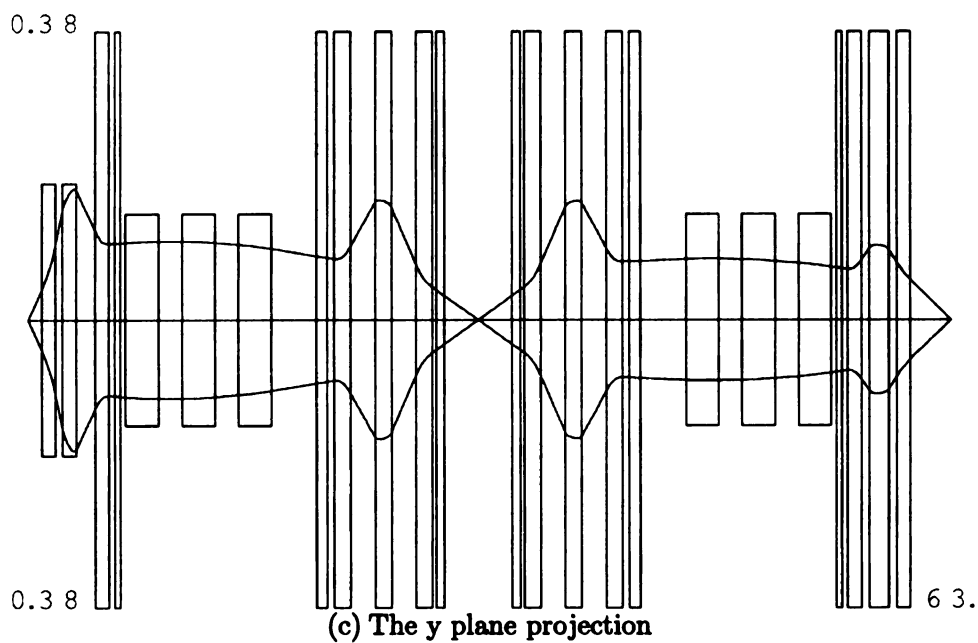
0.3 8   6 3.
(c) The y plane projection

Figure 4.3.2. The figure shows the pre-separator layout and the projections of the trajectories into the x and y planes.

116
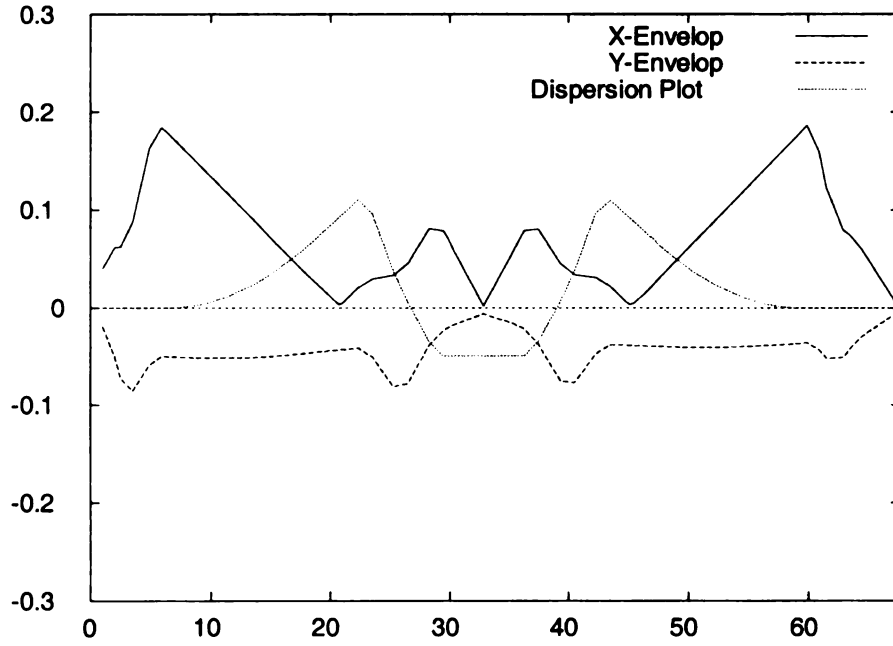
Figure 4.3.3. Envelopes and the dispersion line for the pre-separator stage.

Order	Non-linear resolution
1	785
2	760
3	645
4	647
5	645
6	655
7	660

Table 4.3.3. The Non-linear resolution at the focus PF2.

by launching N particles, uniformly distributed in the phase space, and compute the spot size of the resulting beam distribution. The nonlinear resolution computed using this is a good measure of the overall nonlinear effects. Table 4.3.3 shows the nonlinear resolution achieved at the focus PF2 by changing the order of computation. The strength of sextupoles and octupoles were fitted to maximize the resolution while satisfying other necessary conditions. We see that the resolution does not drop significantly with the increase in the order of computation. In the pre-separator stage the required resolution can thus be achieved with the current lattice settings.

Order	Non-linear resolution
1	1602
2	1582
3	862
4	519
5	484
6	645
7	439

Table 4.3.4. The Non-linear resolution at the focus MF2.

4.3.2 The main-separator

The main-separator consists of 4 dipole stages with focusing elements in front of and behind each dipole magnet system. The main-separator also has 4 focal planes, MF1, MF2, MF3 and MF4 to accommodate an achromatic system with a degrader station in the central focal plane MF2.

An analysis similar to the pre-separator stage is performed for the main-separator stage. Table 4.3.4 shows the non-linear resolution achieved at the focus MF2 by changing the order of computation. Once again the strength of sextupoles and octupoles were fitted to maximize the resolution while satisfying other necessary conditions. For the main-separator stage the resolution changes significantly with change of order of computation. The main-separator stage may require further analysis to correct for high order aberrations.

4.3.3 The energy buncher

After production and in-flight separation in the pre-separator and the main separator stages of the Super-FRS, the secondary beam can be distributed to either of three experimental areas: a high-energy cave, a storage ring complex and a dedicated low-energy branch (LEB), as shown in Figure 4.3.1. In the LEB the exotic species can be slowed-down to ion energies ranging from a few hundred MeV/u down to rest. The LEB is equipped with an energy-bunching stage in order to reduce the energy spread of the secondary ions originating from the fragment production process and from
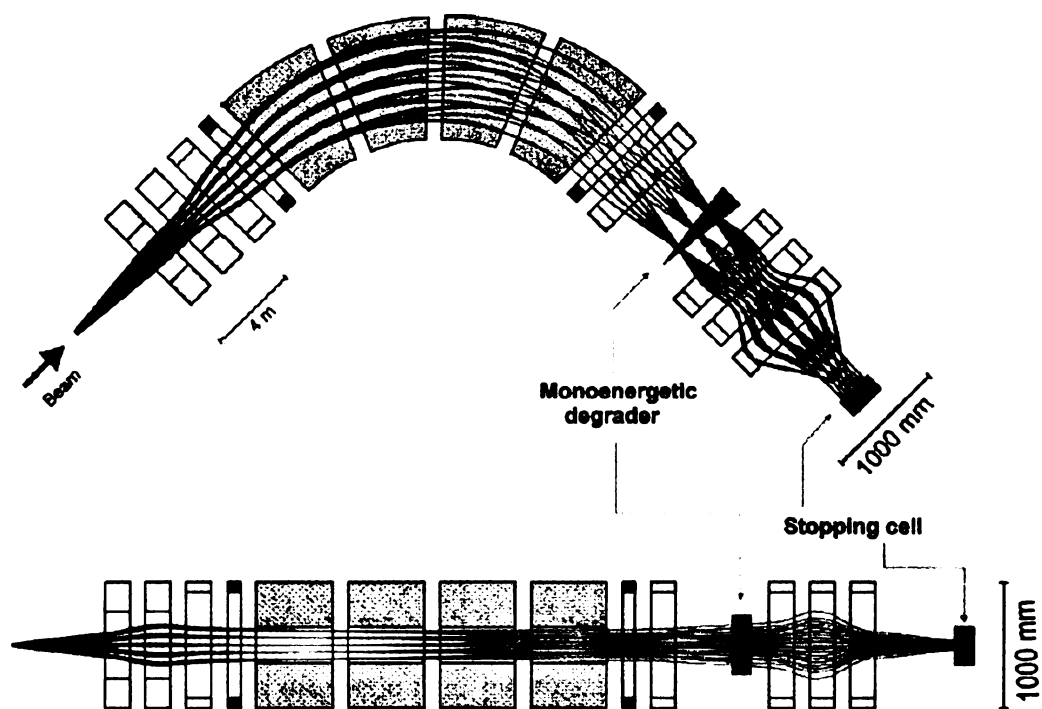
Figure 4.3.4. Ion-optical layout of the energy buncher.

119

straggling in the target and the degraders. For the energy buncher the simulations were performed using the code COSY INFINITY.

The energy buncher consists of a dispersive ion-optical stage with a large split dipole magnet system, quadrupole and hexapole magnets. The magnetic quadrupole triplet in front of the dipole magnet is needed to properly illuminate the field volume of the dipole magnet to reach the required resolving power and to focus the secondary beam onto a monoenergetic degrader. The layout of the system and the trajectories are shown in Figure 4.3.4. The quadrupole triplet behind the monoenergetic degrader guides the exotic nuclei into the gas cell or any other detector array. Its main characteristics are: $B\rho_{\mathrm{max}} = 10$ Tm, $\epsilon_x = 300$ mm mrad, $\epsilon_y = 200$ mm mrad, $\Delta p/p = \pm 2.5\%$, (transverse and longitudinal acceptance). Under these conditions a momentum resolving power of $R = 600$ can be achieved.

4.3.4   The Super-FRS quadrupole magnet

Most of the current ion-optic codes use the analytic models for the magnets and then apply an assumed fringe field models to obtain the transfer map. But, with the Laplace solver techniques we have developed it is possible to extract the transfer maps directly from the magnetic field information. We now use the example of the Super-FRS superferric quadrupole to extract the magnetic field and the transfer map. The Super-FRS superferric quadrupole is designed with effective length of 0.8 m with the usable horizontal aperture of ± 0.2 m and the vertical aperture of ± 0.1 m. Using the TOSCA package, the magnetic field data was obtained on a rectangular surface grid enclosing the region of interest. The surface was discretized with a step size of 5 mm, leading to a discretization of $80 \times 40 \times 320$ surface elements. The relative field computation error was $\Delta B/B = 70 \times 10^{-4}$. Figure 4.3.5 shows the TOSCA model for the magnet. We now use this surface date to compute the magnetic field inside the volume and compare the result with the TOSCA simulation for the points inside
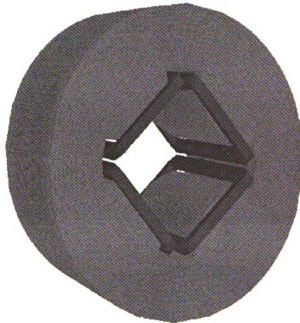
Figure 4.3.5. The TOSCA model for the quadrupole magnet.

the volume.

Figure 4.3.6 shows the difference between the TOSCA and the computed magnetic field for the relative error of the y component of the magnetic field on the midplane of the quadrupole magnet. Due to double midplane symmetry it sufficient to look at the results only for the one quarter of the magnet. It can be seen that the results agree $\sim 10^{-3}$, which is within the TOSCA model computation error of $\Delta B/B = 70 \times 10^{-4}$.

We now study the error dependence on the size (length) of the volume element, or equivalently the number of volume elements chosen for the computation. For the ninth order computation Figure 4.3.7 displays the dependence of the rms average error on the length of the volume element. As an example, for cell lengths of 0.1, with 410 volume data points, the rms error of 8×10^{-5} is observed for the volume element at $(0,0,0)$ with a ninth order computation.

We now extract the transfer map from the Super-FRS quadrupole magnetic field
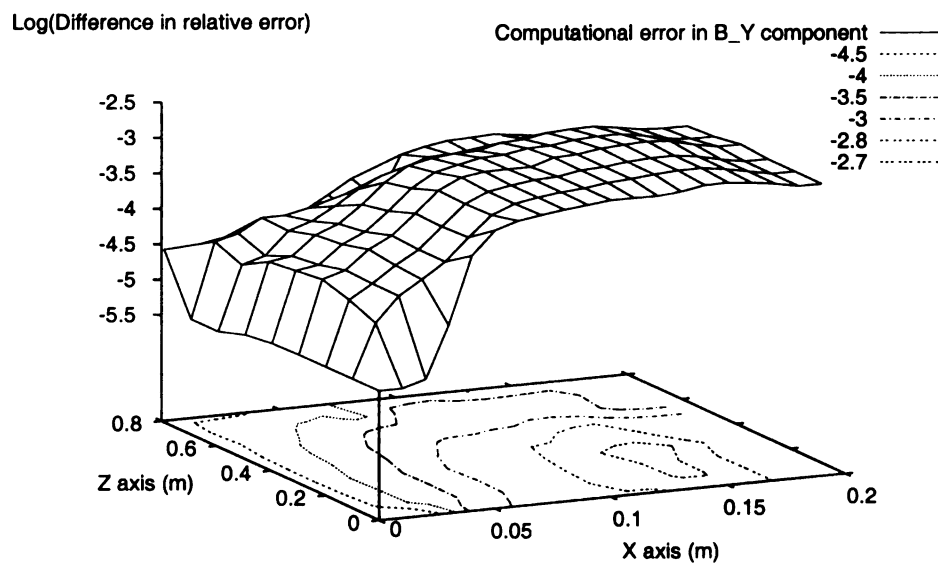
Figure 4.3.6. The difference between the relative error of the y component of the magnetic field on the mid plane. The figure only shows the results for the first quadrant.
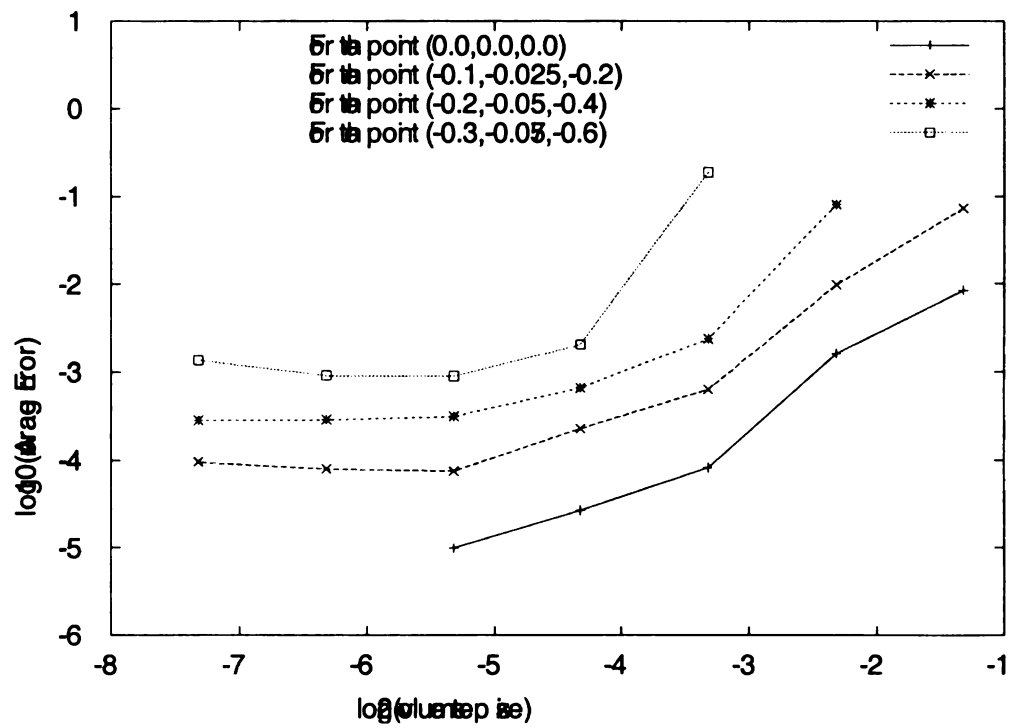
Figure 4.3.7. The rms average difference between the TOSCA simulation result and the new Laplace solver technique versus the volume element length for four volume points (0.0,0.0,0.0), (-0.1,-0.025,-0.2), (-0.2,-0.05,-0.4) and (-0.3,-0.075,-0.6).

data. We solve the ODEs of motion as described in the section 2.3.2. We use the multipole expansion solution of magnetic field computed through the Laplace solver technique to compute the transfer map for the quadrupole. Tables 4.3.5, 4.3.6 and 4.3.7 present the transfer map computed using the magnetic field data on a closed surface.

|					
-0.4705674	-1.394826	0.000000	0.000000	0.000000	100000
0.5581815	-0.4705674	0.000000	0.000000	0.000000	010000
0.000000	0.000000	3.837901	4.272580	0.000000	001000
0.000000	0.000000	3.213394	3.837901	0.000000	000100
0.000000	0.000000	0.000000	0.000000	1.000000	000010
0.000000	0.000000	0.000000	0.000000	0.3989286	000001
0.1284348E-14	0.1535115E-14	0.000000	0.000000	-0.4476261	200000
0.1159401E-14	0.9402369E-15	0.000000	0.000000	0.4865291E-01	110000
-0.1197808E-14	-0.3977569E-14	0.000000	0.000000	-0.1627172	020000
0.1930759E-13	0.5931886E-13	0.000000	0.000000	-2.059670	002000
0.3353931E-13	0.9565057E-13	0.000000	0.000000	-3.933253	001100
0.4768188	-0.4891389	0.000000	0.000000	0.000000	100001
0.1259816	0.4768188	0.000000	0.000000	0.000000	010001
0.000000	0.000000	-1.858375	-0.9955222	0.000000	001001
0.1398535E-13	0.3825810E-13	0.000000	0.000000	-1.984025	000200
0.000000	0.000000	-2.589889	-1.858375	0.000000	000101
0.000000	0.000000	0.000000	0.000000	-0.2995974	000002

Table 4.3.5. The extracted Taylor transfer map for the Super-FRS quadrupole. The Taylor transfer map is shown to second order.

The magnetic field data does not extend to the region far enough for the fringe field to vanish. Hence the transfer map computed may not accurately represent the real transfer map. Further analysis is required to obtain the true transfer map.

4.4 Summary

In this chapter we have successfully demonstrated the utility of the magnetic field computation techniques we have developed. These techniques were applied to analyze a new design of a quadrupole magnet, and to find the multipole decomposition of the magnetic field of the MAGNEX spectrometer dipole magnet, and the quadrupole

124

-5.023497	-1.219005	0.000000	0.000000	0.2575156E-15	300000
-8.056533	-4.472267	0.000000	0.000000	0.2217327E-15	210000
-6.019470	-4.481049	0.000000	0.000000	-0.5442071E-15	120000
-2.428532	-3.420222	0.000000	0.000000	0.000000	030000
0.000000	0.000000	39.46047	50.88769	0.000000	201000
0.000000	0.000000	44.92503	63.97251	0.000000	111000
0.000000	0.000000	24.62299	41.94641	0.000000	021000
26.87556	33.22080	0.000000	0.000000	0.2950176E-13	102000
41.20143	55.84502	0.000000	0.000000	-0.1074050E-13	012000
0.000000	0.000000	-39.97053	-97.22287	0.000000	003000
0.000000	0.000000	21.56656	27.15591	0.000000	200100
0.000000	0.000000	25.13783	36.62275	0.000000	110100
0.000000	0.000000	17.11116	29.54703	0.000000	020100
29.08193	48.08264	0.000000	0.000000	0.4487431E-13	101100
56.42227	81.12632	0.000000	0.000000	-0.2178973E-13	011100
0.000000	0.000000	-68.87387	-200.9709	0.000000	002100
-0.1159274E-15	0.000000	0.000000	0.000000	0.4923260	200001
-0.2781943E-14	-0.4909952E-14	0.000000	0.000000	0.1642214	110001
0.6655356E-15	0.7763230E-15	0.000000	0.000000	0.2524218	020001
-0.2643101E-13	-0.4295697E-13	0.000000	0.000000	3.829388	002001
7.497146	18.20560	0.000000	0.000000	0.1510141E-13	100200
19.69457	29.28498	0.000000	0.000000	-0.1102911E-13	010200
0.000000	0.000000	-37.98898	-141.6864	0.000000	001200
-0.5441379E-13	-0.1018488E-12	0.000000	0.000000	8.142136	001101
-0.2454539	0.3186799	0.000000	0.000000	0.000000	100002
-0.2452654	-0.2454539	0.000000	0.000000	0.000000	010002
0.000000	0.000000	1.639435	0.8273349	0.000000	001002
0.000000	0.000000	-5.482791	-32.98447	0.000000	000300
-0.2705811E-13	-0.5399731E-13	0.000000	0.000000	4.433709	000201
0.000000	0.000000	2.527908	1.639435	0.000000	000102
0.000000	0.000000	0.000000	0.000000	0.2497318	000003

Table 4.3.6. The extracted Taylor transfer map for the Super-FRS quadrupole. The third order coefficients of the Taylor transfer map are shown.

-0.2363760E-14	-0.7663791E-14	0.000000	0.000000	-2.827376	400000
0.1297069E-13	0.6407553E-13	0.000000	0.000000	-4.523454	310000
0.5458716E-13	0.1335168E-12	0.000000	0.000000	-3.289673	220000
0.7936041E-13	0.1489082E-12	0.000000	0.000000	-1.611439	130000
0.5246487E-13	0.1048281E-12	0.000000	0.000000	-0.2505324	040000
0.2214878E-12	0.7629676E-12	0.000000	0.000000	-38.00841	202000
-0.9787271E-12	-0.1752240E-11	0.000000	0.000000	-39.51802	112000
-0.2419524E-11	-0.5075344E-11	0.000000	0.000000	-36.59077	022000

⋮

0.1620236E-11	0.2544577E-11	0.000000	0.000000	14.11275	000400
0.000000	0.000000	11.19360	66.04237	0.000000	000301
0.4103333E-13	0.6831805E-13	0.000000	0.000000	-7.455121	000202
0.000000	0.000000	-2.549064	-1.544657	0.000000	000103
0.000000	0.000000	0.000000	0.000000	-0.2185405	000004
1.572399	13.97146	0.000000	0.000000	0.6739899E-15	500000
18.97848	46.14729	0.000000	0.000000	0.2043959E-13	410000
46.30717	86.55577	0.000000	0.000000	0.6126932E-13	320000
40.04862	79.90497	0.000000	0.000000	0.7543286E-13	230000
18.17722	39.67904	0.000000	0.000000	0.4902103E-13	140000
2.335429	6.248855	0.000000	0.000000	0.5839144E-14	050000
0.000000	0.000000	52.34289	16.25874	0.000000	401000
0.000000	0.000000	-34.47570	-185.8744	0.000000	311000
0.000000	0.000000	-4.958071	-96.76526	0.000000	221000

⋮

-7.871988	7.690329	0.000000	0.000000	0.1030780E-12	100202
53.63167	53.02820	0.000000	0.000000	-0.4518421E-13	010202
0.000000	0.000000	-79.35436	-311.0261	0.000000	001202
-0.9529577E-13	-0.1265356E-12	0.000000	0.000000	18.30773	001103
-0.7612110E-01	0.1853087	0.000000	0.000000	0.000000	100004
-0.2909687	-0.7612110E-01	0.000000	0.000000	0.000000	010004
0.000000	0.000000	1.494996	0.6985110	0.000000	001004
0.000000	0.000000	-201.7121	-64.37471	0.000000	000500
-0.5328690E-11	-0.6519420E-11	0.000000	0.000000	-52.19016	000401
0.000000	0.000000	-15.52484	-102.2664	0.000000	000302
-0.5614135E-13	-0.8194864E-13	0.000000	0.000000	11.06390	000203
0.000000	0.000000	2.597161	1.494996	0.000000	000104
0.000000	0.000000	0.000000	0.000000	0.1966990	000005

Table 4.3.7. The extracted Taylor transfer map for the Super-FRS quadrupole. Some of the fourth and fifth order terms of the Taylor transfer map are shown.

magnet of Super-FRS. We have also extracted the transfer map for the Super-FRS quadrupole from the magnetic field data. In addition, we have also presented the results of the high order ion-optic simulations for the per-separator, the main-separator and the energy buncher of the Super-FRS.

Appendices

APPENDIX A

Comparison of the GICOSY and the COSY INFINITY beam physics codes

Both the GICOSY [19] and the COSY INFINITY [23, 24] codes are widely used computer codes to analyses and simulate the particle optical systems. The GICOSY code is a combination of the GIOS [77] and COSY 5.0 [20] codes. The code GICOSY computes the transfer maps to the fifth order utilizing the magnetic and electric elements from the code COSY 5.0 [20]. We start out by first giving brief description of the both codes. We then compare the maps computed by both the codes for important magnetic and electric elements and summarize our findings.

The **GICOSY** code provides description of the ion optical system using matrices up to fifth order, dipoles with inhomogenieties, quadrupoles and all kinds of multipoles both magnetic and electrostatic, precise treatment of the fringing fields with fringing field integral method or direct tracing of matrix elements using differential algebra use of variables, fitting with different methods, plots of the system, trajectories, envelopes, fields and of phase space distributions, and others. The GICOSY code creates matrix

files of all optical elements that can be used in the Monte-Carlo simulation program MOCADI [1].

The code **COSY INFINITY** is an arbitrary order beam dynamics simulation and analysis code. It allows the study of accelerator lattices, spectrographs, beam lines, electron microscopes, and many other devices. It can determine high-order maps of combinations of particle optical elements of arbitrary field configurations. The elements can either be based on a large library of existing elements with realistic field configurations including fringe fields, or described in detail by measured data. Analysis options include computation of high-order nonlinearities; analysis of properties of repetitive motion via chromaticities, normal form analysis, and symplectic tracking; analysis of single-pass systems resolutions, reconstructive aberration correction, and consideration of detector errors; and analysis of spin dynamics via computation of spin maps, spin normal form and spin tracking.

Differences in approach and implementation:

The code COSY INFINITY code can in principle computes the transfer maps for the particle optical elements to arbitrary order, restricted only by the computational resources available. The coefficients of the transfer maps are computed to machine precision using the differential algebraic techniques. In the GICOSY code the transfer maps for most of the particle optical elements are computed to the maximum of $5th$ order. But, for some of the optical elements the transfer maps are only computed to lower orders. The GICOSY code uses TPSA [7] package to compute the composition of the maps and other operations. However, the coefficients of a transfer map for an individual particle optical element is computed using explicit formulas. The constants appearing in these formulas were entered to only ten digit precision. Hence, the overall accuracy of the maps computed using these coefficients can only be in the order $\sim 10^{-10}$. We expect to see differences of this magnitude in our comparison of the transfer maps generated using the GICOSY and the COSY INFINITY codes.

Parameters	GICOSY and COSY INFINITY
Order of computation	5
Fringe Fields	Off
Output Coordinates	Symplectic coordinates
	with Energy as coordinates
Scaling	Scaled in time
Natural Constants	$amu = 1.6605402 \times 10^{-27}\,\text{kg}$ $e_0 = 1.6021773349 \times 10^{-19}\,\text{C}$ $C_0 = 2.99792458 \times 10^8\,\text{m s}^{-1}$ $amu = 931.4943307\,\text{MeV}$ $\pi = 3.141592653589793$

Table A.0.1. System parameters used for the computation of the transfer maps.

Comparison of maps for important particle optical elements:

To compare the equivalent particle optical elements in the GICOSY and the COSY INFINITY codes, we look at the difference of the maps computed using both the codes. These maps are computed to the $5th$ order, the maximum order supported by the GICOSY code. It would be impractical and also of little use to mention all the coefficients of this difference map and study each coefficient separately. For the purpose of comparison of the maps it would be more useful and practical to consider the RMS average (δ^{5th}_{rms}) of the coefficients of this difference map. This quantity would clearly highlight the differences in the maps, if any. In an ideal case where the equivalent particle optical elements in both codes agree perfectly for all the coefficients of the difference map, the RMS average (δ^{5th}_{rms}) will be of magnitude $\leq 10^{-10}$.

Prior to computing the transfer maps all the system parameters are adjusted to reflect same setting in both the codes. These parameters are listed in Table A.0.1. The GICOSY code was run with computation mode 1, in which the transfer matrixes of the optical elements are calculated by routines generated by the program Hamilton [26]. Where as the COSY INFINITY code was run with default settings.

Table A.0.2 shows the result of the comparison of drift, magnetic and electric particle optical elements. The first column shows the particle optical element. The second column shows the difference between the GICOSY and the COSY INFINITY codes for the 5th order computation of the transfer map. And, the third column

provides comment about the observed difference.

The transfer maps for many of the elements in the GICOSY and COSY INFINITY codes are same. But, for some we notice that the maps agree to only lower orders, suggesting that in the GICOSY code these elements were implemented to lower orders. From Table A.0.2 we see that electric hexapole is implemented to the fourth order in the GICOSY code. And, the electric quadrupole and the magnetic multipole elements are implemented to third order in the GICOSY code. And, the magnetic sector is implemented to only second order in the GICOSY code. Also, it can be seen clearly from Table A.0.2 that the description of the electric sector and electric multipole elements are not same in the GICOSY and the COSY INFINITY codes. Further analysis is needed to find the possible reasons for this difference. Both the GICOSY and the COSY INFINITY codes provide several options for specifying the fringe field for the magnets. But, no options were found that would provide exactly the same description of fringe fields.

Particle Optical Elements	$\delta 5^{th}_{rms}$	Comments
Drift	2.74×10^{-12}	Identical to 5th order
Magnetic Elements		
Dipole	2.21×10^{-10}	Identical to 5th order
Magnetic Sector	3.10×10^{-01}	Identical to 2nd order
Quadrupole	3.08×10^{-11}	Identical to 5th order
Hexapole/Sextupole	2.23×10^{-11}	Identical to 5th order
Octupole	7.43×10^{-12}	Identical to 5th order
DecaPole	9.05×10^{-09}	Identical to 5th order
Duodecapole	2.24×10^{-07}	Some differences
Multipole	1.86×10^{-01}	Identical to 3rd order
Electric Elements		
Electric Sector	3.19×10^{-01}	Not Identical
Quadrupole	1.54×10^{-01}	Identical to 3rd order
Hexapole/Sextupole	6.93×10^{-02}	Identical to 4th order
Octupole	2.75×10^{-12}	Identical to 5th order
DecaPole	7.03×10^{-10}	Identical to 5th order
Duodecapole	5.66×10^{-11}	Identical to 5th order
Multipole	722.79	Not Identical

Table A.0.2. The first column shows the partical optical element. The column 2 shows the RMS average of the coefficients of the difference map between GICO and COSY INFINITY for the 5th order computation. And the third column provides comments about the observed difference.

APPENDIX B

The code converter

The converter program is based on the current release of the GICOSY code [19] (as of Sept. 2005) and the COSY INFINITY version 8.1 [23, 24] code. The converter code is implemented using the Perl programming language. The important beamline elements are translated into the respective elements in the code COSY INFINITY; these include drifts, multipoles, superimposed multipoles, and bends. Table B.0.1 shows the equivalent COSY INFINITY procedure calls for the important GICOSY particle optical elements. Some elements supported by the GICOSY code are translated to drifts or commented out and may have to be adjusted manually. All comments in the GICOSY code are converted to comments in the COSY INFINITY code. The GICOSY code does not require the name and size of the variables to be declared. On the other hand, in the code COSY INFINITY needs all the variables to be declared. In the current converter most of the variable name are extracted from the GICOSY code and are declared in the converted COSY INFINITY code. The loops and fitting routines available in the GICOSY code are commented out in the converted COSY INFINITY code. These have to be manually converted to the equivalent COSY IN-FINITY code.

| GICOSY Command	COSY Command
C O var1 ;	**OV** var1 3 1;
S S ;	**UM** ;
R P var1 var2 var3 ;	**RP** var1 var2×PARA(1) var3;
D L var1 ;	**DL** var1 ;
Magnetic Elements	
M Q var1 ... var3 ;	**MQ** var1 ... var3 ;
M H var1 ... var3 ;	**MH** var1 ... var3 ;
M O var1 ... var3 ;	**MO** var1 ... var3 ;
M D var1 ... var3 ;	**MD** var1 ... var3 ;
M Z var1 ... var3 ;	**MZ** var1 ... var3 ;
M M var1 ... var7 ;	**M5** var1 ... var7 ;
M S var1 ... var8 ;	**MS** var1 ... var8 ;
F F var1 ... var3 ; **M S** var1 ... var3 ;	**DI** var1 ... VAR5 ;
Electric Elements	
E Q var1 ... var3 ;	**EQ** var1 ... var3 ;
E H var1 ... var3 ;	**EH** var1 ... var3 ;
E O var1 ... var3 ;	**EO** var1 ... var3 ;
E D var1 ... var3 ;	**ED** var1 ... var3 ;
E Z var1 ... var3 ;	**EZ** var1 ... var3 ;
E M var1 ... var7 ;	**E5** var1 ... var7 ;
E S var1 ... var8 ;	**ES** var1 ... var8 ;
P M var1 ;	**PM** 6 ;
P A var1 ;	**PM** 6 ;
P N var1 ;	**PA** 6 ;
P S var1.;	**WRITE** 6 var1 ;

Table B.0.1. The table shows the equivalent COSY INFINITY procedure calls for the important GICO particle optical elements.

APPENDIX C

New COSY INFINITY tools for beam physics simulations

For the convenience of presenting and analyzing the spectrometer simulation results the following tools have been implemented in COSY INFINITY:

1. The beam profile generator: This would set the beam profile to either an elliptic or a rectangular shape, which can then be used for phase space plot and the transmission plot. An elliptic or a rectangular distribution of the particles is generated using the pseudo random number generator available in Fortran 77.

2. The phase space plot: This can be used to plot the phase space by choosing x-a or y-b. In addition this can also be used to plot between any two particle optical coordinates.

3. The transmission plot: This tool launches a beam of 1000 randomly chosen particles and looks at transmission through the beam line. The loss comes from the limited aperture of the elements. Final coordinates after each element are computed and compared with the aperture of the element. If the aperture is smaller then the particle coordinates the particle is considered lost. This tool

0.3 E -1

0.9 E -1
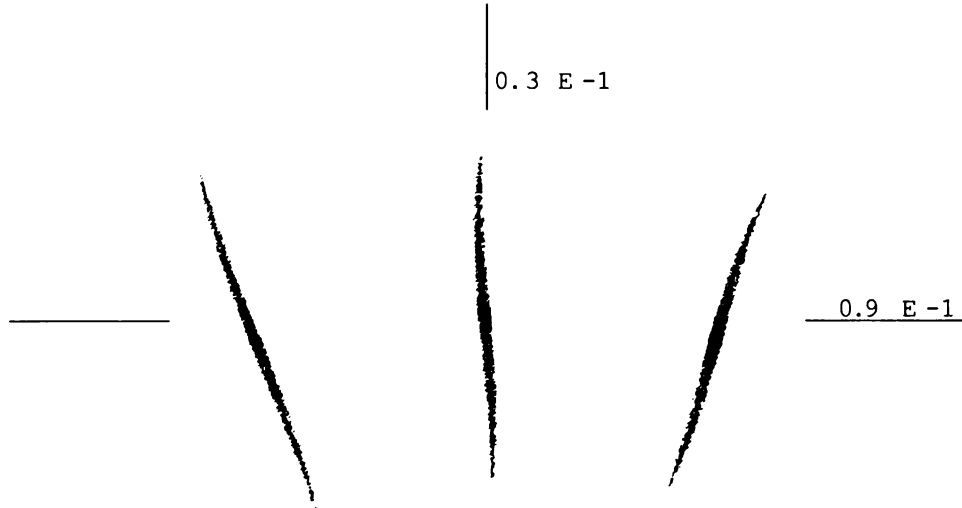
(a) Before correcting aberrations

0.3 E -1

0.9 E -1
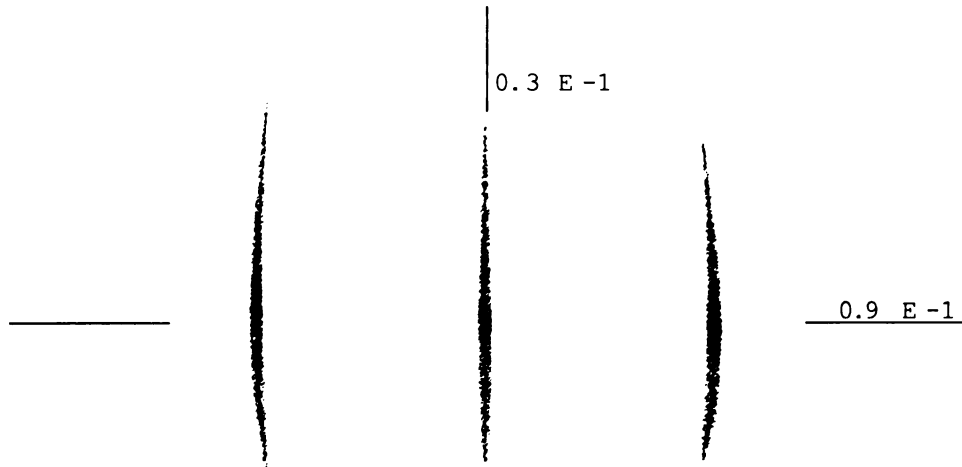
(b) After correcting aberrations

Figure C.0.1. The x-a phase space plots at the dispersive focal plane PF2 for a beam of 40 mm mrad and three different momenta of $\Delta p/p = \pm 2.5$ %. The plot (a) shows the phase space before second order aberration corrections, and (b) shows the phase space after second order aberration corrections.
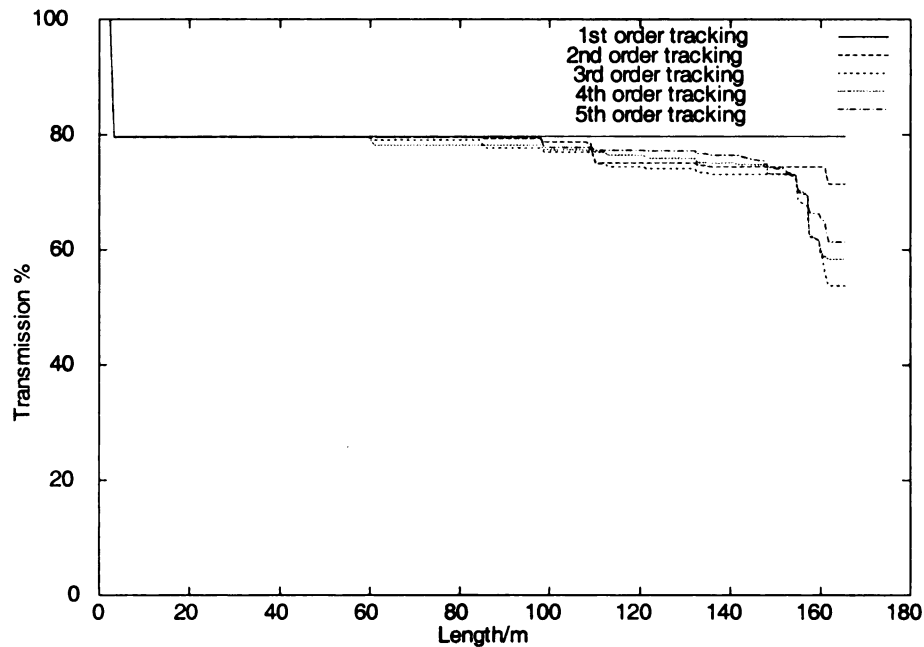
Figure C.0.2. Ion-optic transmisson plot for the Super-FRS high energy branch.

can be modified to include slits and other elements that influence the transmission in a trivial manner. All transmission losses come from purely particle optical effects and is not suitable for modeling reaction products. Example of transmission plot for the Super-FRS high energy branch is shown in the Figure C.0.2.

4. Beam envelope and matrix element plots: This plots the beam envelope and a matrix element versus the length along the optical axis. Figure 4.3.3 shows an example of the beam envelope and the matrix element plot.

5. MOCADI input. This tool generates the COSY INFINITY transfer map output in the GICOSY output format. This can then be used to create input for the Monte Carlo simulation code MOCADI. The input file for MOCADI is generated using the GICOSY and transfers maps from the COSY INFINITY.

BIBLIOGRAPHY

[1] MOCADI 3.0. http://www-linux.gsi.de/ weick/mocadi/. www html page.

[2] Seaborg - IBM SP. http://www.nersc.gov/nusers/resources/SP/. www html page.

[3] The Tosca Reference Manual. Technical Report, Vector Fields Limited, 24 Bankside, Kidlington, Oxford, OX5 1JE, England.

[4] The Tosca User Guide. Technical Report, Vector Fields Limited, 24 Bankside, Kidlington, Oxford, OX5 1JE, England.

[5] The Large Hadron Collider - Conceptual Design. Technical Report AC/95-05 (LHC), CERN (1995).

[6] A. ASI. Boundary element method (bem) for charged particle optics. vol. 4510, pp. 138–147. SPIE (2001).

[7] M. BERZ. The new method of TPSA algebra for the description of beam dynamics to high orders. Technical Report AT-6:ATN-86-16, Los Alamos National Laboratory (1986).

[8] M. BERZ. The method of power series tracking for the mathematical description of beam dynamics. *Nuclear Instruments and Methods* **A258**, 431–437 (1987).

[9] M. BERZ. High-order description of accelerators using differential algebra and first applications to the SSC. In "Proceedings, Snowmass Summer Meeting", Snowmass, Co (1988).

[10] M. BERZ. Differential algebra - a new tool. Technical Report LBL-27033, Lawrence Berkeley Laboratory, Berkeley, CA (1989).

[11] M. BERZ. Differential algebra - a new tool. In "Proceedings of the 1989 IEEE Particle Accelerator Conference", p. 1419. IEEE (1989).

[12] M. BERZ. Differential algebraic description of beam dynamics to very high orders. *Particle Accelerators* **24**, 109 (1989).

[13] M. BERZ. Computational aspects of design and simulation: COSY INFINITY. Technical Report 740, National Superconducting Cyclotron Laboratory, Michigan State University, East Lansing, MI 48824 (1990).

[14] M. BERZ. Computational aspects of optics design and simulation: COSY INFINITY. *Nuclear Instruments and Methods* **A298**, 473 (1990).

[15] M. BERZ. COSY INFINITY, an arbitrary order general purpose optics code. *Computer Codes and the Linear Accelerator Community* **Los Alamos LA-11857-C**, 137 (1990).

[16] M. BERZ. COSY INFINITY. In "Proceedings 1991 Particle Accelerator Conference", San Francisco, CA (1991).

[17] M. BERZ. "Modern Map Methods in Particle Beam Physics". Academic Press, San Diego (1999). Also available at http://bt.pa.msu.edu/pub.

[18] M. BERZ, B. FAWLEY, AND K. HAHN. High order calculation of the multipole content of three dimensional electrostatic geometries. *Nuclear Instruments and Methods* **A307**, 1 (1991).

[19] M. BERZ, B. HARTMANN, K. LINDEMANN, A. MAGEL, AND H. WEICK. GI-COSY Ion Optical Program. http://www-linux.gsi.de/ weick/gico/. www html page.

[20] M. BERZ, H. C. HOFMANN, AND H. WOLLNIK. COSY 5.0, the fifth order code for corpuscular optical systems. *Nuclear Instruments and Methods* **A258**, 402–406 (1987).

[21] M. BERZ, K. JOH, J. A. NOLEN, B. M. SHERRILL, AND A. F. ZELLER. Reconstructive correction of aberrations in nuclear particle spectrographs. *Physical Review C* **47,2**, 537 (1993).

[22] M. BERZ AND K. MAKINO. Verified integration of ODEs and flows using differential algebraic methods on high-order Taylor models. *Reliable Computing* 4(4), 361–369 (1998).

[23] M. BERZ AND K. MAKINO. COSY INFINITY beam physics manual. Technical Report MSUHEP-60804, Department of Physics and Astronomy, Michigan State University, East Lansing, MI 48824 (2006). see also http://cosy.pa.msu.edu.

[24] M. BERZ AND K. MAKINO. COSY INFINITY programmer's manual. Technical Report MSUHEP-60803, Department of Physics and Astronomy, Michigan State University, East Lansing, MI 48824 (2006). see also http://cosy.pa.msu.edu.

[25] M. Berz, K. Makino, K. Shamseddine, G. Hoffstätter, and W. Wan. COSY INFINITY and its applications to nonlinear dynamics. In M. Berz, C. Bischof, G. Corliss, and A. Griewank, editors, "Computational Differentiation: Techniques, Applications, and Tools", pp. 363–365, Philadelphia (1996). SIAM.

[26] M. Berz and H. Wollnik. The program HAMILTON for the analytic solution of the equations of motion in particle optical systems through fifth order. *Nuclear Instruments and Methods* **A258**, 364–373 (1987).

[27] K. L. Brown. A first- and second-order matrix theory for the design of beam transport systems and charged particle spectrometers. Technical Report 75, SLAC (1982).

[28] Y. F. Chang and G. F. Corliss. ATOMFT: Solving ODEs and DAEs using Taylor series. *Computers and Mathematics with Applications* **28**, 209–233 (1994). see also http://www.mscs.mu.edu/ georgec/Pubs/journ.html#1994a.

[29] A. Cunsolo, F. Cappuzzello, A. V. Belozyorov, A. Elanique, A. Foti, A. Lazzaro, O. Malishev, L. Melita, W. Mittig, C. Nociforo, P. Roussel-Chomaz, V. Shchepunov, D. Vinciguerra, A. Yeremin, and J. S. Winfield. Magnex: A large acceptance magnetic spectrometer for EXCYT. *Nuclear and Condensed Matter Physics - Sixth Regional Conference* **513**(1), 270–273 (2000).

[30] A. M. Davis. A generalized helmholtz theorem for time-varying vector fields. *American Journal of Physics* **74**(1), 72–76 (2006).

[31] R. Degenhardt and M. Berz. High accuracy description of the fringe fields of particle spectrographs. In "Proceedings 1993 Particle Accelerator Conference", Washington, DC (1993).

[32] R. Degenhardt and M. Berz. High accuracy description of the fringe field in particle spectrographs. *Nuclear Instruments and Methods* **A427**, 151–156 (1999).

[33] F. M. Denaro. On the application of the helmholtz-hodge decomposition in projection methods for incompressible flows with general boundary conditions. *International Journal for Numerical Methods in Fluids* **43**(1), 43–69 (2003).

[34] B. Erdélyi. "Symplectic Approximation of Hamiltonian Flows and Accurate Simulation of Fringe Field Effects". PhD thesis, Michigan State University, East Lansing, Michigan, USA (2001).

[35] B. ERDÉLYI, M. BERZ, AND K. MAKINO. Detailed analysis of fringe field effects in the large hadron collider. Technical Report MSUCL-1129, National Superconducting Cyclotron Laboratory, Michigan State University, East Lansing, MI 48824 (1999).

[36] L. C. EVANS. "Partial Differential Equations". American Mathematical Society, Rhode Island (1998).

[37] S. FARTOUKH AND O. BRUNING. Field Quality Specification for the LHC Main Dipole Magnets. Technical Report LHC Project Report 501, CERN (2001).

[38] H. GEISSEL, M. WINKLER, H. WEICK, K.-H. BEHR, G. MÜNZENBERG, H. SIMON, K. SÜMMERER, B. ACHENBACH, L. AHLE, T. AUMANN, J. ÄYSTÖ, M. BERZ, A. BLEILE, D. BOUTIN, G. BREITENBERGER, A. BRÜNLE, P. DENDOOVEN, H. EMLING, G. FEHRENBACHER, M. GLEIM, W. HÜLLER, H. IWASE, A. JOKINEN, C. KARAGIANNIS, R. KAISER, A. KELIC, B. KINDLER, G. KLAPPICH, T. KUBO, N. KURZ, K. KUSAKA, H. LEIBROCK, J. LETTRY, B. LOMMEL, S. MANIKONDA, I. MOORE, G. MORITZ, D. MORRISSEY, C. MÜHLE, J. A. NOLEN, I. PSCHORN, T. RADON, R. RONNINGEN, G. SAVARD, C. SCHEIDENBERGER, Y. SHATUNOV, B. SHERRILL, M. SVEDENTSOV, N. TAHIR, K. WENDT, M. YAVOR, A. YOSHIDA, X. YU, A. ZELLER, AND O. ZURKAN. Technical Report on the Design, Construction, Commissioning and Operation of the of FAIR. Technical Report, GSI (2005).

[39] J. GROTE, M. BERZ, AND K. MAKINO. High-order DA methods for the determination of Poincare sections. *Nuclear Instruments and Methods* (in print).

[40] H. HELMHOLTZ. Über Integrale der hydromechanischen Gleichung, welche den Wirbelbewegungen entsprechen. *J. reine angew. Math. (Crelle's Journal)* **55**, 25 (1858).

[41] K. N. HENRICHSEN. Overview of magnet measurement methods. In "CERN Accelerator School 1997" (1997).

[42] J. HOEFKENS. "Verified Methods for Differential Algebraic Equations". PhD thesis, Michigan State University, East Lansing, Michigan, USA (2001).

[43] J. HOEFKENS, M. BERZ, AND K. MAKINO. Efficient high-order methods for ODEs and DAEs. In G. CORLISS, C. FAURE, A. GRIEWANK, L. HASCOËT, AND U. NAUMANN, editors, "Automatic Differentiation of Algorithms from Simulation to Optimization", pp. 343–348. Springer (2002).

[44] J. D. JACKSON. "Classical Electrodynamics". Wiley, New York (1975).

[45] J.IRWIN AND A.DRAGT. "Taylor Maps, Entry in 'Handbook of Accelerator Physics and Engineering', M. Tigner and A. Chao (Eds.)". World Scientific, New York (1999).

[46] Y.-K. KIM AND M. BERZ. Parallel constructs in COSY INFINITY. Technical Report MSUHEP-060805, Michigan State University (2006).

[47] E. R. KOLCHIN. "Differential Algebra and Algebraic Groups". Academic Press, New York (1973).

[48] I. KÜBLER. Master's thesis, Justus Liebig Universität Gießen, 6300 Gießen, West Germany (1987).

[49] A. LAZZARO, A. CUNSOLO, F. CAPPUZZELLO, A. FOTI, C. NOCIFORO, S. ORRIGO, V. SHCHEPUNOV, J. WINFIELD, AND M. ALLIA. Computational aspects of the trajectory reconstruction in the MAGNEX large acceptance spectrometer. In BERZ AND MAKINO, editors, "Computational Accelerator Physics 2002". Institute of Physics Conference Series 175 (2004).

[50] K. MAKINO. "Rigorous Analysis of Nonlinear Motion in Particle Accelerators". PhD thesis, Michigan State University, East Lansing, Michigan, USA (1998). Also MSUCL-1093.

[51] K. MAKINO. The COSY 8th order Runge Kutta integrator. Neutrino Factory/Muon Collider Notes MUC-NOTE-COOL-THEORY-0238, Fermi National Accelerator Laboratory (2002). see http://www-mucool.fnal.gov/notes/notes.html.

[52] K. MAKINO AND M. BERZ. Recent applications of COSY to nonlinear beam dynamics problems. In "Proc. of the APS/DPF/DPB Summer Study on the Future of Particle Physics (Snowmass 2001)", no. T510 (2002). http://www.slac.stanford.edu/econf/C010630/papers/T510.PDF.

[53] K. MAKINO AND M. BERZ. Taylor models and other validated functional inclusion methods. *International Journal of Pure and Applied Mathematics* **6,3**, 239–316 (2003).

[54] K. MAKINO, M. BERZ, D. ERREDE, AND C. J. JOHNSTONE. High order map treatment of superimposed cavities, absorbers, and magnetic multipole and solenoid fields. *Nuclear Instruments and Methods A* **519**, 162–174 (2004).

[55] S. MANIKONDA, J. NOLEN, M. BERZ, K. MAKINO, AND G. WEIZMAN. Design of a superconducting quadrupole with elliptical acceptance and tunable higher order multipoles. Technical Report MSUHEP-060412, Michigan State University (2006).

[56] S. L. MANIKONDA AND M. BERZ. A highly accurate high-order method to solve the Neumann boundary condition problem for the 3D Laplace equation. *International Journal of Pure and Applied Mathematics* **23,3**, 365–378 (2005).

[57] S. L. MANIKONDA AND M. BERZ. Multipole expansion solution of the Laplace equation using surface data. *Nuclear Instruments and Methods* **258**, 175–183 (2006).

[58] S. L. MANIKONDA, M. BERZ, AND K. MAKINO. A highly accurate high-order validated method to solve the Neumann boundary condition problem for the 3D Laplace equation. *Transactions on Computers* **4-11**, 1604–1610 (2005).

[59] P. M. MORSE AND H. FESHBACH. "Methods of Theoretical Physics, Part I and II". (1953).

[60] N. F. OSMAN AND J. L. PRINCE. 3d vector tomography on bounded domains. *Inverse Problems* **14**(1), 185–196 (1998).

[61] H. B. PHILLIPS. "Vector analysis". J. Wiley & Sons, inc.; London, Chapman & Hall, limited, New York (1933).

[62] R. PLONSEY AND R. E. COLLIN. "Principles and Applications of Electromagnetic Fields". McGraw Hill, New York (1961).

[63] P.L.WALSTROM. Soft-edged magnet models for higher-order beam-optics map codes. *Nuclear Instruments and Methods* **A519 1-2**, 216–221 (2004).

[64] P. J. PRINCE AND J. R. DORMAND. High order embedded Runge-Kutta formulae. *Journal of Computational and Applied Mathematics* **7**, 67–75 (March 1981).

[65] S. I. REDIN, N. M. RYSKULOV, G. V. FEDOTOVICH, B. I. KHAZIN, G. M. BUNCE, G. T. DANBY, J. W. JACKSON, W. M. MORSE, R. PRIGL, AND Y. K. S. ET AL. Radial magnetic field measurements with a Hall probe device in the muon (g-2) storage ring magnet at BNL. *Nuclear Instruments and Methods* **A 473, 3**, 260–268 (2001).

[66] N. REVOL, K. MAKINO, AND M. BERZ. Taylor models and floating-point arithmetic: Proof that arithmetic operations are validated in COSY. *Journal of Logic and Algebraic Programming* **64/1**, 135–154 (2004).

[67] J. F. RITT. "Differential Algebra". American Mathematical Society, Washington, D.C. (1950).

[68] G. SABBI. Magnetic field analysis of HGQ coil ends. Technical Report TD-97-040, Fermilab (1997).

[69] M. L. Shashikant, M. Berz, and B. Erdélyi. COSY INFINITY's EXPO symplectic tracking for LHC. *IOP CP* **175**, 299–305 (2002).

[70] V. A. Shchepunov, A. Cunsolo, F. Cappuzzello, A. Foti, A. Lazzaro, A. L. Melita, C. Nociforo, and J. S. Winfield. Numerical computation of arbitrary order transfer maps and reconstructive correction of aberrations in the large acceptance spectrometer MAGNEX. *Nuclear Instruments and Methods B* **204**, 447–453 (May 2003).

[71] I. Vasserman and S. Sasaki. Comparison of different magnetic measurement techniques. In "Proceedings of 13th International Magnetic Measurement Workshop" (2003).

[72] M. Venturini, D. Abell, and A. Dragt. Map computation from magnetic field data and application to the LHC high-gradient quadrupoles. *eConf* **C980914**, 184–188 (1998).

[73] M. Venturini and A. Dragt. Computing transfer maps from magnetic field data. In "IEEE Particle Accelerator Physics Conference" (1999).

[74] M. Venturini and A. J. Dragt. Accurate computation of transfer maps from magnetic field data. *Nuclear Instruments and Methods* **A427**, 387–392 (1999).

[75] P. Walstrom, A. Dragt, and T. Stasevich. Computation of charged-particle transfer maps for general fields and geometries using electromagnetic boundary-value data. In "IEEE Particle Accelerator Conference 2001" (2001).

[76] E. W. Weisstein. Laplace's Equation. From MathWorld–A Wolfram Web Resource. http://mathworld.wolfram.com/LaplacesEquation.html. www html page.

[77] H. Wollnik, J. Brezina, and M. Berz. GIOS-BEAMTRACE, a program for the design of high resolution mass spectrometers. In "Proceedings AMCO-7", p. 679, Darmstadt (1984).

[78] H. Wollnik, J. Brezina, and M. Berz. GIOS-BEAMTRACE, a computer code for the design of ion optical systems including linear or nonlinear space charge. *Nuclear Instruments and Methods* **A258**, 408 (1987).

[79] H. Wollnik, B. Hartmann, and M. Berz. Principles behind GIOS and COSY. *AIP CP* **177**, 74 (1988).

[80] D. A. Woodside. Uniqueness theorems for classical four-vector fields in Euclidean and Minkowski spaces. *Journal of Mathematical Physics* **40**(10), 4911–4943 (1999).

[81] D. A. WOODSIDE. Classical four-vector fields in the relativistic longitudinal gauge. *Journal of Mathematical Physics* **41**(7), 4622–4653 (2000).

[82] K.-H. YANG. The physics of gauge transformations. *American Journal of Physics* **73**(8), 742–751 (2005).